SIMULATION OF METAL PARTICULATES IN HIGH ENERGETIC MATERIALS

THESIS

Eduardo Nieto, Captain, USAF

AFIT-ENY-MS-15-J-043

DEPARTMENT OF THE AIR FORCE
AIR UNIVERSITY

AIR FORCE INSTITUTE OF TECHNOLOGY

Wright-Patterson Air Force Base, Ohio

AFIT-ENY-MS-15-J-043

SIMULATION OF METAL PARTICULATES IN HIGH ENERGETIC MATERIALS

THESIS

Presented to the Faculty
Department of Aeronautical Engineering
Graduate School of Engineering and Management
Air Force Institute of Technology
Air University
Air Education and Training Command
in Partial Fulfillment of the Requirements for the
Degree of Master of Science in Aeronautical Engineering

Eduardo Nieto, B.S.M.E.
Captain, USAF

May 28, 2015

AFIT-ENY-MS-15-J-043

SIMULATION OF METAL PARTICULATES IN HIGH ENERGETIC MATERIALS

THESIS

Eduardo Nieto, B.S.M.E.
Captain, USAF

Committee Membership:

Robert B. Greendyke, PhD (Chairman)

LtCol Richard Huffman (Member)

Maj Darrell S. Crowe (Member)

AFIT-ENY-MS-15-J-043

Abstract

The United States (US) military and its allies have found themselves fighting in asymmetrical wars against terrorist and insurgent groups. Allied forces have been hesitant to attack targets at certain locations due to the probability of injury or death to innocent civilians. Low fragmentation weapons with concentrated pressures that dissipate quickly and the addition of aluminum (Al) particulates in explosive mixtures will provide the capabilities needed to develop weapons needed to fight current and future asymmetric warfare.

The issue with such weapons is that the physics of multi-phase explosives are not well understood. The inclusion of metal particulates in explosives represents a particularly computationally challenging physical environment, in that such flows are "two-phase" flows. In "two-phase" flows, gas physics and solid particle physics are simultaneously simulated. Since the two phases represent different states of matter, matching of physical conditions for the two different phases is difficult to accomplish computationally. The assumptions made for the development of a computational code that simulates multi-phase explosives are presented in this document.

This research focused on analyzing the effects of aluminum in high explosives such as PBX9501 using a computational simulation code. The Multi-Phase Explosive Simulation (MPEXS) hydrocode is used to perform simulations on a wide range of metalized explosive cases, where the varying parameters are the size of the aluminum particles from 9 to 34 microns and the mass fraction of aluminum from 10 to 20 percent. The mass fraction directly correlates to the amount of aluminum present in the mixture. The MPEXS code was evaluated by performing several studies including a data convergence test to determine the stability and limitations of the code.

The important explosive detonation parameters that were considered to evaluate the effects of aluminum were pressure, density, detonation velocity, and Run-to-Detonation (Run2Det) time and distance. The results showed that the gas pressure steadily increased as the Al particle diameter increased. When the Al mass fraction was increased, the gas pressure for each of the particles decreased. The gas density displayed the same trends as pressure. Density steadily increased as the Al particle size increased, and density decreased when Al mass fraction increased. Detonation velocity steadily decreased as the Al particle diameter was increased, and detonation velocity decreased as the Al mass fraction increased. It was concluded that varying the aluminum mass fraction had a larger effect on Run2Det properties than varying the aluminum particle diameter for both Run2Det distance and time. In general, increasing the Al mass fraction will decrease the the time and distance for the detonation to reach steady-state.

The addition of metal particulates in explosive mixtures increases the density of the shock wave, causing a higher pressure in the shock. The high pressure in the shock is devastating and will incapacitate adversaries in physical proximity of the detonation of the munition. The concentrated pressures will dissipate quickly due to the high density, providing a short proximity detonation. This research significantly contributes to both current explosive simulation analysis and development of future explosive formulations for better munitions that will save many lives.

I dedicate this to my wife who has encouraged and supported me through this difficult journey. Also, to my daughter who is my daily motivation.

Acknowledgements

Dr. Robert Greendyke, thank you for being a great advisor and aiming me in the right direction through this entire process. Thank you for going the extra mile to make sure I had all the resources I needed.

Dr. Michael Crochet, Dr. Sunhee Yoo, Dr. Steven Pemberton, and all the folks at the HERD, thank you for your time and support with the simulation code. I hope my research will assist you in the development of future versions of the simulation code.

LtCol Richard Huffman and Maj Darrell Crowe, thank you taking time out of your busy schedules to be members of my thesis committee and thank your for your feedback.

Eduardo Nieto

Table of Contents

List of Figures

Figure Page

List of Tables

List of Acronyms

AFIT Air Force Institute of Technology

AFRL Air Force Research Laboratory

BN Baer and Nunziato

CJ Chapman-Jouguet

DOD Department of Defense

DOE Design of Experiments

EOS Equation of State

HERD High Explosives Research and Development

JWL Jones-Wilkins-Lee

LX Livermore's High-Energy Explosive

MC Monte Carlo

MD Molecular Dynamics

MPEXS Multi-Phase Explosive Simulation

ORVIS Optically Recording Velocity Interferometry System

PBX Polymer-Bonded Explosive

PTFE Polytetrafluoroethylene

PVDF Polyvinylidene Fluoride

RDX Research Department Explosive

Run2Det Run-to-Detonation

SNL Sandia National Laboratories

SPEXS Single-Phase Explosive Simulation

TNT Trinitrotoluene

US United States

ZND Zeldovich, Von Neumann, and Deering

1-D One-Dimension

3-D Three-Dimension

List of Symbols

α_{sg} drag partitioning function

Al aluminum

AlF_j aluminum fluorides

β_{sg} inter-granular stress

$\mathcal{C}$ mass source term

$\mathcal{C}_i$ i-th solid mass source term

c_{sg} compaction partitioning function

D Detonation velocity

D_{CJ} CJ detonation velocity

d_m grain mean diameter

δ_{sg} drag coefficient

$\mathcal{E}$ energy source term

$\mathcal{E}_i$ i-th solid energy source term

E_i i-th solid total specific energy

E_g gas total specific energy

E_s solid total specific energy

e_g gas specific internal energy

e_s solid specific internal energy

$\mathcal{F}$ compaction source term

Fe_2O_3 hematite

$\mathbf{g}_i$ nozzling sources

GiB gibibyte

γ heat capacity ratio

H_{sg} heat transfer coefficient

K_{pr} oxidation rate

λ mass fraction

λ_m metal mass fraction

λ_m^o initial metal mass fraction

$\mathcal{M}$ momentum source term

$\mathcal{M}_i$ i-th solid moment source term

μ_{sg} compaction viscosity

Nx computational cells

P pressure

P_{CJ} CJ pressure

P_i i-th solid pressure

P_g gas pressure

P_s solid pressure

$P-u$ pressure vs particle velocity

$P-U$ pressure vs shock velocity

$P-v$ pressure vs specific volume

ϕ volume fraction

ϕ_i i-th solid volume fraction

ϕ_g gas volume fraction

ϕ_s solid volume fraction

q specific heat

ρ density

ρ_{CJ} CJ density

ρ_i i-th solid density

ρ_g gas density

ρ_o initial density

ρ_s solid density

t time

T temperature

T_g gas temperature

T_s solid temperature

u particle velocity

u_{CJ} CJ particle velocity

u_i i-th solid particle velocity

u_g gas particle velocity

u_p piston velocity

u_s solid particle velocity

$u - v$ particle velocity vs specific volume

$U - u$ shock velocity vs particle velocity

$U - v$ shock velocity vs specific volume

x position

ξ_{sg} chemical reaction partitioning function

SIMULATION OF METAL PARTICULATES IN HIGH ENERGETIC MATERIALS

I. Introduction

Asymmetrical warfare has presented many issues to the US and its allies in the way wars are being fought. Allied forces have been hesitant to attack targets at certain locations due to the probability of injury or death to innocent civilians. One solution to this problem is the development of more advanced weapons. Low fragmentation weapons with concentrated pressures that dissipate quickly might provide a solution that eliminates targets with less or no collateral damage. The addition of Al particulates in explosive mixtures might provide the capabilities to develop weapons needed to fight current and future asymmetric warfare. Explosive simulation hydrocodes such as the MPEXS code will allow researchers to study multi-phase explosives and formulate new explosive material for use in future advanced munitions. Section 1.1 provides a background on the current issues of asymmetrical wars the US is facing. Section 1.2 introduces the topic of metalized explosives, and discusses the assumptions and limitations of computational modeling of explosives. Section 1.3 presents the research questions that were explored in this research. Finally, Section 1.4 gives an overview of subsequent chapters in this document.

1.1 Background

1.1.1 Asymmetrical Warfare

In the recent Iraq and Afghanistan wars, the US military and its allies have found themselves fighting in asymmetrical wars against terrorist and insurgent groups. These groups have resorted to strategies and tactics that involve hiding in and attacking from heavily populated zones, hospitals, schools, mosques, and other locations. This type of asymmetrical warfare makes allied forces hesitant to attack such locations using conventional weapons due to the risk of damage to non-combatant targets or threat to innocent civilians. Conventional weapons such as air-to-surface missiles and bombs are designed to destroy targets effectively by destroying entire buildings and town-blocks where adversaries are located. The problem with asymmetrical warfare is that the US military can no longer destroy targets using conventional weapons. The US needs the capability to eliminate targets with diminished risk of killing innocent civilians.

War strategy is dependent on many factors and it is always changing to meet the needs of war. One thing that has not changed much is that wars have been fought in a conventional way for a long time. Conventional warfare can be defined as a confrontation between two or more groups with well-defined confrontation lines. These lines or boundaries can be a location on a field of battle, or the border line of a country, or a boundary surrounding the location where the opposing side is located. Either both sides come to accordance on where the battle will be fought or one side attacks the other side's territory. In both cases there is a clear distinction between the groups/enemies. The purpose of conventional warfare is to weaken or destroy the enemy's military. When destroying or weakening the enemy is not possible, either side might resort to asymmetrical warfare to exploit the other's weakness.

The US and its allies have shown superiority over enemies and terrorist groups when it comes to conventional warfare. Operation Desert Fox was an example of an effective attack campaign that destroyed the enemy's military infrastructure in a short period of time with no allied losses [10]. Operation Desert Fox was the “code-name” for the bombing of Iraq on December 16 - December 20, 1998 [10]. The invasion of Iraq in 2003 was another example of a successful campaign in a conventional type of war. From 20 March 2003 - 1 May 2003 the coalition forces invaded Iraq and overthrew the Ba'athist Iraqi government led by Saddam Hussein. The campaign ended when Coalition forces captured the city of Baghdad. To put in perspective the superiority of the US in conventional warfare, coalition forces attacked an enemy of equal troop size and defeated the Ba'athist Iraqi government while only suffering a few hundred losses.

Terrorist groups and Taliban insurgents learned that their chances of defeating the US in conventional warfare are close to none and therefore they have resorted to fighting with asymmetrical tactics. These adversary groups have found that the US will not attack hospitals, schools, mosques and populated zones; therefore these groups use such locations as hiding shelters and weapon storage. Asymmetrical warfare presents many problems for allied forces fighting against insurgent and terrorist groups. The US needs to adapt to this type of warfare by developing methods and weapons to effectively eliminate enemy targets without injuring or killing innocent bystanders.

1.1.2 Munitions

Precision-guided munitions have allowed the US military to strike specific targets with great accuracy. These bombs and missiles are dropped from high altitudes and are guided within a few feet of the target. Although such munitions reduce collateral damage by reducing the miss distance from the actual target, metal fragments from the munition case travel large distances and kill innocent civilians near the detonation location.

Most conventional munitions are composed of a metal case that encloses the explosive material and other components. The purpose for the metal shell is to allow the munitions to penetrate tanks, buildings, bunkers, and other material without disintegrating before detonation. When the munition detonates, the internal pressure creates tensile stress on the case as it expands causing it to crack and creating many metal fragments. "The sizes of fragments are a function of the rate of cylinder expansion" due to the explosion, which can be calculated by Mott's equations [4]. Chapter 27 of Cooper's textbook [4] provides equations that calculate the velocity and position of the fragments. It can be calculated that fragments can travel at speeds close to Mach 3 and travel hundreds of feet depending on the size of the fragment.

The need for munitions with no to little fragmentation is growing due to current and forthcoming wars. For that reason, the Air Force Research Laboratory (AFRL) Munitions Directorate is exploring and testing munitions that do not produce metal fragmentation during detonation. Reducing fragmentation in munitions can be accomplished by using a composite case made from materials like wound-carbon-fiber. During the explosion the high temperatures and pressures disintegrate the carbon-fiber casing, thus not producing any fragments. These carbon-fiber casing warheads are a solution to reducing fragmentation. The next step in fielding such munitions is to develop the best explosive formulation that would maximize the performance of new carbon-fiber casing munitions.

1.2 Research Problem Description

1.2.1 Introduction

Dr. Crochet et al have performed numerical analysis on multi-phase explosives simulations composed of metal particulates and explosive compounds [7]. These numerical analyses have provided utile information about multi-phase explosives. The addition of metal particulates in explosive mixtures increases density to the shock wave, causing a higher pressure in the shock. These high-pressure shocks are devastating and will incapacitate adversaries in physical proximity to the detonation of the munitions. The combination of low fragmentary munition casings and the increase in shock wave pressure, through metalized explosives, has the potential to effectively eliminate threats in modern asymmetrical combat theaters.

1.2.2 Background and Issues of Metalized Explosives

The issue with such a weapon is that the physics of multi-phase explosives are not well understood. The inclusion of metal particulates in explosives represents a particularly computationally challenging physical environment, in that such flows are "two-phase" flows. In "two-phase" flows, gas physics and solid particle physics must be simultaneously simulated. Since the two phases represent different states of matter, matching of physical conditions for the two different phases is difficult to achieve computationally.

In a simple explosive mixture there are two components, the solid explosive grains and the reaction gas products [5]. Piston-impact simulations are commonly used to determine properties of the explosive being tested. Detonation velocity (D), pressure (P), density (ρ), temperature (T), and material sensitivity are a few of the properties resulting from piston-impact simulations. Other important properties that provide an overview of the explosive mixture is Run2Det distance and time. The description “Run-to-detonation” is abbreviated to “Run2Det” in this report. Run2Det time is the point when the chemical reaction of the detonation reaches steady-state and its detonation properties remain constant. Run2Det distance is the distance from the piston at which the shock wave reaches steady-state. As the impact-induced detonation is initiated, a shock front compresses and heats the explosive, which initiates an instant exothermic chemical reaction. The energy released from the exothermic reaction continues to feed the shock and drives the shock forward [4]. Conventional explosives composed of a simple mixture are computationally simpler because the explosive transitions from a solid to a gas phase. Simple mixture explosives require fewer equations that model the conservation of mass, energy, and momentum relationships.

Simulations become more complex and expensive with explosives that contain multiple solid components. Multi-component explosives are a three-phase system; one phase consists of a mixture of condensed explosive and metal grains, another phase consists of the reaction zone, and the product phase consists of solid metal oxide and vaporized metal [5]. Baer and Nunziato (BN) formulated a system of equations that allow basic simulations of “two-phase” flows, more details of which can be found in in Chapter III of this thesis [3] . This system of equations considers separate mass, momentum, and energy balance equations for each component and additional expressions related to the evolution of the solid volume fractions [5].

1.2.3 Research Assumptions and Limitations

The complexity of computationally modeling explosive reactions pushes researchers to make many assumptions in order to obtain approximations of the reaction. Without assumptions these simulations would be almost impossible to model correctly. Most of the modeling methods use Euler’s conservation equations, which assume that the flow is inviscid and adiabatic. Chapter III explains the assumptions that were made in order to obtain appropriate equations of state for the explosive. Some of those assumptions are that the model will conserve mass, momentum, and energy, and that the flow is inviscid and adiabatic.

Although a Three-Dimension (3-D) simulation would provide results closer to experimental explosions, it would be more computationally and analytically intensive. Most explosive modeling is limited to One-Dimension (1-D) because it is less computationally expensive and will provide a simple wave solution that is sufficient to determine detonation properties.

Certain conditions in multi-phase explosives such as the transition from solid state to gas state of metal particulates can complicate computational simulations. Modeling methods for heterogeneous explosives can become very complicated. The choice of technique is dependent upon the required accuracy and computational resources available. Chapter III includes a detailed description of the multi-phase modeling method chosen for this research.

1.3 Research Questions

The main focus of this research is the study of the effects of aluminum in high explosives such as PBX9501 using the hydrocode developed by AFRL. A hydrocode is a computational program for modeling the behavior of fluid flow like explosive flows. This research utilizes the MPEXS hydrocode which was developed by Dr. Crochet, a computational researcher at the Munitions Directorate of AFRL. Dr. Crochet's numerical scheme demonstrated that detonation velocity has a strong dependence on various parameters such as the metal grain size and metal mass fraction that is mixed with high explosive HMX ($C_4H_8N_8O_8$) [5]. Al grain size and initial metal mass fraction (λ_m) will be the independent variables of interest to study the detonation effects. The MPEXS code will be used to evaluate the effects of aluminum particulates in the high explosive PBX9501 and provide a recommendation on an explosive mixture.

Determining the effects of *Al* grain size and mass fraction on detonation properties for PBX9501 are the main focus, but the MPEXS hydrocode will also be evaluated. The MPEXS code will be evaluated by performing several studies to determine the stability and limitations of the code. The MPEXS code needs to output comparable data to other hydrocodes. The stability of the MPEXS code will be determined by looking for a convergence in the data as the grid resolution is increased. Performing a wide range of simulations will insure that minimums and maximums will be tested, providing an idea of the limitations of the code.

1.4 Overview of Subsequent Sections

Chapter I includes a background on current asymmetrical warfare and the problems presented to the US and its allies. One of the problems faced is the high probability of injury or death to innocent civilians resulting from conventional munitions. A solution to such problem is the development of low fragmentary munition casings and explosive formulations that yield strong blast effects within a small radius and then rapidly drop off in strength. Chapter I also includes the research problems and the research questions to be answered. Chapter II will present a literature review on the fundamentals of detonation theory, previous research on the effects of aluminum on detonation velocity, and multi-phase explosive modeling techniques. Chapter III will present a detailed methodology of the simulations and data collection procedures that was implemented to obtain the sought after results. Chapter IV will present the results of the simulations that were performed. Finally, Chapter V will summarize the data, and make conclusions about the effects of aluminum on PBX9501 and the performance of the MPEXS code.

II. Literature Review

2.1 Introduction

To understand the effects metal particulates have in explosive materials, one must begin with the basics. This chapter will include a literature review of the fundamentals of detonation to understand the physics, thermodynamics, and chemical reactions that occur in an explosive detonation. A shock wave traveling radially out from the center of the explosion provides very useful information of the detonation. Detonation velocity, pressure, and temperature are a few of the parameters that are studied. Throughout the years much of empirical data has been collected on explosives and equations have been developed based on this data. In recent years new heterogeneous explosives have emerged. These explosives might be a mixture of several explosive materials or a mixture of explosive materials and metalized powders. This literature review also includes current simulation work on heterogeneous explosive materials, as well as explosive materials with aluminum particulates which is the area of interest for this thesis.

2.2 Fundamentals of Detonation Theory

2.2.1 Simple Theory

An explosive detonation is a very complicated fluids problem because it is a shock wave traveling out radially with a rapid exothermic chemical reaction zone occurring behind the shock front [4]. By considering a simple model of detonation, it puts this complicated fluids problem into simpler terms. The "simple theory" or "Zeldovich, Von Neumann, and Deering (ZND) theory" mathematically simplifies detonation by quantifying thermodynamic and kinetic terms into first-order engineering problems [4]. The ZND theory makes the following six assumptions [4]:

First: The flow is 1-D (laminar).

Second: The detonation front is a discontinuity because there is an instantaneous jump in the pressure.

Third: All the reaction gases are in chemical and thermodynamic equilibrium.

Fourth: The chemical reaction zone is infinitely thin.

Fifth: The detonation velocity is constant and therefore the products leave at the same state and are independent of time.

Sixth: The detonation products can change after leaving the reaction zone.

Based on these assumptions, a detonation is defined as a shock wave passing through the explosive (explosive or energetic is interchangeably through out this thesis) with a following rarefaction wave or gas expansion. This wave is known as a Taylor Wave, named after the British mathematician Geoffrey Ingram Taylor who developed the Equation of State (EOS)s for the wave. The Taylor wave can be seen in Figure 1. "The shock front, chemical reaction, and the leading edge of the rarefaction are all in equilibrium; so they are all moving at the same speed, which we call detonation velocity (D) [4]." The steady-state detonation condition for the products is known as the Chapman-Jouguet (CJ) point, shown by the blue dot in Figure 1. The Von Neuman Spike is the necessary energy to activate the chemical reaction, see Figure 1. The distance between the vertical dashed line and vertical solid line in Figure 1 represents the reaction zone of the detonation wave. For ZND theory, the reaction zone is assumed to be infinitely thin or zero as stated by the forth assumption listed above. Another important detonation parameter is the CJ pressure (P_{CJ}).

2.2.2 Wave Properties

In explosives, piston-impact simulations are commonly utilized to determine properties of the explosive materials being tested. A piston-impact problem is simulated by a rigid piston moving with constant u_p inside a rigid tube which contains explosive materials and gases. The denotation is initiated when the piston compresses the explosive materials and gases. A forward-moving shock wave travels with velocity D. To understand this piston-impact problem, the flow field between the piston and the shock must be solved. D is an important parameter that could be solved by using the Hugoniot relationships. A suitable flow connecting the piston and the final state must be found [9]. The solution can consist of a rarefaction wave. When the piston velocity is less than detonation velocity, the front of the wave still exists and a rarefaction wave is needed "to reduce the velocity at the front to that at the piston [9]." Figure 1 shows the detonation wave front and the rarefaction wave that follows. Figure 1 is based on a figure by Fickett and Davis [9].

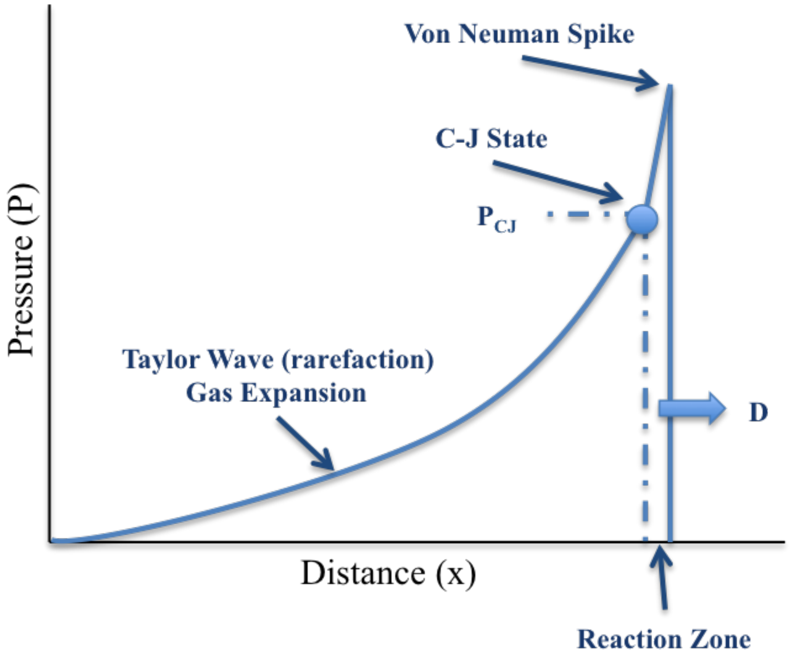

Figure 1. Detonation Wave

The *final state* as described by Fickett and Davis, is where the flow stabilizes just after the reaction zone of the detonation wave [9]. “The conservation conditions require that the *final state* point in the pressure vs specific value plane lie on both this Hugoniot curve and the Rayleigh line [9].” The *final state* is given by the intersection of the Rayleigh line and the Hugoniot curve as shown in Figure 2. Figure 2 is based on a figure by Fickett and Davis [9]. There are three different final state solutions. 1) If D is less than the CJ detonation velocity (D_{CJ}), the red Rayleigh line does not cross the blue Hugoniot curve, therefore there is no steady-state solution [9]. 2) If D is equal to D_{CJ}, the red Rayleigh line crosses the blue Hugoniot curve at one location, the CJ point, therefore there is one steady-state solution [9]. 3) If D is greater than the D_{CJ}, the red Rayleigh line crosses the blue Hugoniot curve at two locations, therefore there are two possible solutions [9]. The upper or strong intersection where the flow is subsonic is utilized for steady state analysis [9]. The lower or weak intersection is rejected because the flow is supersonic [9].

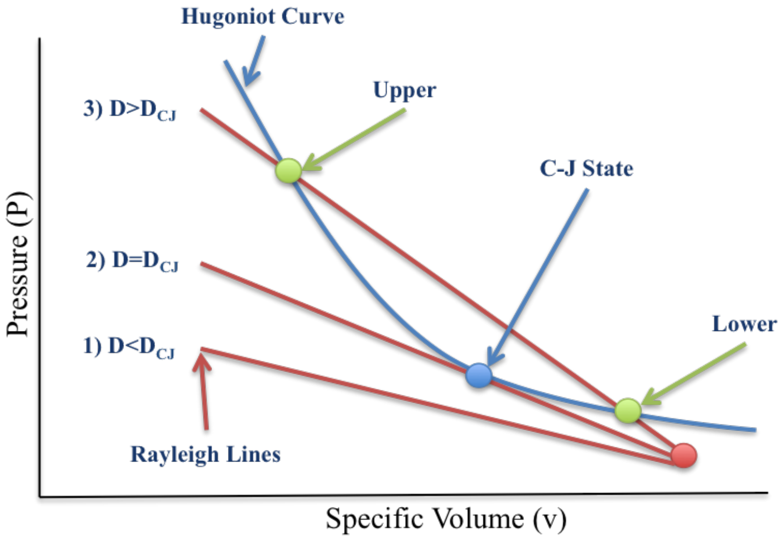

Figure 2. Hugoniot Curve and Rayleigh Lines Relationships: Final State Conditions

2.2.3 Solving for Explosive Parameters

There are a few important parameters that need to be determined for explosive analysis and those are CJ density (ρ_{CJ}), CJ particle velocity (u_{CJ}), P_{CJ}, and D. Empirical data shows that there is a relationship between initial density (ρ_o) and the ρ_{CJ}. When plotting the empirical data on a log scale it is seen that there is a fairly linear relationship. Therefore, Cooper derived Equation 1 to solve for ρ_{CJ} [4].

$$\rho_{CJ} = 1.386\rho_o^{0.96} \quad [4] \tag{1}$$

where ρ_{CJ} is CJ density, and ρ_o is initial density.

The P_{CJ} and u_{CJ} can be determined from initial density and D empirical values using mass and momentum conservation equations. Equation 2 provides an estimate of P_{CJ} within 5% of experimentally measured values [4]. Equation 3 demonstrates how u_{CJ} can be calculated when P_{CJ} and ρ_o are known [4].

$$P_{CJ} = \rho_o D^2(1 - 0.7125\rho_o^{0.04}) \quad [4] \tag{2}$$

$$u_{CJ} = \frac{P_{CJ}}{\rho_o D} \quad [4] \tag{3}$$

where P_{CJ} is CJ pressure, ρ_o is initial density, D is detonation velocity, and u_{CJ} is CJ particle velocity.

The Equations 2 and 3 provide acceptable approximations for certain explosive parameters at the CJ state. It is also important to determine explosive parameters at other conditions along the Hugoniot curves. Hugoniots are empirically derived EOS relating six different variable pairs such as pressure vs shock velocity ($P - U$), pressure vs particle velocity ($P - u$), pressure vs specific volume ($P - v$), shock velocity vs particle velocity ($U - u$), shock velocity vs specific volume ($U - v$), and particle velocity vs specific volume ($u - v$) [4]. Estimating Hugoniot relationships can be approximated more accurately using computer codes that use empirically derived nonlinear EOS. Due to the complexity of the nonlinear EOS these codes can be computationally expensive requiring large computers or codes are not readily available to most engineers. However, there are simple empirical correlations that will provide solutions with reasonable accuracy based on P/P_{CJ} ratios. The data correlates to two regions; for reduced pressure ratios above 0.08 use Equation 4 and for reduced pressure ratios below 0.08 use Equation 5 [4].

$\frac{P}{P_{CJ}} > 0.08$:

$$\frac{P}{P_{CJ}} = 2.142 - 1.7315\left(\frac{u}{u_{CJ}}\right) + 0.3195\left(\frac{u}{u_{CJ}}\right)^2 \qquad [4] \tag{4}$$

$\frac{P}{P_{CJ}} < 0.08$:

$$\frac{P}{P_{CJ}} = 235\left(\frac{u}{u_{CJ}}\right)^{-8.71} \qquad [4] \tag{5}$$

where P is pressure, P_{CJ} is CJ pressure, u_{CJ} is CJ particle velocity, and particle velocity (u).

There are several methods to develop equations of state for an explosive material. Equations of state for explosive products are only engineering approximations for simulating explosive behaviors [9]. As discussed above, one of the methods is to find a Hugoniot relationship between the six different variable pairs. These relationships can be done with nonlinear EOS using computers or using simple empirical correlations. These simple theory EOSs have many limitations that are based from the assumptions made in the Simple Theory section. So far we have focused on the EOS for the explosive material, but now we need to look for EOS for the reaction products. Fickett and Davis discussed several forms that have been utilized to determine reaction product EOS [9]. Some of these forms account for the chemistry in the reaction and some that do not. There are four EOS without chemistry discussed by Fickett and Davis; 1) the constant-γ form, 2) the constant-β equation of state, 3) the constant-α equation of state, and 4) the Jones-Wilkins-Lee (JWL) equation of state [9]. One of the simplest form is the constant-γ form which yields Equation 6 for P_{CJ} and Equation 7 for D_{CJ}.

$$P_{CJ} = 2(\gamma - 1)\rho_o q \quad [9] \tag{6}$$

$${D_{CJ}}^2 = 2(\gamma^2 - 1)q \quad [9] \tag{7}$$

where P_{CJ} is CJ pressure, D_{CJ} is detonation velocity, heat capacity ratio $(\gamma) = 3$, ρ_o is initial density, and specific heat (q).

Another form is the constant-β equation of state were β is constant for all pressures and specific volumes. The equations for P_{CJ} and D_{CJ} are complicated, therefore Fickett and Davis derived Equations 8 and 9 that approximate P_{CJ} and D_{CJ} based on empirical correlations for the explosive Composition B [9].

$$P_{CJ} \propto {\rho_o}^{13/6} q^{1/3} \quad [9] \tag{8}$$

$${D_{CJ}}^2 \propto {\rho_o}^{2/3} q^{1/3} \quad [9] \tag{9}$$

where P_{CJ} is CJ pressure, D_{CJ} is detonation velocity, ρ_o is initial density, and q is specific heat.

Another form is the constant-α equation of state. These EOS are similar to the constant-β equation of state, but α is a function of pressure, where as β is a function of specific volume. Just like the constant-β equation of state, the P_{CJ} and D_{CJ} equations are complicated and require a computer code to solve. Another form of the constant-β EOS is the JWL equation of state, but it uses the Gruneisen coefficient instead of β. The four different forms can be utilized, but according to Fickett and Wood the constant-β equation of state has the most reasonable properties in the region of interest [9].

Once a form of the EOS has been chosen, important parameters like P and D can be determined. The calculated P and D values, which were derived from the EOS must be compared to empirical data. This comparison will determine if the coefficients utilized for the P and D equations provided a good correlation to the empirical data. If the coefficients did not provide a good correlation then they must be reconsidered. The EOS should be calibrated using the empirical data until a stronger correlation is derived.

2.3 Heterogeneous Explosive Materials

As previously stated, determining explosive parameters of pure explosive can be accomplished with certain confidence, but it can get computationally intensive depending on the accuracy needed and the modeling methods utilized. This problem is exacerbated when the explosive materials are heterogeneous. Heterogeneous implies the explosive mixture is composed of different materials, phases, or grains of different densities. It is important that heterogeneous explosive materials are studied because almost all explosives utilized in the military or commercially are heterogeneous. Some explosives use binding materials to hold the explosive crystals together as well as to decreases the shock sensitivity of the explosive by preventing the explosive grains from touching each other, making it safer to handle. Polymer-Bonded Explosive (PBX) and Livermore's High-Energy Explosive (LX) are examples of explosives that use "plastic" as a binder material. Other heterogeneous explosives mix two or more explosive materials, for example Composition B consists of a mixture of Research Department Explosive (RDX) and Trinitrotoluene (TNT).

The microstructure of these heterogeneous materials introduce internal boundary effects that change the thermal/mechanical/chemical behavior of the explosive [2]. The microscale, at the atomic level, is usually not utilized for these types of experiments because it requires greater computational resources. To get an idea between the micro and meso scales, Dr. Baer gives an example that a $1\mu m$ long solid material flake would contain 10^{17} atoms [2]. Therefore, the mesoscale is more appropriate for these explosive experiments.

Some of Dr. Baer's prior work has demonstrated that particle diameter and morphology are very important parameters to the formulation of explosive materials [2]. Many performance parameters like shock sensitivity, pressure, detonation velocity, and particle velocity are believed to be directly affected by particle size and morphology of the explosive. In order to trigger a chemical reaction a certain pressure threshold must be met. Tests indicated that fine grain HMX, with average particle diameter of 10-15μm, required higher pressures to trigger the reaction than other larger grain HMX [2]. Most of the current work is either done through computer simulation or by impact loading experiments, but better "experimental techniques for measurement at the mesoscale crystal level are currently in development [2]."

2.3.1 Uniform Mixing Methods

Heterogeneous materials when mixed properly should have uniform mixture of all the particles. The explosive mixture should be uniform enough that samples of the same mixture should not vary from sample to sample. As with real explosives, computer simulations of explosives should have uniform mixture. The heterogeneous material must be modeled by using a computerized method that randomly distributes the varied geometry crystals into a closely packed configuration, so that the mixture is as uniform as possible [2]. Due to the infinite number of possible combinations, the size and geometry of the explosive crystals must be limited to a certain range of sizes and geometries. Since the main concern is particle/crystal size, the geometry can be limited to one shape, even though in real explosive materials a myriad of crystal shapes exist.

Dr. Baer mentions two computer simulation methods to randomly distribute and pack particles of a heterogeneous material [2]. One of those methods is the drop-and-fill method were randomly sized particles are dropped into a 3-D space, then a simulated gravitational force will settle the particles at the bottom of the 3-D space. The problem with this method is that "the influence of "gravity", leads to interbody collision and contact frictional effects [2]." Another method to randomly distribute and pack particles of arbitrary sizes is by using a combination of Monte Carlo (MC) and Molecular Dynamics (MD) methods. The MC method uses a random number generator based on a chosen probability distribution function to determine different particle sizes. Figure 3 is based on a figure by Dr. Baer [2]. The randomly sized particles from the MC method are placed in a 3-D space and distributed randomly, as shown in Figure 3a). An MD simulation method places particles by giving them a velocity and and allowing them to collide as shown in Figure 3b). This collision dynamics ensure that the particles mix with each other, creating a random distribution.

In order to pack them to a desired volume fraction, the density inside the 3-D space is increased dynamically until the particles are locked in place, Figure 3c) [2].

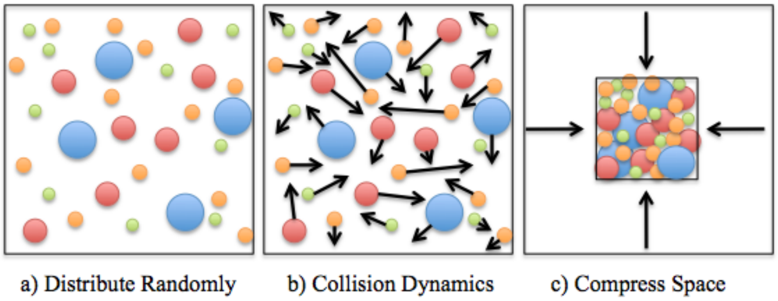

Figure 3. Monte Carlo Method for Randomly Packing Particles

2.3.2 Experimental Measuring Techniques

As mentioned earlier, computational simulations are effective and provide useful approximation, but experimental testing provide more realistic results. Experimental techniques for measurement at the mesoscale are currently in development by organization such as Sandia National Laboratories (SNL). A new technique being explored at SNL is a line-imaging Optically Recording Velocity Interferometry System (ORVIS) to provide data on particle velocity in shock-compressed heterogeneous materials [2]. ORVIS uses electromagnetic waves to measure properties in the shock wave and produces a 3-D line-image of the particle velocity versus time and distance. The time resolution of the ORVIS technique is approximately 3 nanoseconds and a spatial resolution of approximately 3 micrometers. For examples of an ORVIS particle velocity measurement of a compaction wave see work by Dr. Baer [2].

Figure 4a shows a schematic of the line-imaging ORVIS based on a figure from Dr. Ao [1]. The light beam from a moving object, such as a shock wave, is reflected to a series of mirrors and optics to collimate the light. The light signal then pases through a splitter, where the signal either goes to mirror one (M1) or mirror two (M2). The M2 signal gets delayed by a delay etalon and the M1 signal continues with no delay.

Both the signals meet at a crossing plane, shown in Figure 4a and b. The interfering fringes get translated into an output signal of velocity and time [1].

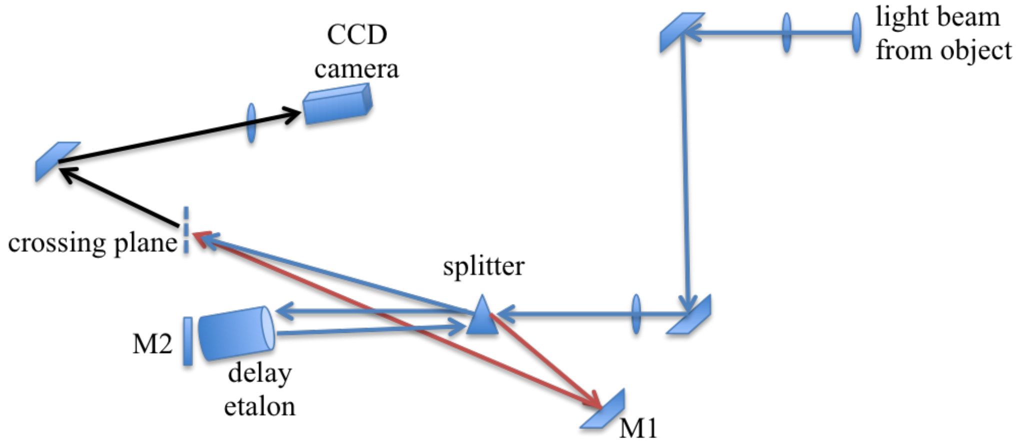

(a) Line-Imaging ORVIS Schematic

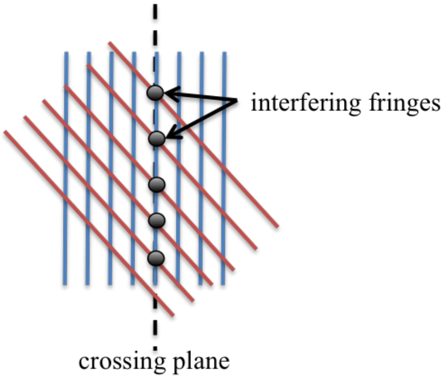

(b) Crossing Plane

Figure 4. ORVIS Schematic and the Crossing Plane

The ORVIS experimental technique opens many possibilities in exploring heterogeneous materials, but there are a few issues with the technique [2]. One of the issues is the large amount of data that is collected needs to be stored, analyzed, and interpreted. SNL is looking at ways to improve the post processing of large amounts of data. Despite the minor drawbacks, this technique shows incredible promise in allowing for the capture of useful data from physical tests, providing a practical alternative to reliance on computational techniques. The combination of simulation and experimental data will allow for a better understanding of the thermal/mechanical/chemical behaviors of heterogeneous explosives.

2.3.3 Explosive Materials with Aluminum Powders

2.3.3.1 Inert Aluminum

The addition of metal particulates in explosives is not a new concept, but there remains a lack of understanding on what occurs in the reaction. Several researchers have developed EOS for metalized explosives in an attempt to computationally model the behavior. Dr. Crochet developed a simulation modeling code, MPEXS, to study the effects of metalized explosives [5]. In particular, he looked at the high explosive HMX and Al by varying initial metal mass fraction (λ_m^o) by 15%, 25%, 50% for Al grain mean diameter (d_m) of $150\mu m$ and $100nm$. As λ_m increases, the amount of solid explosive available for combustion decreases, therefore affecting detonation properties like detonation velocity, pressure, and temperature. For inert metalized explosives, as λ_m^o increases the heat released from the compressive work behind the detonation wave decreases [5]. The heat transfer from the gas phase is mostly influenced by the combustion reaction energy, which is dependent on the aluminum particle size, i.e. d_m [5].

The results for detonation wave speed, end-state pressure, and end-state temperature for the three different metal mass fractions at various metal particle diameters are presented in Dr. Crochet dissertation [5]. It was concluded by Dr. Crochet that the detonation wave speed increases as the mass fraction decreases [5]. Therefore, the amount of Al present in the mixture directly affects the wave speed. As the mass fraction decreases, both pressure and temperature increase. The wave speed, pressure, and temperature remain constant for small aluminum grain sizes until a threshold is met, then it increases. Dr. Crochet suggests that "the influence of size-dependent relaxation processes approach a threshold, beyond which more rapid phase equilibrium has a negligible effect" on wave speed, pressure, and temperature [5].

Dr. Crochet's inert metal model, when compared to the experimental data of Gogulya et al. [11], under predicted the detonation wave velocities for aluminum grain sizes of 20, 50, and 150 microns [5]. One of the factors that is believed to reduce the detonation wave velocity is that as the λ_m^o increases, the explosive gets diluted and combustion energy available decreases [5]. The other factor is as the λ_m^o increases, gas-phase energy decreases [5]. These decreases in energy reduce the detonation wave velocities. For the 500 nm aluminum grain size, the inert metal model over predicted the detonation wave velocity, "possibly due to the simplified form of the drag and heat transfer coefficients" [5].

2.3.3.2 Reactive Aluminum

Dr. Crochet also performed an analysis of reactive metal in the explosive by varying two parameters; the metal grain size d_m and oxidation rate (K_{pr}) [5]. Based on the metal oxidations laws utilized in the simulations, there were three values of K_{pr} tested. Oxidation rates of K_{pr}= $1.9x10^{-9}$ m^2/s and K_{pr}= $1.9x10^{-8}$ m^2/s were taken from suggested values based on Fedorov and Kharlamova's research [5]. The other oxidation rate is that of inert aluminum, K_{pr}= 0 m^2/s [5]. The results of the detonation wave velocity with the two varying parameters, d_m and K_{pr} are presented in Dr. Crochet dissertation [5]. For large aluminum particles, d_m greater than 5 microns, the oxidation prefactor seems not to affect the detonation velocity. Due to a more rapid metal oxidation and heat transfer, it is observed that the detonation velocity increases as K_{pr} increases for d_m less than 5 microns [5]. Similar to the inert metal, there is a threshold of metal particle size, above/below which the size does not affect the detonation velocity.

The study performed by Dr. Crochet consisted on the explosive HMX and aluminum, where aluminum was either inert or reactive [5]. In both of these cases, it was observed that aluminum particle size had a direct impact on many explosive properties like detonation wave velocity, end-state pressure, and end-state temperature. Future work in this area includes improving the refinement of spatial grid utilized near the detonation wave to properly model gas physics, thermal and chemical behaviors.

2.3.4 An Analysis of Shock-Induced Reactions in Fe_2O_3+$Al+Teflon^{®}$ Powder Mixtures: Reactive Material Section

Yang et al [15] conducted a series of experiments to perform a preliminary analysis of shock-induced chemical reactions. The powder mixture for this series of experiments was a mixture of aluminum, hematite (Fe_2O_3), and Polytetrafluoroethylene (PTFE) also known as Teflon®. These powder mixture samples were impacted by a metal "flyer", on impact it sends a shock wave through the powder mixture. This shock wave initiates the chemical reaction and continues to feed the shock wave. There are two Polyvinylidene Fluoride (PVDF) pressure gauges located at different positions between the powder mixture that measure shock pressures . These gauges are utilized to determine what is happening in the chemical reaction, which occurs under the high pressure shock wave loading.

During the Fe_2O_3+Al+Teflon® powder mixture chemical reaction, Yang et al believe that two main reactions occur. One, the reaction between Fe_2O_3 and Al and the other between the Teflon® and aluminum [15]. When aluminum reacts with Teflon® or hematite it produces a gas product of aluminum fluorides (AlF_j), with j representing the number of fluoride atoms present. The variation of shock strength during the propagation in the mixture is thought to be determined by the product gas AlF_j [15]. It was concluded by Yang et al that the AlF_j formed depends on both the shock pressure and temperature in the mixture. As the shock pressure increases, more Fe_2O_3 and Teflon® react with aluminum; therefore reducing the amount of fluoride atoms present in the product gas AlF_j [15].

When dealing with shock induced chemical reactions and explosive reactions, there are many assumptions made due to the complexity and speed of events. In order to simplify the complexity of these problems, the initial assumptions made result in non desired EOS variables and coefficients. Yang et al concluded that the variables describing mechanical and thermodynamic reactants and products may need to be improved [15]. These variables change too fast that chemical equilibriums might not be reached, but it is difficult to determine the state of the reaction. Yang et al also concluded that a further understanding is needed on how to formulate the conditions under which the shock pressure increases and decreases during wave propagation [15].

2.4 Conclusion

The literature reviewed herein served as the foundation for the research described in this document. The main goal of this thesis is to study the effects of aluminum particulates in certain explosive materials via a computational simulation. This chapter included a review of the fundamentals of detonations of explosives included the basic information of the important parameters that are studied in explosives. Also, included in this chapter was a review of current simulation work on heterogeneous explosives with inert and reactive aluminum methods. This chapter included a review on computational procedures to randomize mixtures of particles to simulate as close as possible real explosives.

III. Methodology

3.1 Introduction

The code utilized for the 1-D multi-phase simulation of Al particulates in explosives needs to be consistent with thermodynamic or entropy conditions that exist in the explosive reaction, incorporate the EOS, and the reactive burn models between phases during the reaction. As explained earlier, the effects of metal mass fraction (λ_m) and particle size (d_m) are the parameters of interest. Some modifications to the code might be necessary to properly analyze the effects of different explosive compound formulations. These suggested modifications will be implemented in future versions of the code. Simulations will be performed on several formulations of explosives, different particle grain sizes, and different metal mass fractions. This research will look at the stability of the code by running several tests to determine consistency and limits of the code. This research will look at trends in several detonation properties for metalized PBX9501. In this section a detailed description of the multi-phase code will be presented. Also, the methodology that will be utilized to run the simulations and how the data will be analyzed.

3.2 Multi-Phase Code Modeling

To properly evaluate the effects of aluminum metal particulates in multi-phase explosives, this research will use a 1-D multi-phase computational numerical method code, MPEXS, to simulate the explosion by predicting thermomechanical flow field properties at the macroscopic level. The MPEXS code utilized for this research was developed by Dr. Michael Crochet, a computational researcher at the Munitions Directorate of AFRL. The MPEXS code is an evolving code that will be continuously modified to provide better explosive parameters and ease of use by Department of

Defense (DOD) users. The main goal of this thesis is to use Dr. Crochet's code to evaluate the effects of aluminum in PBX9501, a multi-phase explosive. Other goals are to test the accuracy and performance of the code and provide suggestions to AFRL.

This section will provide an explanation of how the fundamental equations of state were derived for the MPEXS hydrocode. It will provide a description of the relevant input files and subroutines files that the user will modify, how the MPEXS code is executed, and the output files it produces. All other subroutines and equations associated with the code are described in more detail in Dr. Crochet's Ph.D. dissertation [5]. "The code is intended to provide the end user with some flexibility in prescribing equations of state, burn models, and other constitutive relations by utilizing a modular source code structure, where only a limited number of subroutines require user interaction [6]." This "beta" version of the MPEXS hydrocode will be continuously modified until a final version is user friendly and provides the most accurate simulation results for metalized explosives.

There are different models that could be utilized to simulate explosive reactions. The One-Phase Model simulates simple explosions and provide overall flow properties but no information is provided on what occurred in the gas or solid phases. The Two-Phase Model provides flow properties for both the solid and gas phase of the explosion. The Two-Phase Model is utilized for this research to run simulation on simple explosive reactions like PBX9501 with no aluminum particulates. A more complicated model like the Multi-Phase Model with N Solid Components is utilized for this thesis when running simulations with aluminum particulates. The Multi-Phase Model allows the simulation of explosives with more than one solid phase, that is, either multiple solid explosive compounds or an explosive solid compound with a solid metal compound. The following sections provide a more detailed description of the different models to include the derivations of the systems of equations for each.

3.2.1 One-Phase Model

The one-phase model can predict flow properties of simple explosives at both the macro and micro scale. Macro scale is when objects can be seen with the naked eye and micro scale is when objects need a magnification device to see them more clearly. A simple explosive is composed of the explosive material and the gas produced during the reaction. This model follows the basic equations of conservation for inviscid and adiabatic flow. The conservation equations utilized for the one-phase 1-D model are: Equation 10 conservation of mass, Equation 11 conservation of momentum, and Equation 12 conservation of energy [5]. Mass, momentum, and energy is not exchanged between the gas/solid mixture and the environment. Viscosity and thermal conductivity can be ignored because it occurs over a longer time scale than that of an explosion, which occur in a matter of microseconds. Since viscosity and thermal conductivity are ignored, the flow can be described by the Eulerian Conservation Equations 10–12 below:

$$\frac{\partial \overline{\rho}}{\partial t} + \frac{\partial}{\partial x}(\overline{\rho}\,\overline{u}) = 0 \tag{10}$$

$$\frac{\partial}{\partial t}(\overline{\rho}\,\overline{u}) + \frac{\partial}{\partial x}\left(\overline{\rho}\,\overline{u^2} + \overline{P}\right) = 0 \tag{11}$$

$$\frac{\partial}{\partial t}\left(\overline{\rho}\,\overline{E}\right) + \frac{\partial}{\partial x}\left[\overline{\rho}\left(\overline{u}\overline{E} + \frac{\overline{u}\overline{P}}{\overline{\rho}}\right)\right] = 0 \tag{12}$$

where x is position, t is time, $\overline{\rho}$ is mixture density, $\overline{u}$ is velocity, $\overline{P}$ is pressure, and $\overline{E}$ is total specific energy.

In order apply the Euler equations to this system, an EOS must be utilized to close the system. Equation 13 below is a caloric EOS, where specific internal energy is a function of both density and pressure.

$$\overline{e} = \overline{e}(\overline{\rho}, \overline{P}) \tag{13}$$

where $\overline{e}$ is the mixture specific internal energy.

3.2.2 Two-Phase Model

The two-phase model is similar to the one-phase model in that both are for simple explosive and use the conservation equations, but now both phases must me considered. For the two-phase model, a simple reactant/product mixture composes two phases, a solid and a gas phase. The conservation equations are then separated for each component. The volume fraction (ϕ) of each component is included in the equations. Throughout the report both mass fraction (λ) and ϕ are utilized to describe the quantity of aluminum within the high explosive material. Both can be calculated by using a ratio of densities of the materials in the explosive mixture. BN formulated a system of equations for basic two-phase flow explosive modeling, shown by Equations 14–20 [3].

The terms on the right side of Equations 14–19 are called "source terms". The mass source term ($\mathcal{C}$) indicates the mass exchange between the solid and gas phase, the momentum source term ($\mathcal{M}$) indicates the momentum exchange between phases, and the energy source term ($\mathcal{E}$) indicates the energy exchange between phases. The conservation of mass equation for the solid phase, Equation 14, has a positive $\mathcal{C}$ and the conservation of mass equation for the gas phase, Equation 15, has a negative $\mathcal{C}$. These opposite terms between the solid and gas phase indicate that what is gained by one phase must be lost by the other phase or vice versa to maintain conservation. The relationship between phases is applied to the six conservation equations; Equation

14–15, Equation 16–17, and Equation 18–19.

$$\frac{\partial}{\partial t}(\phi_s \rho_s) + \frac{\partial}{\partial x}(\phi_s \rho_s u_s) = \mathcal{C} \quad [3] \tag{14}$$

$$\frac{\partial}{\partial t}(\phi_g \rho_g) + \frac{\partial}{\partial x}(\phi_g \rho_g u_g) = -\mathcal{C} \quad [3] \tag{15}$$

$$\frac{\partial}{\partial t}(\phi_s \rho_s u_s) + \frac{\partial}{\partial x}(\phi_s \rho_s u_s^2 + \phi_s P_s) = \mathcal{M} \quad [3] \tag{16}$$

$$\frac{\partial}{\partial t}(\phi_g \rho_g u_g) + \frac{\partial}{\partial x}(\phi_g \rho_g u_g^2 + \phi_g P_g) = -\mathcal{M} \quad [3] \tag{17}$$

$$\frac{\partial}{\partial t}(\phi_s \rho_s E_s) + \frac{\partial}{\partial x}\left[\phi_s \rho_s u_s \left(E_s + \frac{P_s}{\rho_s}\right)\right] = \mathcal{E} \quad [3] \tag{18}$$

$$\frac{\partial}{\partial t}(\phi_g \rho_g E_g) + \frac{\partial}{\partial x}\left[\phi_g \rho_g u_g \left(E_g + \frac{P_g}{\rho_g}\right)\right] = -\mathcal{E} \quad [3] \tag{19}$$

where x is position, t is time, ϕ_s is solid volume fraction, ϕ_g is gas volume fraction, ρ_s is solid density, ρ_g is gas density, u_s is solid particle velocity, u_g is gas particle velocity, P_s is solid pressure, P_g is gas pressure, E_s is solid total specific energy, and E_g is gas total specific energy. The subscripts s indicates the solid components and subscript g indicates the gas components.

Equation 20 relates the volume fraction exchange in the reaction. The compaction source term ($\mathcal{F}$) associates the inert pore collapse of the granular material during the reaction. Equation 21 states that the volume fraction of solid and gas components must equal to one, assuming there is no other materials or massless voids in the mixture.

$$\frac{\partial \phi_s}{\partial t} + u_s \frac{\partial \phi_s}{\partial x} = \mathcal{F} + \frac{\mathcal{C}}{\rho_s} \quad [3] \tag{20}$$

$$\phi_s + \phi_g = 1 \tag{21}$$

Just like the one-phase model, an EOS for each phase is needed to close the system of Equations 14–20. These EOS are given by Equation 22 and 23.

$$e_s = e_s(\rho_s, P_s) \tag{22}$$

$$e_g = e_g(\rho_g, P_g) \tag{23}$$

where e_s is the solid specific internal energy and e_g is the gas specific internal energy.

In order to develop an accurate model the formulas for the source terms, $\mathcal{C}$, $\mathcal{M}$, and $\mathcal{E}$ must be determined. The formulations for the source terms were derived from the Second Law of Thermodynamics by Bdzil et al. [13]. These source term formulas are shown by Equations 24–26. In these source term equations there are two different parameters of interest. The relaxation coefficients and the partitioning parameters.

Relaxation Coefficients

The relaxation coefficients “control the rate at which the solid and gas pressures, velocities, and temperatures equilibrate [6].” The compaction viscosity (μ_{sg}) is utilized to determine the rate at which the mixture mechanically equilibrates, the drag coefficient (δ_{sg}) is utilized to govern the rate of kinematic equilibration, and the heat transfer coefficient (H_{sg}) is utilized to dictate the rate of thermal equilibration [6]. In a piston impact test, when the piston hits the explosive mixture a detonation wave forms and travels throughout the mixture. At any position in the mixture, after the detonation wave passes the mixture will relax to a lower state. The relaxation coefficients are estimated from explosive empirical relaxation data. The larger these coefficients are, the faster the mixture will equilibrate after the wave passes. The smaller these coefficients are, the longer it will take to equilibrate.

Partitioning Parameters

Partitioning parameters are similar to the relaxation coefficients in the way that they describe the interaction between phases like solid-gas. The partitioning parameters determine the fraction of thermal energy exchange that occurs during different processes like the compaction, chemical reaction, drag, and other additional dissipative processes [6]. The compaction partitioning function (c_{sg}) determines the thermal energy exchange due to the compaction process, the chemical reaction partitioning function (ξ_{sg}) determines the thermal energy exchange due the chemical reaction process, and the drag partitioning function (α_{sg}) determines the energy exchange due to the drag produced by the production of combustion gas [6]. It is recognized "that the original BN model implicitly assigned all dissipation energy from some process to either the gas or solid, which results in nonphysical phase temperature increases. [6]" Equations 24–26 are the formulations for the source terms were derived from the Second Law of Thermodynamics by Bdzil et al. [13].

$$\mathcal{F} = \frac{1}{\mu_{sg}} \phi_s \phi_g (P_s - \beta_s - P_g) \quad [13] \tag{24}$$

$$\mathcal{M} = P_g \frac{\partial \phi_s}{\partial x} + \left[\frac{1}{2}(u_s + u_g) - \alpha_{sg}(u_g - u_s) \right] \mathcal{C} - \delta_{sg}(u_s - u_g) \quad [13] \tag{25}$$

$$\mathcal{E} = u_s\mathcal{M}_s - [c_{sg}(P_s - \beta_s) + (1 - c_{sg})P_g]\mathcal{F} - \left[\frac{1}{2}\alpha_{sg}(u_s - u_g)^2 + \frac{u_s^2}{2}\right]\mathcal{C}$$
$$+ \left\{\xi_{sg}e_s + (1 - \xi_{sg})\left[e_g + P_g\left(\frac{1}{\rho_g} - \frac{1}{\rho_s}\right)\right]\right\}\mathcal{C} + \alpha_{sg}\delta_{sg}(u_s - u_g)^2 \qquad [13] \quad (26)$$
$$+ \mathcal{H}_{sg}(T_g - T_s)$$

where $\mathcal{F}$ is the compaction source term, $\mathcal{M}$ is the momentum source term, $\mathcal{C}$ is the mass source term, $\mathcal{E}$ is the energy source term, μ_{sg} is the compaction viscosity, δ_{sg} is the drag coefficient, H_{sg} is the heat transfer coefficient, α_{sg} is the drag partitioning function, c_{sg} is the compaction partitioning function, ξ_{sg} is the chemical reaction partitioning function, β_{sg} is the inter-granular stress from particles, T_s is the solid temperature, T_g is the gas temperature, and subscript sg indicates the relaxation process between the solid and gas phases.

3.2.3 Multi-Phase Model with N Solid Component

The multi-phase model is derived from the same system of equations as the two-phase model but with the addition of more equations to represent the other added components. The model provides the means to perform simulations with mixtures with multiple solid components. A multiple solid component can be several different combinations of solids. One combination can be a mixture of different particle sizes of the same explosive. Another combination can be a mixture of different explosive components. The combination this research is concerned about is the mixture of explosive and metal mixture. The conservation equations will be the same as the two-phase model but there will be three equations for the gas: conservation of mass, momentum, and energy. There will also be three conservation equations for each solid and one volume fraction equation for each solid. The total number of equations need can be summarized by 3+4N equations, where N is the number of solid components

[6]. For example, this research will focus on one explosive (PBX9501) and one metal solid (Al) mixture that will have a system of eleven conservation equations because of the two solids (N=2). Equations 27–33 were derived from the BN formulated system of equations for this multi-phase model with N number of solid components [3].

$$\frac{\partial}{\partial t}\left(\phi_i \rho_i\right) + \frac{\partial}{\partial x}\left(\phi_i \rho_i u_i\right) = \mathcal{C}_i \quad [3] \tag{27}$$

$$\frac{\partial}{\partial t}(\phi_g \rho_g) + \frac{\partial}{\partial x}(\phi_g \rho_g u_g) = \mathcal{C}_g \quad [3] \tag{28}$$

$$\frac{\partial}{\partial t}(\phi_i \rho_i u_i) + \frac{\partial}{\partial x}(\phi_i \rho_i u_i^2 + \phi_i P_i) = \mathcal{M}_i \quad [3] \tag{29}$$

$$\frac{\partial}{\partial t}(\phi_g \rho_g u_g) + \frac{\partial}{\partial x}(\phi_g \rho_g u_g^2 + \phi_g P_g) = \mathcal{M}_g \quad [3] \tag{30}$$

$$\frac{\partial}{\partial t}(\phi_i \rho_i E_i) + \frac{\partial}{\partial x}\left[\phi_i \rho_i u_i \left(E_i + \frac{P_i}{\rho_i}\right)\right] = \mathcal{E}_i \quad [3] \tag{31}$$

$$\frac{\partial}{\partial t}(\phi_g \rho_g E_g) + \frac{\partial}{\partial x}\left[\phi_g \rho_g u_g \left(E_g + \frac{P_g}{\rho_g}\right)\right] = \mathcal{E}_g \quad [3] \tag{32}$$

$$\frac{\partial \phi_i}{\partial t} + u_i \frac{\partial \phi_i}{\partial x} = \mathcal{F}_i + \frac{\mathcal{C}_i}{\rho_i} \quad [3] \tag{33}$$

where ϕ_i is i-th solid volume fraction, ρ_i is i-th solid density, u_i is i-th solid particle velocity, P_i is i-th solid pressure, and E_i is i-th solid total specific energy. Other expressed symbols with a subscript i denote parameters of the solid components.

The saturation equation, Equation 34, shows the volume fractions for all the i-th solids and the volume fraction for the gas component equals to one.

$$\phi_g + \sum_{i=1}^{N} \phi_i = 1 \tag{34}$$

The "source terms", $\mathcal{C}$,$\mathcal{M}$, $\mathcal{E}$, for all the components are summed by Equations 35–37. These equations indicate there is conservation between all sources. For example, the mass sources, $\mathcal{C}$, are conserved between gas and all solid components.

$$\mathcal{C}_g + \sum_{i=1}^{N} \mathcal{C}_i = 0 \tag{35}$$

$$\mathcal{M}_g + \sum_{i=1}^{N} \mathcal{M}_i = 0 \tag{36}$$

$$\mathcal{E}_g + \sum_{i=1}^{N} \mathcal{E}_i = 0 \tag{37}$$

The i-th solid mass source term ($\mathcal{C}_i$), i-th solid moment source term ($\mathcal{M}_i$), and i-th solid energy source term ($\mathcal{E}_i$) terms can be separated into two contributions; the solid/gas interaction contributions denoted by subscript ig and the solid/solid interaction contribution denoted by subscript im [6]. Equations 38–40 below show the solid/gas and solid/solid interaction contributions to $\mathcal{C}_i$, $\mathcal{M}_i$, and $\mathcal{E}_i$.

$$\mathcal{C}_i = \mathcal{C}_{ig} + \sum_{m=1}^{N} \mathcal{C}_{im} \tag{38}$$

$$\mathcal{M}_i = \mathcal{M}_{ig} + \sum_{m=1}^{N} \mathcal{M}_{im} \tag{39}$$

$$\mathcal{E}_i = \mathcal{E}_{ig} + \sum_{m=1}^{N} \mathcal{E}_{im} \tag{40}$$

The metal utilized for this research will be aluminum and will be treated as a non-reactant metal. Since non-reactant Al will be utilized the terms that include any interaction with Al will not be utilized. In the MPEXS code Al is denoted by subscript m for metal and the explosive is denoted by s. Applying this notation to Equations 38–40 will reduce them to:

$$\mathcal{C}_i = \mathcal{C}_{sg}, \quad \mathcal{M}_i = \mathcal{M}_{sg}, \quad \mathcal{E}_i = \mathcal{E}_{sg}$$

3.2.4 Nozzling Sources

The system of equations formulated by BN for conservation of mass, momentum, and energy of explosive reactions can be written in a general form, shown by Equation 41 [6]. "The mixture entropy inequality gives rise to terms that are proportional to the volume fraction gradient $\partial\phi/\partial x$ [6]." These non-conservative terms which are multiplied by the volume fraction gradients are known as nozzling sources ($\mathbf{g}_i$).

$$\frac{\partial \mathbf{q}}{\partial t} + \frac{\partial}{\partial x}\left[\mathbf{f}(\mathbf{q})\right] = \sum_{i=1}^{N} \mathbf{g}_i(\mathbf{q}) \frac{\partial \phi_i}{\partial x} + \mathbf{s}(\mathbf{q}), \tag{41}$$

where $\mathbf{q}$ is the vector of unknown variables such as ϕ_i, ρ_i, u_i, E_i, $\mathbf{f}$ is a flux vector as a function of $\mathbf{q}$, $\mathbf{s}$ is a vector of algebraic interphase sources as a function of $\mathbf{q}$.

The left side of Equation 41 are the Eulerian conservation equations and the right side are the source term equations. "The approximations resulting from the centered scheme introduce additional numerical error into the solution. This is due to the difficulties associated with discretizing the nozzling sources, which continues to be an active area of mathematical research.[6]" If the nozzling terms are too precise then it becomes computationally expensive, if they they are not precise enough then it will result in a poor approximation.

3.3 Multiphase Explosive Simulation Code Files

3.3.1 Input Files

The MPEXS code is written in the Fortran programming language. The code is composed of several routine and subroutine files. The purpose of the MPEXS code is to allow the user to input the explosive simulation parameters in as few files as possible. The latest version of the MPEXS code has reduced the number of input files needed to run a simulation. Most of the inputs are done in the **maininput.txt** file but there are other inputs that are done in other files. Brief descriptions are given below.

3.3.1.1 maininput.txt

The **maininput.txt** file is is the principal file where most of the simulation changes will be made. The main input file is divided into two sections; Simulation Inputs and Initial Conditions. The main inputs that will be modified are the number of solid species (Nsp), number of discrete computational cells (N_x), left and right domain boundary locations (L1) and (L2), initial reference piston speed (vf0), final simulation time (tfinal), average component grain diameter (dmean), and the types of equations of state (eostypes). The initial conditions section allows the user to modify the volume fraction ϕ of the solids, the density ρ and the pressure P for both the gas and solids.

The MPEXS code can run both neat and metalized explosives. The term "neat" is utilized to refer to homogeneous explosives with no metal particulates. For neat explosive simulations the number of solid species Nsp = 1. By doing so, the code will neglect any aluminum properties in the input files. For metalized explosives set Nsp = 2.

The current version of the MPEXS code has five different equations of state; Ideal

(0), Virial (1), Mie-Grüneisen (2), Wide-Ranging-Reactant (4), and Wide-Ranging-Product (5). The Ideal EOS are applied to ideal gases in many flow regimes. Virial EOS are applied to non-ideal gases like detonation products of explosives. Mie-Grüneisen EOS applies relationships between pressure and volume of solids like the metal particulates.

The equations of state can be selected on line # 52 of the **maininput.txt** file. The unreacted explosive PBX9501 will use the Wide-Ranging-Reactant equations of state, number (4). The granular aluminum will use the Mie-Grüneisen equations of state, number (2). The gaseous combustion products will use the Wide-Ranging-Product equations of state, number (5). When running cases with pure PBX9501 explosive without aluminum, the equations of state are called in line # 52. This is done by setting eostypes = 4, 5, 0. The first number is the unreacted explosive, the second number is the gaseous products, and the third number is a place holder. The third number will not be read because Nsp is set to 1 for pure explosive simulations. When running cases with PBX9501 and aluminum, line # 52 will be set to eostypes = 4, 2, 5. The first number is the unreacted explosive, the second number is the aluminum, and the third number is the gaseous products.

3.3.1.2 timemarch.f90

This subroutine steps the solution forward in time using a 2nd order Strang splitting method, which alternates between the convective and local source portions of the solver [6]. The most input in this file is the frequency data is stored. The default is that a **fort.xxx** file is saved every 10 time steps. This input is found in line # 64 that reads as follows: "$IF(MOD(j,10) == 0.OR.j == N_t s)THEN$". An analysis will be performed to determine if the amount of data collected is worth the increase in accuracy.

3.3.1.3 ppoutput.txt

The post processing output file, **ppoutput.txt**, is a self generated file needed to calculate the detonation wave speed. This file is stand-alone and can be modified to determine the wave speed at different times intervals by changing the range of **fort.xxx** files. If the MPEXS code stops before the run is completed, the post processing subroutine will not generate the detonation wave speed data. In that case, the inputs can be manually entered and be able to calculate detonation wave speeds. The following are the inputs; number of discrete grid points, number of condensed phases, number of output text files, number of time steps, piston velocity, and domain length.

3.3.1.4 postprocess.f90

This subroutine performs the detonation wave speed calculations after all the output files have been created. This subroutine is can also be utilized as a stand-alone program if the output files have already been created. One input is the threshold pressure. This threshold pressure is utilized to differentiate between a passing detonation wave and a compaction wave. When the threshold is meet, the leading wave position at each recorded time will be stored in the **wavespeeddata.txt** file. The threshold pressure requires some trial and error to set it properly for detonation waves. If too large then no wave will be detected and if too low then it will detect any pressure rise even if it is not a detonation wave. Another input is the number of points utilized for the linear fit that determines the detonation wave speed. The more points utilized the better the linear fit. If too many points are use the result will be inaccurate because non steady state points will be utilized.

3.3.2 Execution Files

The MPEXS hydrocode is executed by using the Linux command terminal. The **binscript.sh** shell script is utilized to execute all the subroutines and input files. As the code runs, the current time and time step is displayed on the terminal screen. The data displayed on the terminal screen is useful to determine if the code is running properly. The data is saved in **fort.xxx** files every 10 time steps which is the default but it can be changed under the **timemarch.f90** file.

3.3.3 Output Files

The data is saved to output files named **fort.xxx**. The“xxx” is a number sequence that begins at 100 and increases by one for each set of data. Each set of data is collected every 10 time steps and it depicts what is happening at that time step. The **fort.101** file will contain data at the 20th time step, **fort.102** will contain data at the 30th time step, and so on. The **fort.xxx** files contain columns of data for time, position, density, pressure, temperature, volume fraction, and particle velocity. Table 1 shows the names corresponding to each column of data for a neat explosive simulation which includes the explosive solid and gas reaction products. Table 2 shows the names corresponding to each column of data for a metalized simulation which include the explosive solid, the metal solid, and the gas reaction products.

Table 1. Fort.xxx Columns for Two Components (Explosive solid, Gas products)

1	2	3	4	5	6	7	8	9	10	11	12
t	x	ρ_e	ρ_g	P_e	P_g	T_e	T_g	ϕ_e	ϕ_g	u_e	u_g

where t is time in microseconds, x is position in millimeters, ρ is density in kilograms per meters cubed, P is pressure in Pascals, T is temperature in Kelvin, ϕ is volume fraction, and u is particle velocity in kilometers per second. Subscript “e” represents explosive solid and “g” represents gas products.

Table 2. Fort.xxx Columns for Three Components (Explosive solid, Metal solid, Gas products)

1	2	3	4	5	6	7	8	9	10	11	12	13	14	15	16	17
t	x	ρ_e	ρ_m	ρ_g	P_e	P_m	P_g	T_e	T_m	T_g	ϕ_e	ϕ_m	ϕ_g	u_e	u_m	u_g

where t is time in microseconds, x is position in millimeters, ρ is density in kilograms per meters cubed, P is pressure in Pascals, T is temperature in Kelvin, ϕ is volume fraction, and u is particle velocity in kilometers per second. Subscript “e” represents explosive solid, “m” represents metal solid, and “g” represents gas products.

The **wavespeeddata.txt** file is a compilation of data collected from all the **fort.xxx** files. The time and position of the shock wave is collected from each **fort.xxx** file by setting a threshold pressure to detect when the shock wave has passed. The time and position are saved into a separate file named **wavespeeddata.txt**. Table 3 below provides an example of the data contained in the **wavespeeddata.txt** file. The data is stored in four columns. The first column it the time when the shock wave passes, the second column is the position of the shock wave in the explosive particles, the third column is the position for the metal particles, and the forth column is the position for the gas particles.

Table 3. Wavespeeddata.txt Example

$t(\mu s)$	$x_e(mm)$	$x_m(mm)$	$x_g(mm)$
0.34355E2	0.1353	0.1359	0.1346
0.34477E2	0.1365	0.1365	0.1359

In some cases a detonation will not occur and only the wave due to the impact of the piston will go through. This wave is called the compaction wave. Detonation wave velocities are much larger than compaction wave velocities and will be noticeable when a detonation does not occur. The goal is to choose a velocity threshold large enough that will detect the detonation wave but ignore the compaction wave. The **wavespeeddata.txt** data provides the time and position of the wave. When plotted the detonation wave velocity for the explosion can calculated with the slope of the line $\partial x/\partial t$. Since the piston face is utilized as the reference, the piston velocity must be added to the wave velocity. The piston and wave velocities will give the detonation velocity.

3.4 Simulation Run Setup

In order to study the effects of aluminum particulates on the detonation velocity of explosives, computational simulations must be performed with various particle size and mass fractions. This research will focus on the high explosive compound PBX9501. The first step is to test the fidelity of the MPEXS code on a simple explosive like PBX9501 with no aluminum particulates, this will be referred as neat PBX9501. If the simulation results for neat PBX9501 have a good correlation with empirical results, then the second step is to run simulations with aluminum particulates. Comparing simulation data to empirical data does not provide any benefit to this research due to the complexity of plastically bonded explosives like PBX9501. The detonation properties are different for every batch made due to the purity and curing process of the binding material can vary from batch to batch. Instead of comparing simulation data to empirical data, this research will look at the stability of the code by running several tests to determine consistency and limits of the code. This research will look at trends in several detonation properties for metalized PBX9501.

AFRL Munitions Directorate currently uses spherical aluminum particulates manufactured by Toyal America Inc [12] in explosive mixtures being tested. Toyal manufactures a range of aluminum powers in different diameters for aerospace and military applications. Toyal manufactures six different sized aluminum powders with a mean diameter D_{50} ranging from 9 to 34 microns [12]. The six different diameters will be utilized as a varying parameter for the computational simulations of this research.

Another parameter that will be varied is the mass fraction (λ) of aluminum to the solid explosive. Increasing the mass fraction of the aluminum will decrease the mass fraction of the solid explosive. A decrease in the amount of explosive available for the reaction will affect detonation properties such as detonation velocity, run-to-detonation time, and run-to-detonation location. Three different mass fractions will be studied for this research; 10, 15, and 20 percent.

Figure 5 below shows the two varying parameters that will be studied, aluminum mass fraction and aluminum mean diameter. The first set of simulations that will be performed will be with neat PBX9501. The data from these simulations will utilized verify that the equations of state in the MPEXS hydrocode are correct. The verification of the MPEXS code can be done by comparing run-to-detonation results to other hydrocodes. The next set of simulations will consider different cases of PBX9501 with aluminum. The six aluminum diameters will be tested for each aluminum mass fraction. For example, the aluminum mass fraction of 10 percent will be tested with 9, 13, 19, 23, 29, and 34 micron diameter. The same simulations will be performed for 15 and 20 percent.

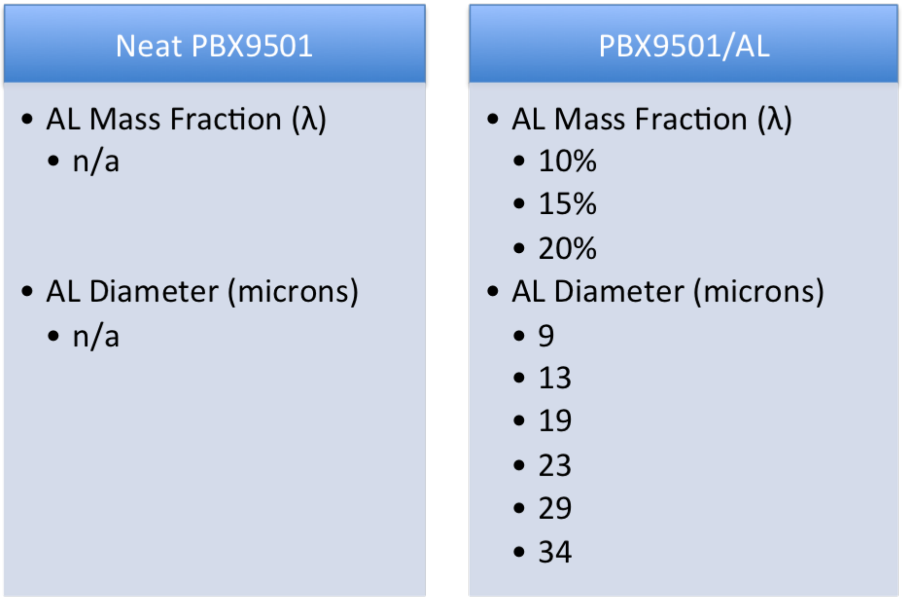

Neat PBX9501

- AL Mass Fraction (λ)
  - n/a
- AL Diameter (microns)
  - n/a

PBX9501/AL

- AL Mass Fraction (λ)
  - 10%
  - 15%
  - 20%
- AL Diameter (microns)
  - 9
  - 13
  - 19
  - 23
  - 29
  - 34

Figure 5. Varying Parameters for Simulation Runs

3.5 Neat Explosive Simulations

Two things must be considered before the study of the effects of metalized explosives; the validity of the MPEXS code and a baseline of initial parameters to be utilized. In this section, different computational cell quantities and different piston speeds will studied with the purpose to determine a baseline of initial parameters to be utilized for metalized explosives.

For the neat explosive simulations, data will be collected at different piston speeds (u_p) and at different number of discrete computational cells (Nx) for both PBX9501 and HMX explosives. Simulations with small number of computational cells will run in a shorter time but the resolution will be lower. The lower resolution might miss important data points specially at the location of the shock wave. Simulations with very large number of computational cells will provide a higher resolution with more data points around the shock but will take longer to run. Besides run time and resolution, the amount of data output per simulation is an another important consideration. The more computational cells the more output files the code will produce. Simulation run time is not as important, but data output is important. Therefore, a study will be performed to determine if the higher resolution simulations are worth the data each simulation will output based on the percent difference for each number of computational cells. Detonation properties can vary depending on the impact speed of the piston. A study will be performed to determine what piston speed will provide the best results and what piston speeds will cause the code to fail.

For the two initial studies, computational cells and piston speed, a low, medium, and higher limit will be tested to gauge the detonation properties of neat explosives. For computational cell, runs with 800 and 2000 cells will be the lower and higher limits to be tested. For piston speed, runs with 0.5, 1.0, 2.0 km/s will be tested. Both the computational cell quantity and piston speed studies are described in more detail in the following sections.

3.5.1 PBX9501 at Different Computational Cell Quantities

Two different number of discrete computational cells will be considered for each explosive, 800 and 2000 cells. The purpose is to determine the amount of cells needed to obtain good results and if the run time and data storage of the simulation is worth the resolution. In this case, the explosive PBX9501 was simulated at three different piston speeds and the two computational cell quantities with the focus of comparing results for 800 and 2000 cells. Larger numbers of computational cell sizes such as 2400, 2500, 3000 cells were tested but the code did not run with the current parameters. It is believed that computational limits on the computer were reached and the computer aborts the code. This issue will be discussed in Results chapter after the code is run on the Air Force Institute of Technology (AFIT) computer cluster and the results are analyzed. There are five detonation properties that are considered through out this research; density, pressure, temperature, particle velocity, and volume fraction of the solids and gas.

When the simulation was run at a piston speed of $u_p = 0.5\ km/s$ the results did not seemed to vary from 800 to 2000 computational cells for density, pressure, temperature, particle velocity, and volume fraction. Simulations with 800 cells took around 13 minutes to run and stored about 746 MB. Simulations with 2000 cells took around 78 minutes to run and stored about 4.6 gibibyte (GiB). As a reference, 1.0 gibibyte equals 1.07374 gigabytes. These run times and storage sizes are for neat explosive, where no Al is present. Figure 6a shows pressure versus position for 800 computational cells and Figure 6b shows the same plot for 2000 computational cells. As seen in the figures the plotted data looks identical. When the data is compared, it can be seen that there is a 1.5% difference between 800 cells and 2000 cells. The number of computational cells utilized for 0.5 km/s makes a very small difference in the results. A generalized conclusion about the effects of computational cells can not be made at this point based on the results because the detonation did not reach steady state. There are two options, either run the simulation for a longer time or increase the piston impact speed. To keep the position domain consistent, faster piston speeds were considered and are discussed in the next paragraph.

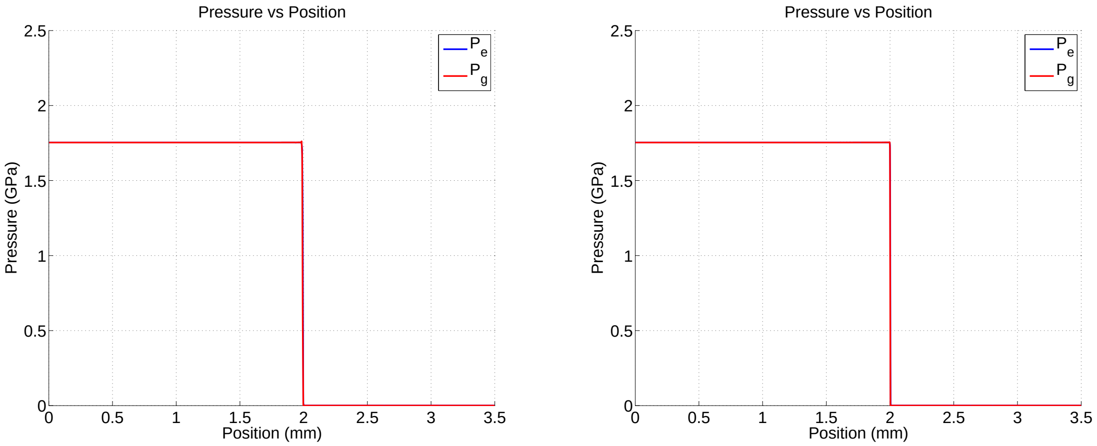

(a) PBX9501 u_p0.5 800cells (b) PBX9501 u_p0.5 2000cells

Figure 6. PBX9501 P vs X Piston Speed = 0.5 km/s

Since steady state was not reached within the position domain for piston speed of 0.5 km/s, the piston speed was increased. Simulations with piston speeds of 1.0 and 2.0 km/s were performed for PBX9501. The focus is on the grid resolution therefore the same computational cells, 800 and 2000, were utilized for the faster piston speeds. 800 and 2000 computational cells were utilized for the simulations with faster piston speeds. Since the results for 1.0 km/s and 2.0 km/s are similar when varying computational cell sizes, only the 2.0 km/s case will be presented and discussed here. The results for density, pressure, particle velocity, and volume fraction were almost identical when 800 and 2000 computational cells are compared. For 1.0 and 2.0 km/s the detonation reached a steady state. Figure 7a and Figure 7b show pressure vs position for both cases. Comparing the results for the two cell sizes it is calculated there is a 1.0% difference in pressure results, 0.8% difference for particle velocity, 1.5% difference for density, and 0.0% difference for detonation velocity. The difference is small enough that it can be concluded that computational cells sizes do not affect these detonation parameters.

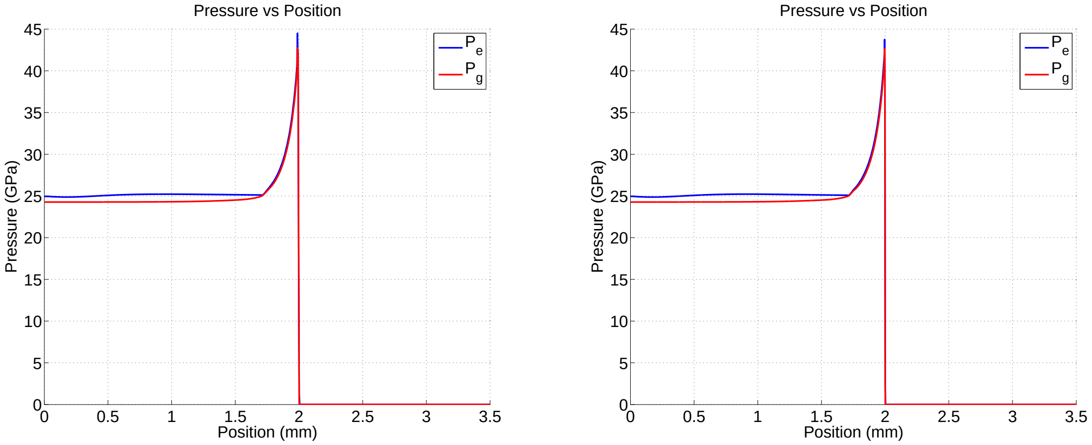

(a) 9501 u_p2.0 800cells

(b) 9501 u_p2.0 2000cells

Figure 7. 9501 P vs X Piston Speed = 2.0 km/s

As seen in Figure 8a and 8b, the temperature of the explosive particles has a higher spike when 2000 computational cells are utilized versus the 800 cells. The thin region behind the detonation wave is typically very small compared to the grid sizes utilized. The more computational cells utilized, the finer the grid size gets and more data can be captured in this region. The case with 2000 cells provides more detail in this region and shows that the temperature is actually higher. When less computational cells are utilized, some of the higher temperature data points are skipped, therefore showing a lower temperature. Another observation for temperature vs position is that the transition to equilibrium after the shock passes is smoother with 2000 computational cells. The smoother transition is also due to the increase of data points per unit distance.

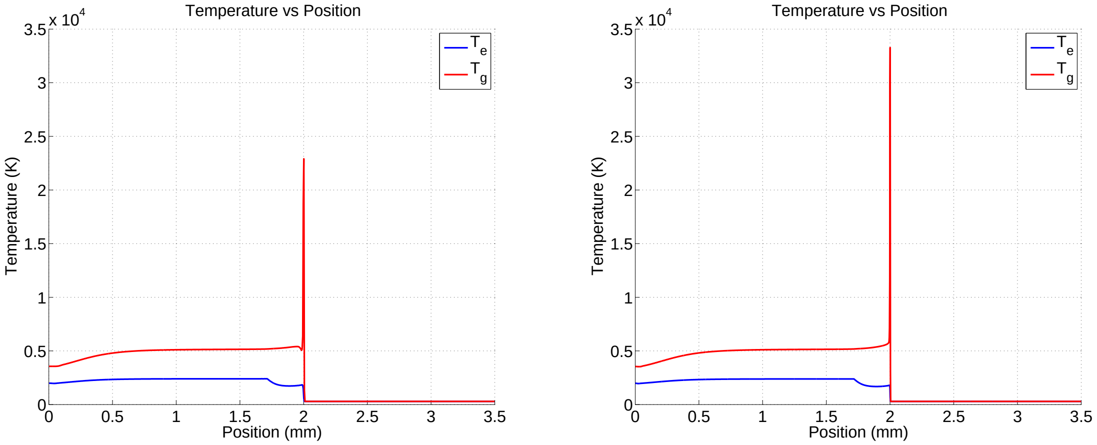

(a) 9501 u_p2.0 800cells

(b) 9501 u_p2.0 2000cells

Figure 8. 9501 T vs X Piston Speed = 2.0 km/s

The results showed there was repeated trends and consistent results between the two different computational cell sizes. There were no abnormal results between the two cell sizes. These results help validate that the code is providing consistent and predictable results.

3.5.2 HMX at Different Computational Cell Quantities

Neat explosive HMX was also studied at different piston speeds and two different computational cell quantities, 800 and 2000 cells. To compare both the computational cell quantities a piston speed of 0.5 km/s was considered first. The simulation of neat HMX with a piston speed of 0.5 km/s showed a 2.2% difference between 800 and 2000 cells in particle velocities, 0.7% difference in temperatures, 1.7% difference in pressures, 0.3% difference in densities, and 2.3% difference in detonation velocities. Figure 9 shows a comparison between 800 and 2000 cells for temperature vs position of HMX. Both the HMX and PBX9501 simulations at 0.5 km/s showed that there is a very small difference between 800 and 2000 computational cells. Based on the results for a piston speed of 0.5 km/s, the detonation did not reach steady state.

No conclusions can be made from these results about the different cell quantities. To make a good comparison of computational cell sizes, higher piston speeds were considered.

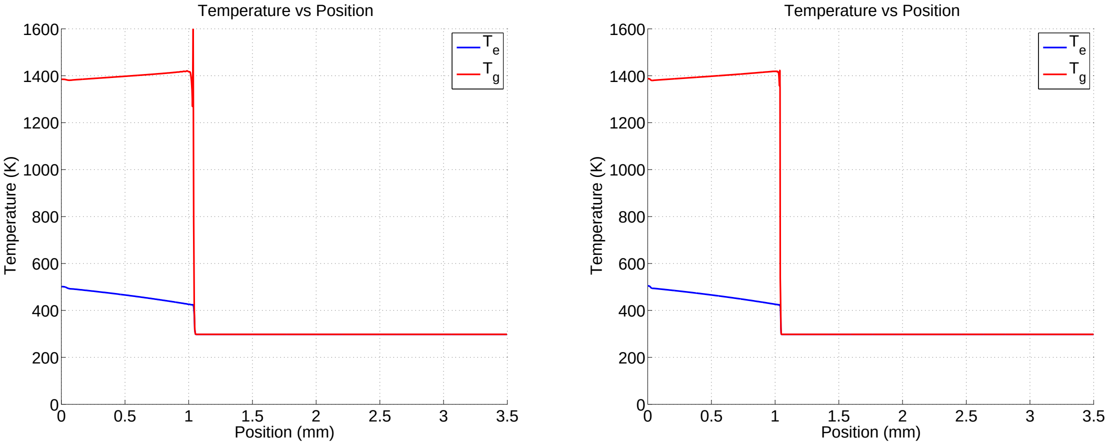

(a) HMX u_p0.5 800cells

(b) HMX u_p0.5 2000cells

Figure 9. HMX T vs X Piston Speed = 0.5 km/s

The results of the simulations for neat HMX with piston speed of 2.0 km/s had less than 2% difference from 800 to 2000 computational cells for density, pressure, particle velocity, and volume fraction. The only parameter that displayed a difference between 800 to 2000 cells was temperature as seen in Figure 10. For the 2000 computational cell simulation, the temperature reached a higher temperature and had a smoother transition behind the shock. Like the PBX9501 simulation, the smoother transition and higher temperature is due to the larger number of data points per unit length when 2000 cells are utilized.

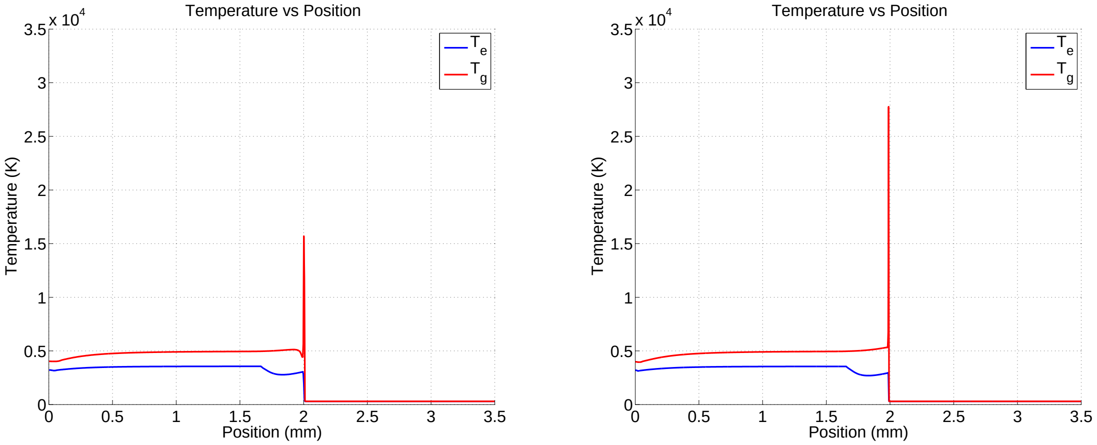

(a) HMX u_p2.0 800cells

(b) HMX u_p2.0 2000cells

Figure 10. HMX T vs X Piston Speed = 2.0 km/s

Based on this study for neat explosive simulations, it is shown that 2000 cells will increase the resolution by adding more data points, but it will require more data storage. 800 cells provided less precise results but it required less storage. The difference in the results between 800 and 2000 cells is within 1% to 2%. Running the simulations with 800 cells is a better option for faster and quick checks of detonation properties because it will require less data storage. The larger data storage of 2000 cells might be an issue with the metalized explosive simulations but with neat explosives is not a issue. Therefore, 2000 cells will be utilized for studying the different speeds of neat explosives in the next section.

3.5.3 PBX9501 at 3 Different Piston Speeds

From the previous study it was determined that a good starting resolution was 2000 computational cells. The following simulations will look at the effect of different piston speeds to determine the best piston speed for the metalized explosive simulations. It is important to get a good understanding of the neat explosive detonation properties before the addition of metal particulates.

Three different piston speeds were chosen for the following simulations, all with 2000 computational cells. Piston speeds of 0.5 km/s, 1.0 km/s, and 2.0 km/s. All five detonation properties were compared at each of the piston speeds. The detonation properties are: density, pressure, temperature, particle velocity, and volume fraction.

Figure 11 plots the volume fraction vs position for the three different piston speeds. Figure 11a shows that volume fraction does not transition from explosive solid to gas for the $u_p = 0.5$ case. The explosive volume fraction should exponentially decay to zero and the gas volume fraction should exponentially increase to the total solids volume fraction as shown in Figures 11b and 11c. As discussed earlier, for piston speed of 0.5 km/s the detonation wave is developing and does not reach steady state for the time and position domain considered. Figure 11c is a good example of a detonation wave that has reached its steady state. Figure 11b is almost at steady state but not quite there. Steady state is reached when the explosive solid decays to zero very sharply and does not change.

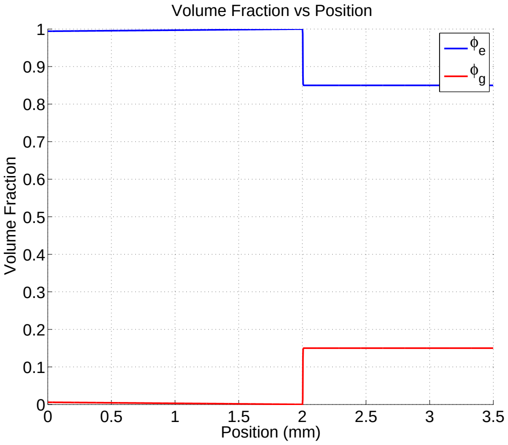

(a) PBX9501 u_p0.5 2000grid

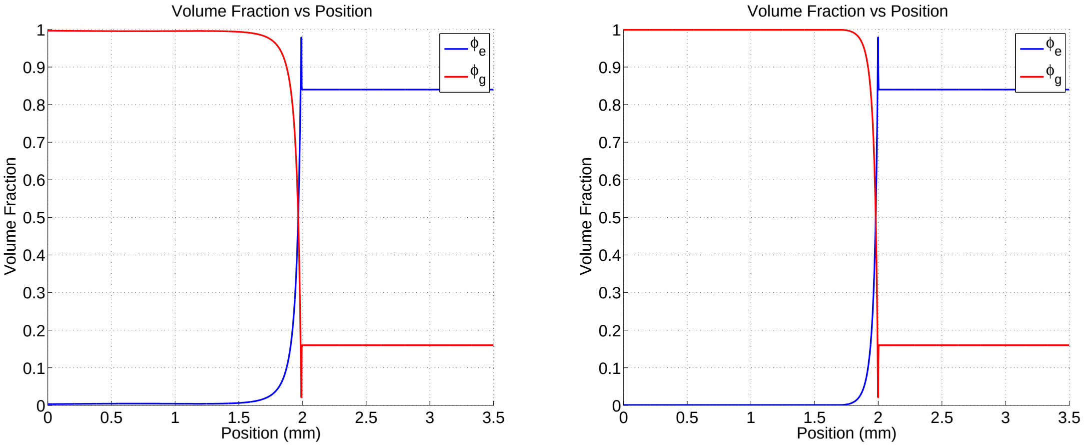

(b) PBX9501 u_p1.0 2000grid

(c) PBX9501 u_p2.0 2000grid

Figure 11. PBX9501 Volume Fractions

The rise in density for the $u_p = 0.5\ km/s$ case is due to the compression wave caused by the impact of the piston. The small rise in density indicates the piston speed was not fast enough to reach steady state within the time and position domain.

Since steady state was not reached at $u_p = 0.5\ km/s$, the piston speed was increased to 1.0 km/s and 2.0 km/s. The results for $u_p = 1.0\ km/s$ and 2.0 km/s are shown in Figure 12b and 12c. For these faster speeds it can be seen that a detonation occurred because there is a larger increase in density as the shock wave passed. The peak density for the gas is 2437 kg/m^3 at $u_p = 1.0\ km/s$ and 2484 kg/m^3 at $u_p = 2.0\ km/s$. The biggest difference between the two speed is the rate the rarefaction wave reaches equilibrium. The $u_p = 2.0\ km/s$ simulation reaches equilibrium at a faster rate and the $u_p = 1.0\ km/s$ simulation at a slower rate. Figure 12b shows a smoother more gradual decrease to the equilibrium state and Figure 12c a sharper drop to equilibrium state.

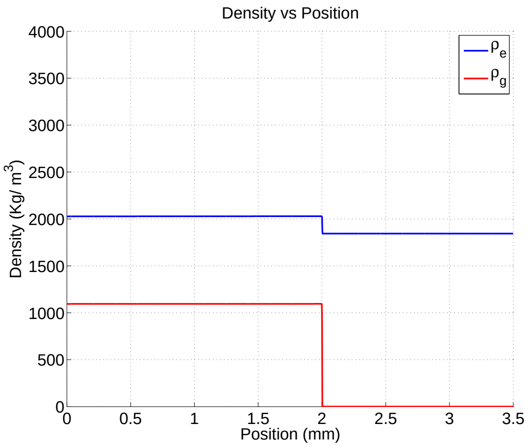

(a) Density vs X $u_p = 0.5$

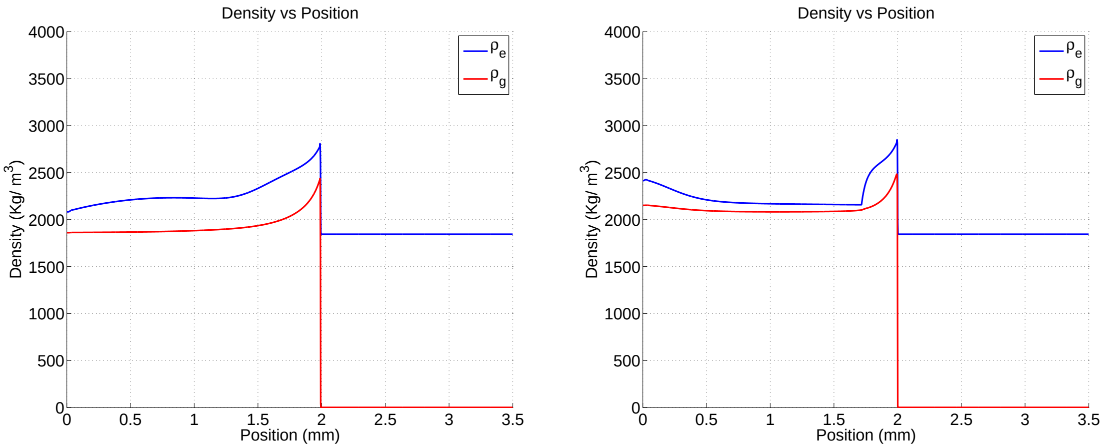

(b) Density vs X $u_p = 1.0$

(c) Density vs X $u_p = 2.0$

Figure 12. PBX9501 Density vs X 3 Speeds

Pressure versus position is plotted for the three piston speeds and the results are shown in Figure 13. The same patterns as density are seen for pressure, were steady state is not reached at $u_p = 0.5\ km/s$ and a steady state detonation occurs for the faster piston speeds. The peak pressure for the gas is 38.86 GPa at $u_p = 1.0\ km/s$ and 42.64 GPa at $u_p = 2.0\ km/s$. Piston speed directly affects the detonation properties like pressure. When the piston speed was increased, the pressures also increased. In Figure 13b, the rarefaction wave for $u_p = 1.0\ km/s$ has a more gradual drop in pressure. Figure 13c shows the rarefaction wave for $u_p = 2.0\ km/s$ has a sharper drop in pressure and then equilibrates.

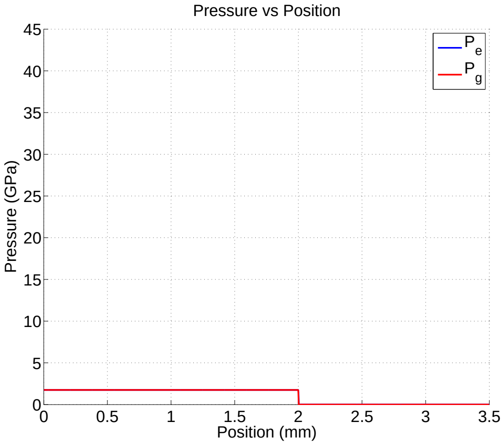

(a) Pressure vs X $u_p = 0.5$

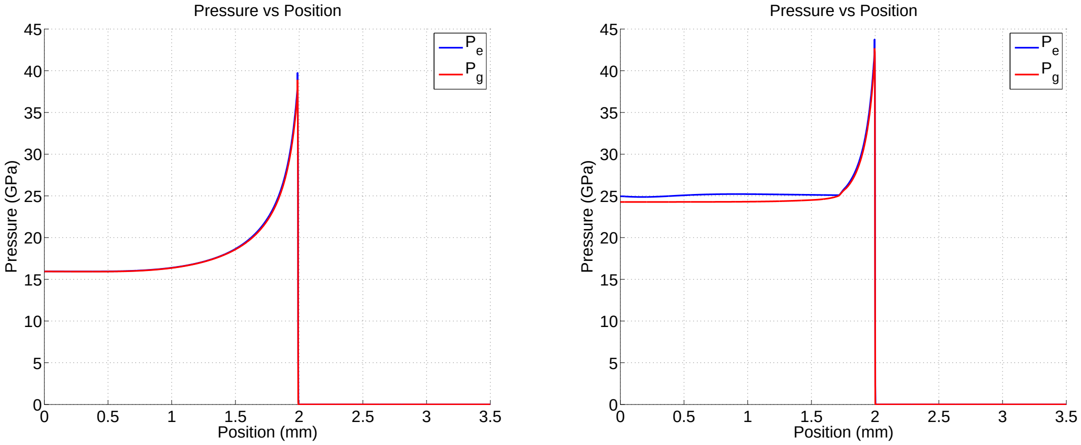

(b) Pressure vs X $u_p = 1.0$

(c) Pressure vs X $u_p = 2.0$

Figure 13. PBX9501 Pressure vs X 3 Speeds

The relationship between the three speeds is the same the remaining properties like temperature, particle velocity, and volume fraction. The correlation between piston speed and detonation properties is that as piston impact speed increases, the detonation properties increase. Higher piston speeds resulted in higher pressure, temperature, particle velocity, and detonation velocity. For brevity of the report some of the key detonation property values for PBX9501 at the three piston speed are shown in Table 4.

Table 4. Neat PBX9501 Detonation Properties for Different Piston Speeds

Piston Speed, u_p (km/s)	**Pressure, Pg** (GPa)	**Temperature, Tg** (K)	**Part. Velocity, Ug** (km/s)	**Det. Velocity, D** (km/s)
0.5	2.07	969	0.576	2.252
1.0	38.86	29170	3.357	7.842
2.0	42.64	33280	3.594	7.842

3.5.4 HMX at 3 Different Piston Speeds

The same analysis was performed for the neat HMX at three different piston speeds; 0.5 km/s, 1.0 km/s, and 2.0 km/s. When the piston speed was increased, neat HMX had the detonation properties trends as neat PBX9501. As the piston speed increased the pressure, temperature, particle velocity, and detonation velocity also increased. A summary of the results for neat HMX is on Table 5.

Table 5. Neat HMX Detonation Properties for Different Piston Speeds

Piston Speed, u_p (km/s)	**Pressure, Pg** (GPa)	**Temperature, Tg** (K)	**Part. Velocity, Ug** (km/s)	**Det. Velocity, D** (km/s)
0.5	2.35	1115	0.585	2.629
1.0	33.38	22740	2.716	7.799
2.0	36.76	27760	2.869	7.968

3.5.5 Neat PBX9501 and Neat HMX Detonation Properties Comparison

The previous two sections looked at both neat PBX9501 and neat HMX individually to determine how computational cells and piston speed affected detonation properties for each explosive. This section will focus on comparing detonation properties between PBX9501 and HMX at a piston speed of 2.0 km/s and 2000 computational cells. If the code is running correctly then the detonation properties for PBX9501 and HMX should have similar trends.

Figure 14 below plots the the density vs the position for both PBX9501 and HMX at piston speed of 2.0 km/s and 2000 computational cells. The density of the explosive material as the detonation wave passes is higher for PBX9501. The stable density values of the rarefaction wave for PBX9501 are higher as well.

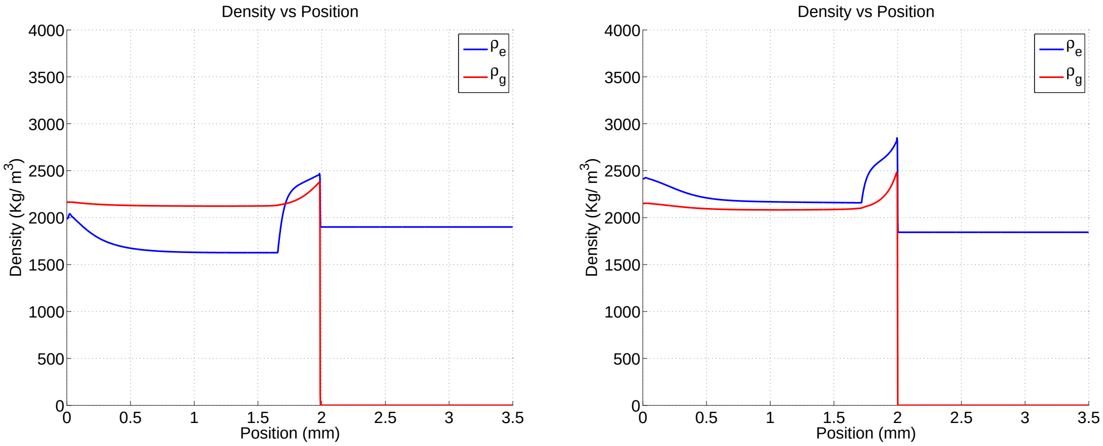

(a) HMX u_p2.0 2000grid

(b) 9501 u_p2.0 2000grid

Figure 14. HMX and 9501 ρ vs X Piston Speed = 2.0 km/s

Figure 15 plots the pressure vs position of both HMX and PBX9501. The pressure for PBX9501 is higher than the pressure for HMX. The peak pressure for PBX9501 is higher than that of HMX at piston speed of 2.0 km/s, 2000 cells.

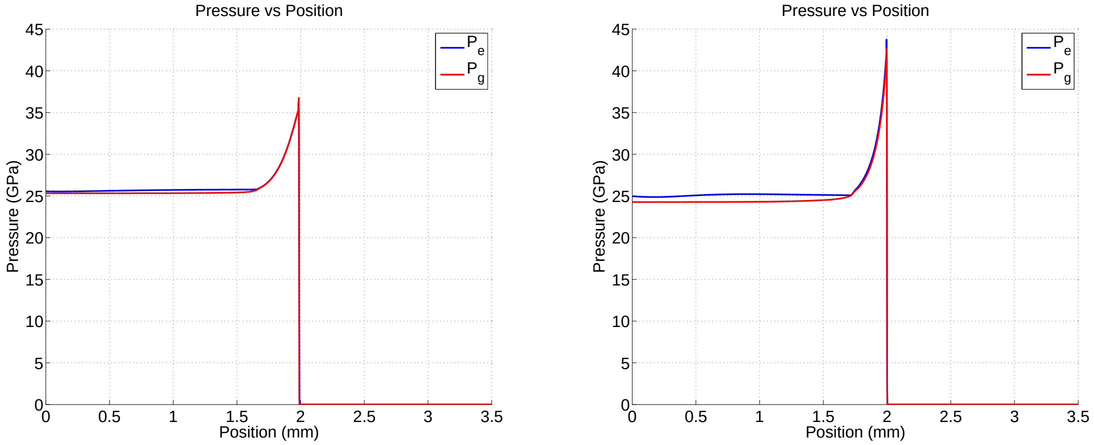

(a) HMX u_p2.0 2000grid (b) 9501 u_p2.0 2000grid

Figure 15. HMX and 9501 P vs X Piston Speed = 2.0 km/s

Figure 16 plots the temperature vs position of both HMX and PBX9501. The temperature for PBX9501 is higher than the temperature for HMX. The peak temperature for PBX9501 is higher than that of HMX at piston speed of 2.0 km/s, 2000 cells.

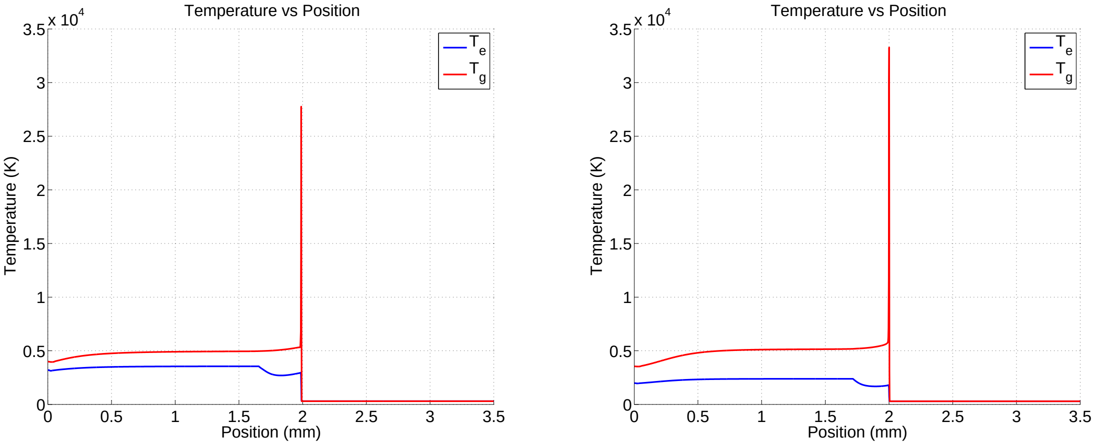

(a) HMX u_p2.0 2000grid (b) 9501 u_p2.0 2000grid

Figure 16. HMX and 9501 T vs X Piston Speed = 2.0 km/s

Figure 17 plots the velocity vs position of both HMX and PBX9501. The velocity for PBX9501 is higher than for HMX. The peak particle velocity for PBX9501 is higher than that of HMX at piston speed of 2.0 km/s, 2000 cells.

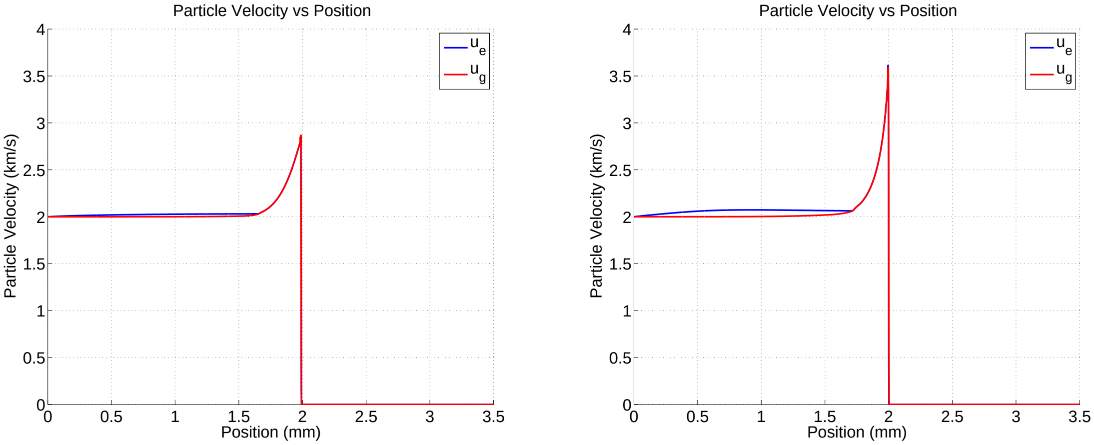

(a) HMX u_p2.0 2000grid

(b) 9501 u_p2.0 2000grid

Figure 17. HMX and 9501 u vs X Piston Speed = 2.0 km/s

Figure 18 plots the volume fraction vs position of both HMX and PBX9501. The volume fraction for both HMX and PBX9501 are very similiar if not the same. The detonation for both explosives are at steady-state and the volume fractions should be at zero for the explosive solid and at one for the gas products after the detonation wave has passed.

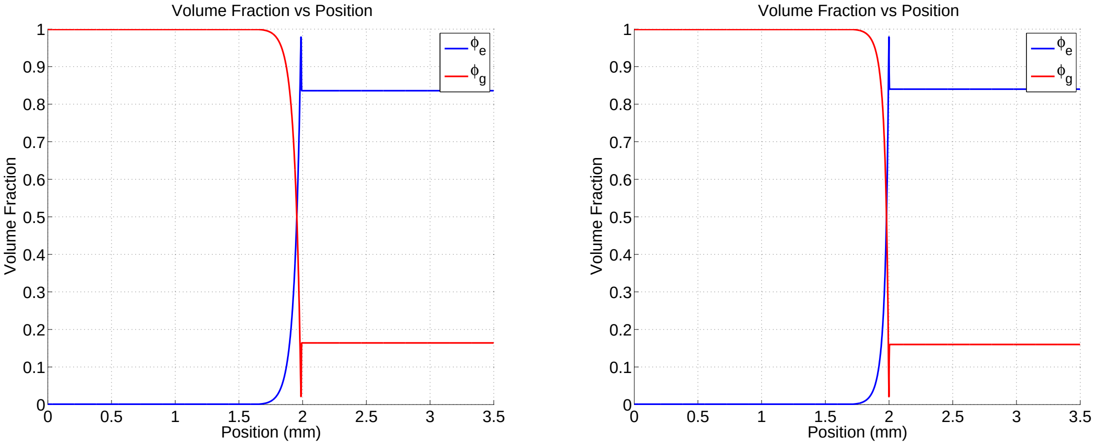

(a) HMX u_p2.0 2000grid

(b) 9501 u_p2.0 2000grid

Figure 18. HMX and 9501 ϕ vs X Piston Speed = 2.0 km/s

Neat PBX9501 explosive is polymer bonded explosive that is composed of 95% HMX and bounded together by 2.5% estane and other materials. The addition of estane-based binder material in PBX9501 adds more fuel to the chemical reaction and can be clearly seen in the stoichiometry equations. The stoichiometry calculations show that more fuel is available to the reaction due to the binder materials. Detonation properties such as pressure, temperature, density, and particle velocity are all affected by the addition of the binder material. This effect was seen in Figure 14 to Figure 18. The binder material retards the burn rate of the explosive and this retardation makes the reaction last longer in which increases the detonation properties like density, pressure, temperature, and particle velocity.

3.6 Metalized Explosive Simulations

3.6.1 PBX9501/Al at Different Computational Cell Quantities

A few cases with metalized PBX9501 explosive were done to determine the accuracy of the higher resolution simulations and how much data storage is needed for each metalized explosive simulation. Simulations with PBX9501 and aluminum were performed at a piston speed of 1.5 km/s, 10% Al mass fraction, and 9μm and 34μm Al particle diameter. Also, simulations at $u_p = 1.5$ km/s, 20% Al mass fraction, and 9μm Al particle diameter. These three simulations will cover a good range of the cases that will be run for the results chapter.

Figure 19 below plots pressure vs position for 10% Al mass fraction and 9μm to compare 800 and 2000 cell simulations. Figure 20 below plots temperature vs position for 10% Al mass fraction at 9μm to compare 800 and 2000 cell simulations. As seen in Figure 20, the gas temperatures rapidly increase to values outside the chart range. This large spike in gas temperature are consequence of the computational model utilized for the simulations. The large spike were also seen by other researchers like Schwendeman, Wahle, and Kapila as described in Dr. Crochet's dissertation [5].

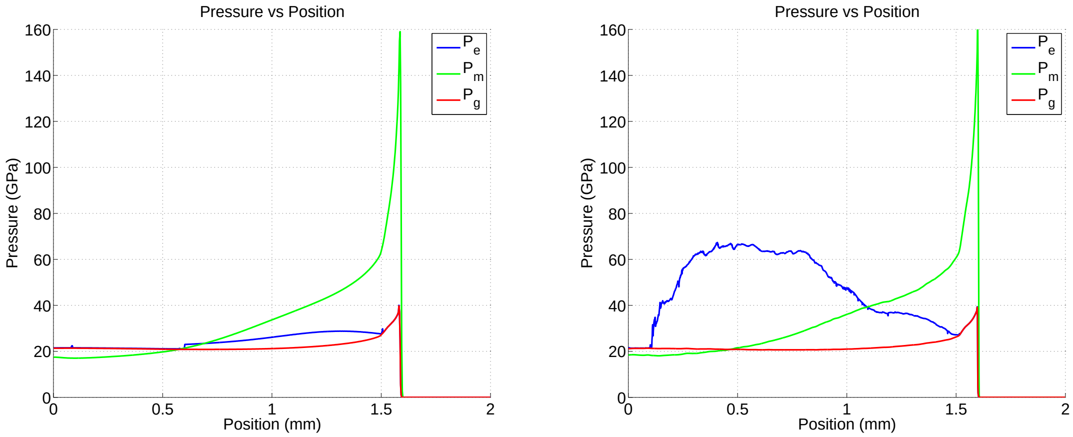

(a) PBX9501 10% 9μm u_p1.5 800cells

(b) PBX9501 10% 9μm u_p1.5 2000cells

Figure 19. PBX9501 10% 9μm P vs X Piston Speed = 1.5 km/s

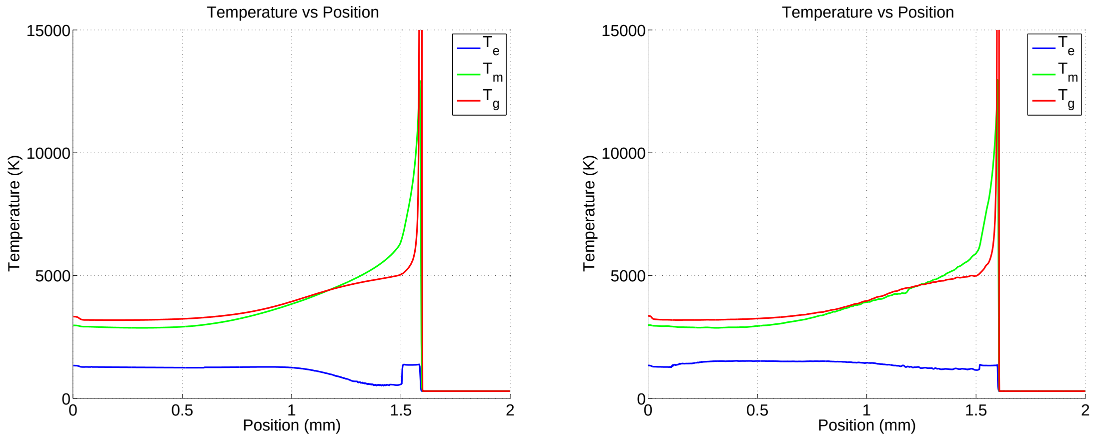

(a) PBX9501 10% 9μm u_p1.5 800cells

(b) PBX9501 10% 9μm u_p1.5 2000cells

Figure 20. PBX9501 10% 9μm T vs X Piston Speed = 1.5 km/s

A summary of the simulations performed to study the precision of higher computational cells and the amount of storage needed per simulation are listed below in Table 6 and Table 7. To describe each simulation in a shorter format, the following naming convention is utilized, "**PBX9501_10_9**". The first part is the name of the explosive, the first number after the explosive name is the mass fraction of the aluminum in percent, and the last number is the diameter of the aluminum in microns. Other added descriptions are added to the name. The added description of "up1.5" is the piston speed and "800cells" is the number of computational cells utilized.

Table 6 shows the percent difference between each simulation at 800 and 2000 computational cells. For the first simulation listed, **PBX9501_10_9_up1.5**, there is a 1.5% average difference between 800 and 2000 cells for particle velocities, 23.4% difference for temperature, 2.1% for pressure, 0.6% for density, and 0.5% for detonation velocity. The other two cases are listed in the table. The largest difference is the temperature but as described in the previous paragraph, the computational model does not accurately predict the actual temperatures near the shock wave. With this in mind, the focus will be on the other detonation properties. The other properties for **PBX9501_10_9_up1.5**, have percent differences below 2.1%. Besides the percent difference for temperature, **PBX9501_20_9_up1.5** has a large percent difference in detonation velocity. The reason for the large percent difference compared to the other cases is because the **PBX9501_10_9_up1.5** 800 cell simulation ended earlier than the 2000 cell simulation. The next paragraph will look at how these differences compare to the amount of storage needed per simulation.

Table 6. Difference Between 800 and 2000 Computational Cells

	Part. Vel. % Diff.	**Temp. % Diff.**	**Press. % Diff.**	**Density % Diff.**	**Det. Vel. % Diff.**
PBX9501_10_9_up1.5	1.5%	23.4%	2.1%	0.6%	0.5%
PBX9501_10_34_up1.5	1.4%	8.6%	1.9%	0.5%	0.5%
PBX9501_20_9_up1.5	2.3%	16.0%	1.7%	0.4%	5.1%

Table 7 below shows a comparison between the amount of storage needed for the data of the simulation for 800 and 2000 computational cells. The first case **PBX9501_10_9_up1.5** at 800 cells outputted 2.9 *gibibytes* and 2000 cells outputted 23.7 *gibibytes*. The 2000 cell simulation requires 8.2 times more data storage capacity than the 800 cell simulation. The 2000 cell simulation for **PBX9501_10_34_up1.5** requires 6.5 times more data storage than 800 cells. The 2000 cell simulation for **PBX9501_20_9_up1.5** requires 7.7 times more data storage than 800 cells.

Table 7. Difference Between 800 and 2000 Computational Cells

	Data Output(GiB)	**2000 vs 800 (Times Larger)**
PBX9501_10_9_up1.5_800cells	2.9	
PBX9501_10_9_up1.5_2000cells	23.7	8.2x
PBX9501_10_34_up1.5_800cells	2.6	
PBX9501_10_34_up1.5_2000cells	17.0	6.5x
PBX9501_20_9_up1.5_800cells	1.5	
PBX9501_20_9_up1.5_2000cells	11.5	7.7x

The average percent difference for all the detonation properties, except temperature, is 1.5%. The average data output for 2000 cell simulations is 7.5 times larger than for the 800 cell simulations. 7.5 times more data storage is not worth the 2% difference in the detonation properties for 2000 computational cells. The rest of the simulations will use 800 computational cells as a starting grid resolution for each metalized case. If the grid resolution does not provide good results for the metalized case, then 2000 computational cells will be utilized. In order to reduce the storage amount the data saving rate can be changed. The data saving rate is defaulted to save a fort file every 10 time steps. For 2000 cells the rate will be changed to save a fort file every 100 time steps. The fewer time step files saved will provide less data points and might result in poor results. This issue will be considered when all the metalized explosive simulation data at 800 computational cells is studied in Chapter IV.

3.6.2 PBX9501/Al at 3 Different Piston Speeds

Several metalized explosive simulations were performed at three different piston speeds to test the limitations of the MPEXS code. The piston speed that were considered were u_p = 0.5, 1.0, and 1.5 km/s. To test the code three cases were considered; **PBX9501_10_9**, **PBX9501_10_13**, and **PBX9501_20_9**. This covered simulations at the lowest concentration of aluminum, which is 10% *Al* mass fraction, at two different *Al* particle diameters. It also covered simulations at the highest concentration of aluminum, 20% *Al* mass fraction.

The piston speed of $u_p = 2.0$ km/s was tested for the three cases. The simulation ran with no issues for **PBX9501_10_9** and **PBX9501_10_13** but failed immediately after starting for **PBX9501_20_9**. The MPEXS code has problems performing calculations with high aluminum mass fractions and high piston speeds. A reasons might be that at high impact speeds the explosive mixture might have compressibility issues. This high metal mass fraction, high impact speed problem has been reported to AFRL, so it can be resolved in further iterations of the code.

Since **PBX9501_20_9** failed at a piston speed of $u_p = 2.0\ km/s$, the three cases were run at a lower piston speed of $u_p = 1.0\ km/s$. The MPEXS code ran with no issues for three cases. The problem with this lower piston speed is that the detonation wave did not reach steady state for the chosen position domain.

Since $u_p = 2.0\ km/s$ was too fast and $u_p = 1.0\ km/s$ was too slow, a piston speed of $u_p = 1.5\ km/s$ was tested for the three cases. The three cases, **PBX9501_10_9**, **PBX9501_10_13**, and **PBX9501_20_9**, ran with no issues and the detonation wave reached steady state for the chosen domain. The piston speed of $u_p = 1.5\ km/s$ provided good results and will be utilized for all the simulations what will be discussed in the results chapter.

3.7 Design of Experiments

Design of Experiments (DOE) is the process of determining the cause-and-effect relationships between input parameters and how these relationships affect the output. The purpose for such analysis is to optimize the output by looking at the inputs. A stochastic experiment has inputs that are uncontrollable and are usually not solved analytically. DOE methods are useful for stochastic experiments to determine the effect that these uncontrollable inputs have on the output. In deterministic experiments the inputs are controllable and the relationship between input and output is conclusively determined. The input parameters for this research are particle size and mass fraction and both are controllable and are independent of each other. The six different aluminum particle sizes are discrete because these sizes are determined by the manufacturer. The aluminum mass fraction is determined by the user. These input parameters are controllable and independent of each other, therefore this research is considered deterministic. DOE methods were considered for the multiphase code simulation runs but there was no benefit in using a DOE method.

3.8 Summary

Section 3.2 explained the different modeling methods that lead to multiphase computational modeling. After the modeling method for multiphase explosives was described, a brief summary was given of the main files utilized in the MPEXS code in Section 3.3. The MPEXS code will be utilized to perform all the simulations of metalized PBX9501 explosive. Section 3.4 describes the different simulations runs that will be performed at different *Al* mass fractions and *Al* particle diameters. Section 3.5 and Section 3.6 explained the different preliminary studies that were performed to find the limitations of the code and selected the initial parameters for all the simulation cases.

IV. Data Discussion

4.1 Introduction

This chapter will present the results from the three main studies that were performed. The purpose of these studies was to evaluate the stability and limitations of the MPEXS code. The first study is a short study with neat PBX9501 to compare run-to-detonation properties against a single phase explosive code developed by AFRL. This study will verify that the MPEXS code outputs reasonable data. The second study is a convergence test of detonation properties by varying the number of computational cells for metalized PBX9501. The goal of this study was to test the stability of the code by looking for a convergence in the data as the number of computational cells increased, decreasing the grid size. The third study is to study the effects of aluminum on PBX9501 by performing several simulations at a range of aluminum mass fractions and aluminum particle diameters. The results of the three studies are presented in the three sections below.

4.2 Run-to-Detonation Properties for Neat PBX9501

The MPEXS code was developed to run simulations for multiphase explosives that contain at least two solid components like an explosive and a metal. For this research, the chosen explosive is PBX9501 and the chosen non-reactive metal is aluminum. The MPEXS code also has the capability to run single phase explosive simulations. Before multiphase simulations are considered, the MPEXS code must first be tested with single phase explosive simulations.

The MPEXS code was utilized to perform a short Run2Det study of neat PBX9501 at several piston speeds $u_p = 0.5$, $u_p = 1.0$, and $u_p = 1.5$ km/s. The description "Run-to-detonation" is abbreviated to "Run2Det" in this report. The MPEXS

Run2Det results will be compared to the results of the Single-Phase Explosive Simulation (SPEXS) code. The SPEXS code was developed and utilized by AFRL's High Explosives Research and Development (HERD) group to determine Run2Det properties for single phase explosives. The goal of this study is to compare the MPEXS results to SPEXS results. The equations of state utilized for the MPEXS code are different from the SPEXS code, therefore the Run2Det properties should be different. Although the results will differ, the MPEXS data should display a similar trend as the SPEXS data. A qualitative comparison will verify the MPEXS code is working properly.

Two important parameters in explosive studies are run-to-detonation time and run-to-detonation distance. The Run2Det time and distance is the time and location the explosive detonation transitions to steady state. Detonation properties in the transition stage provide information with little use because these properties are constantly changing and unstable. The Run2Det time versus distance diagrams provide an illustration of the transition from the initial shock wave to the detonation shock wave. These time versus distance diagrams, often call "pop-plots", provide the Run2Det time and distance as a function of shock input pressure. The threshold input pressure is set by the user in the **postprocess.f90** file described in Section 3.3.1.4. Pop-plots are utilized to determine the transition time and location to a steady state detonation.

There are two slopes connected by a smooth transition in the pop-plot. The slope closest to the zero position represents the initial shock wave. During the initial shock wave the detonation is still in development. The second slope represents the steady state detonation shock wave. The transition from one slope to the other is very gradual and difficult to detect. The goal is to determine the time and position when the detonation reaches steady state. The time and position can be approximated by finding a point where the second slope begins, showing a constant rate of change. Figure 21 to Figure 23 show the pop-plots for the three piston speeds tested in this study. The pop-plots have a pressure gradient bar on the right side of the plot. The pressure is the current pressure at the time and position within the chart. If the color gradient that represents the current pressure is followed along the slope of the first slope, it is seen that pressure increases as the initial shock wave develops. Along the transition to the steady state slope line the pressure increases rapidly, then at some point the pressure stabilizes to a constant pressure. The point where the pressure values begin to stabilize is the point that is chosen to be the Run2Det time and position. The point at the beginning of the second slope can be seen on Figure 21 to Figure 23. The chosen pressure for this neat PBX9501 study is 3.0e10 Pa (30 GPa).

Three pop-plots were generated for the three simulation runs at piston speeds of $u_p = 0.5$, $u_p = 1.0$, and $u_p = 1.5$ km/s. Figure 21 is the pop-plot for Neat PBX9501 at $u_p = 0.5$ km/s and shows a Run2Det time of 2.1705 μs and distance of 5.001 millimeters. Figure 22 is the pop-plot for Neat PBX9501 at $u_p = 1.0$ km/s and shows a Run2Det time of 0.41043 μs and distance of 1.4125 millimeters. Figure 23 is the pop-plot for Neat PBX9501 at $u_p = 1.5$ km/s and shows a Run2Det time of 0.15460 μs and distance of 0.60063 millimeters.

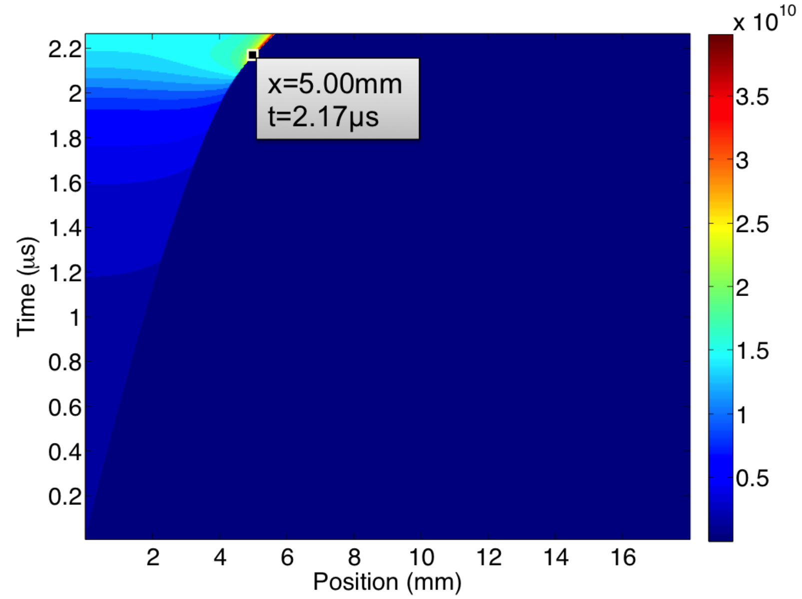

Figure 21. Neat PBX9501 Pop-Plot (u_p = 0.5 L = 18 Nx = 3000)

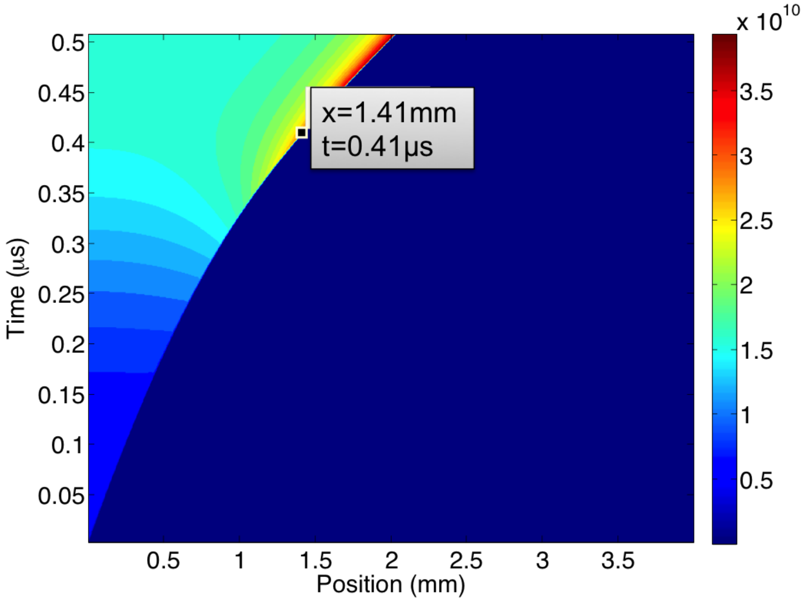

Figure 22. Neat PBX9501 Pop-Plot (u_p = 1.0 L = 4 Nx = 800)

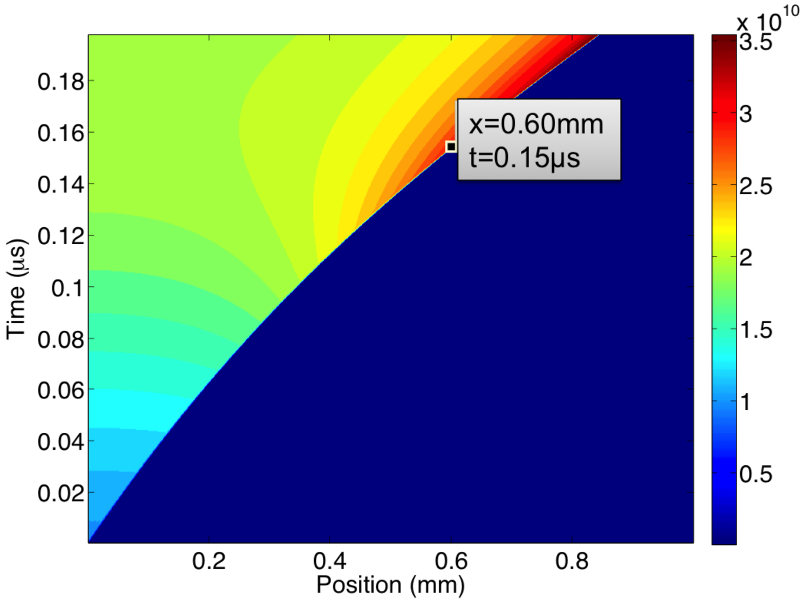

Figure 23. Neat PBX9501 Pop-Plot (u_p = 1.5 L = 1 Nx = 800)

Table 8 is a summary of all the SPEXS and MPEXS simulation results for the three piston speeds. As seen on Table 8, Run#1 failed for the simulations run with the MPEXS code. The reason for the code failure was that the grid size was too large. The grid size is calculated by taking the total length divided by the number of computational cells utilized. The length for Run#1 was 18 mm and the number of cells utilized was 800 cells resulting in a grid size of 0.022 $mm/cell$. The grid size was increased by using 3000 cells over the same length for Run#2, resulting in a grid size of 0.006 $mm/cell$. The results for both codes are as follows.

Table 8. Neat PBX9501 Run-to-Detonation Properties

Run #	u_p (km/s)	**Grid Size** $(mm/cell)$	**SPEXS Run2Det x** (mm)	**MPEXS Run2Det x** (mm)	**SPEXS Run2Det Time** (μs)	**MPEXS Run2Det Time** (μs)
1	0.5	0.022	15.00	Failed	4.50	Failed
2	0.5	0.006	15.00	5.00	4.50	2.17
3	1.0	0.005	2.00	1.41	0.45	0.41
4	1.5	0.001	0.30	0.60	0.10	0.15

Figure 24 is a bar chart to compare the Run2Det distance for both the SPEXS and MPEXS codes. The Run2Det distance for each piston speed are shown in blue for SPEXS and red for MPEXS. As the piston speed increases the Run2Det distance decreases. The average rate of change between $u_p = 0.5$ and $u_p = 1.0$ is 26 $mm/(km/s)$ for SPEXS and 7.18 $mm/(km/s)$ for MPEXS. The average rate of change between $u_p = 1.0$ and $u_p = 1.5$ is 3.40 $mm/(km/s)$ for SPEXS and 1.62 $mm/(km/s)$ for MPEXS. The reason for the difference in results between both codes is due to the use of different equations of state for the reaction. The average rate of change between each set of points is larger for the SPEXS code but the takeaway is that the MPEXS code follows the same trend.

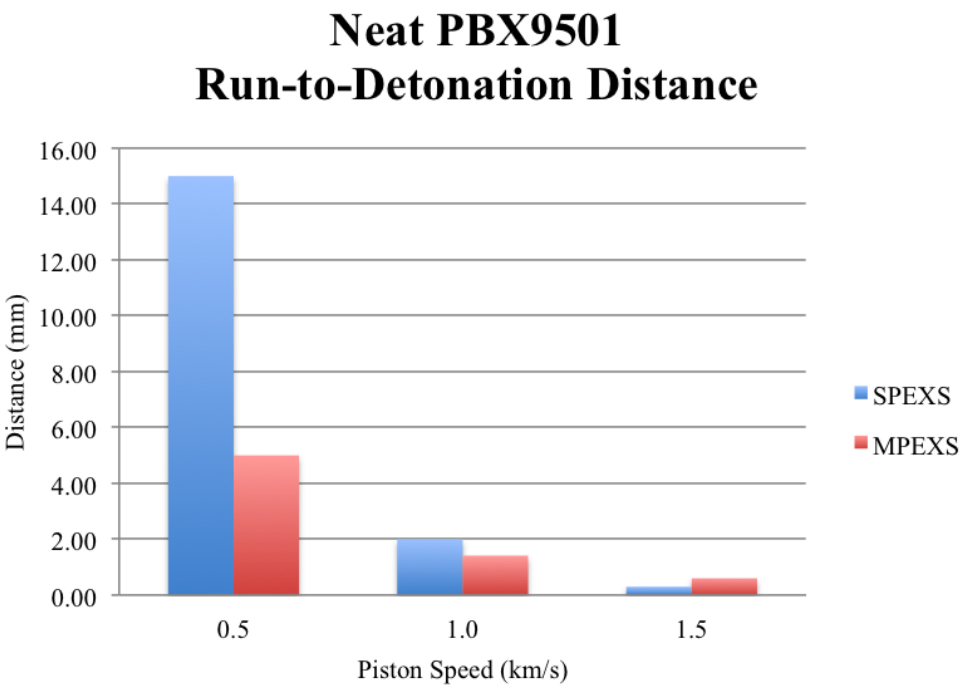

Figure 24. NeatPBX9501 R2D Distance Chart

Figure 25 shows the Run2Det time at different piston speeds for both the SPEXS and MPEXS codes. As the piston speed increases the Run2Det time decreases. The average rate of change between $u_p = 0.5$ and $u_p = 1.0$ is 8.10 $\mu s/(km/s)$ for SPEXS and 3.52 $\mu s/(km/s)$ for MPEXS. The average rate of change between $u_p = 1.0$ and $u_p = 1.5$ is 0.70 $\mu s/(km/s)$ for SPEXS and 0.52 $\mu s/(km/s)$ for MPEXS. The average rate of change between each set of points is larger for the SPEXS code. Again the difference in the results between both codes is that different equations of state were utilized.

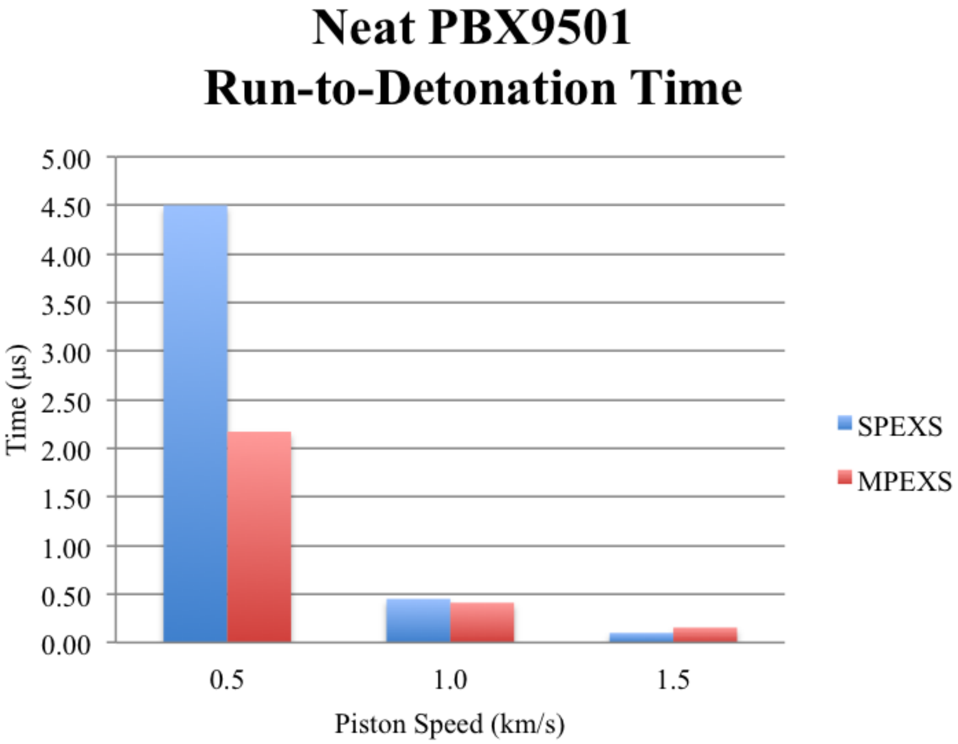

Figure 25. NeatPBX9501 R2D Time Chart

4.3 PBX9501/AL Convergence Test

Another study that was performed was a convergence test of detonation properties for different computational cell sizes. The computational cell sizes play an important role in the grid resolution of the simulation. The number of computational cells, Nx, per unit length is the grid size. The MPEXS code was designed to perform simulations at the macroscopic scale. If the grid size is large the code will stop because the equations can not handle macro scale calculations. If the grid size is very small then the code will run into problems were the grid size is smaller than the particle diameters. The convergence test was performed with **PBX9501_10_9** at a piston speed of 1.0 km/s. The computational cell sizes were varied from 200 to 3000 cells. There are three detonation properties that were considered for this convergence test, Run2Det time, Run2Det distance, and detonation velocity. The Run2Det distance and time are approximated by analyzing the pop-plot chart and finding the point were the detonation transitions to steady-state as described earlier. The point was chosen at the beginning of the steady-state slope at a pressure value of 35 GPa for all metalized explosive cases.

Table 9 summarizes the results for the convergence test for the computational cell range. Run 1 and 2 failed due to the grid size being too large. Based on this study and the neat explosive study from Section 4.2 it was concluded that for any grid size larger than 9.9e-3 $mm/cell$ will make the code fail. The MPEXS code ran for simulations with 800 or more computational cells. The Run2Det distance and time, and detonation velocity results are listed below, in Table 9.

The final stop time for all the runs in this study was set at tfinal = 2.0 μs in the **maininput.txt** file. It was observed that all the simulations did not run to the final run time. The runs stopped around 1.2 μs and runs 10 and 11 stopped around 1.4 μs. An explanation for the early stop time is that the errors occurring in the code are due to larger numerical error for lower resolutions simulations. As the resolution increases, the simulations run longer due to a decrease in numerical error. The early stop time issue will be reported to the HERD to be corrected in future code versions.

Table 9. PBX9501_10_9 Convergence Test

Run #	**Nx**	**Grid Size** ($mm/cell$)	**Run2Det x** (mm)	**Run2Det Time** (μs)	**Det. Vel.** (km/s)
1	200	0.0300	Failed	Failed	Failed
2	400	0.0150	Failed	Failed	Failed
3	800	0.0075	3.761	1.193	6.142
4	1000	0.0060	3.699	1.182	6.576
5	1300	0.0046	3.722	1.182	7.013
6	1600	0.0037	3.733	1.183	7.251
7	1800	0.0033	3.738	1.184	7.387
8	2000	0.0030	3.743	1.184	7.667
9	2500	0.0024	3.757	1.186	7.957
10	3000	0.0020	3.739	1.183	7.940

The results for the Run2Det distance are plotted on Figure 26. For smaller computational cells the Run2Det distance varies but as the cell number increases the Run2Det distance seems to stabilize at a distance around 3.74 mm.

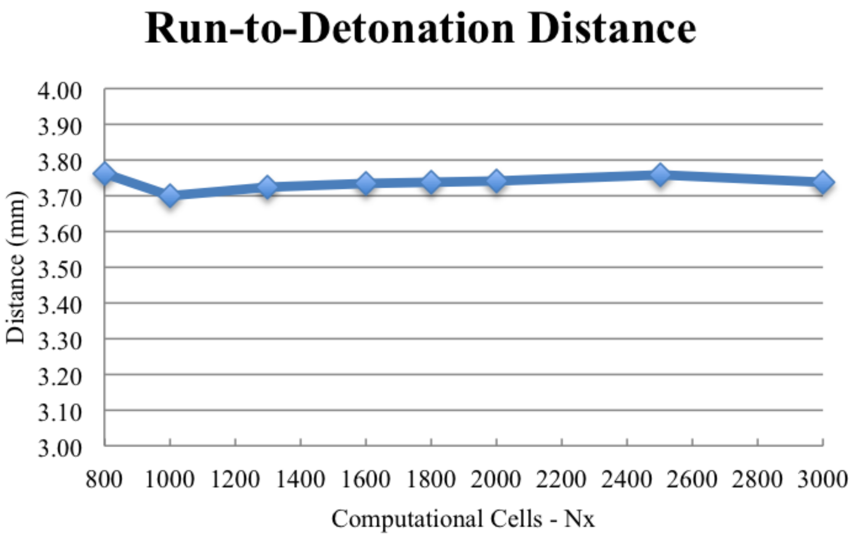

Figure 26. Convergence Test for PBX9501_10_9 Run2Det Distance

Figure 27 is a plot of Run2Det time in microseconds versus computational cells. The Run2Det time has the same relationship to Nx as Run2Det distance. At smaller cell amounts the results are unstable but as the number of cells increases the Run2Det time stabilizes around 1.183 μs.

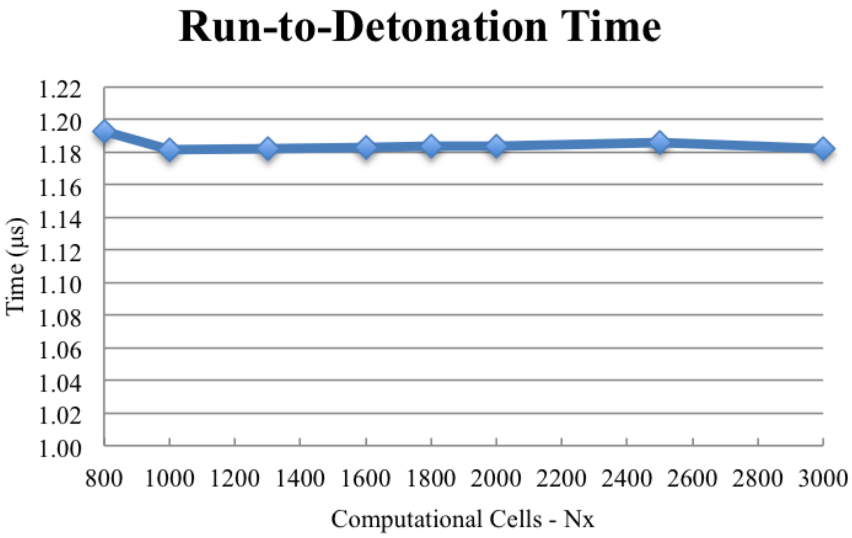

Figure 27. Convergence Test for PBX9501_10_9 Run2Det Time

Figure 28 plots the detonation velocity in kilometers per second versus computational cells. As the resolution increases the detonation velocity results stabilize around 7.94 km/s. The results for Run2Det distance, Run2Det time, and detonation velocity behave as expected where the results should converge to a steady value as the resolution is increased.

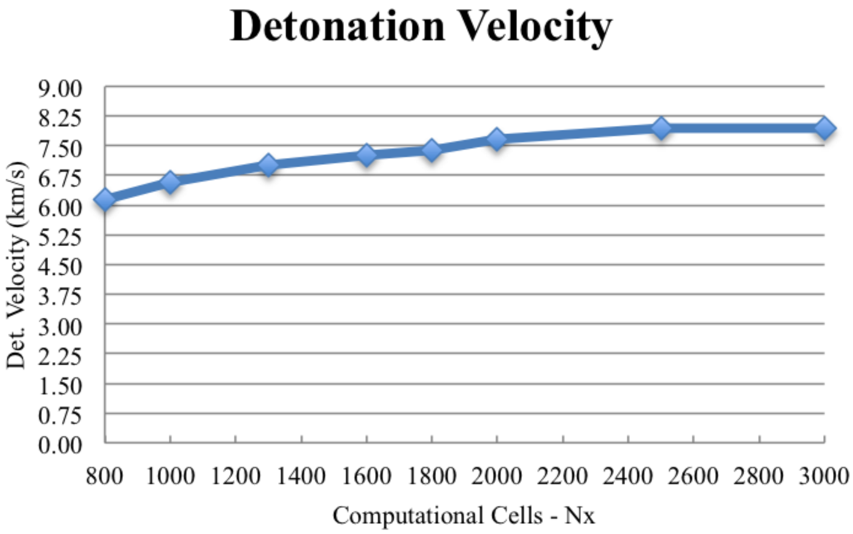

Figure 28. Convergence Test for PBX9501_10_9 Detonation Velocity

Figure 29 through Figure 31 are the pop-plots for three different computational cells, 800, 1600, and 3000 cells, for **PBX9501_10_9**. The domain length for each simulation is from the left boundary location (0 mm) to the right boundary location (6 mm). All the pop-plots are very similar since Run2Det distance has a standard deviation of 0.019 mm, a standard deviation of 0.003 μs for Run2Det time, and a standard deviation of 0.644 km/s for detonation velocity. Figure 31 looks different than the other simulations due to the longer running time when 3000 computational cells were utilized, but the Run2Det point is almost the same for the three plots. Although the simulations stopped earlier than the final simulation time, the data collected was enough to determine steady state detonation properties like Run2Det distance, Run2Det time, and detonation velocities.

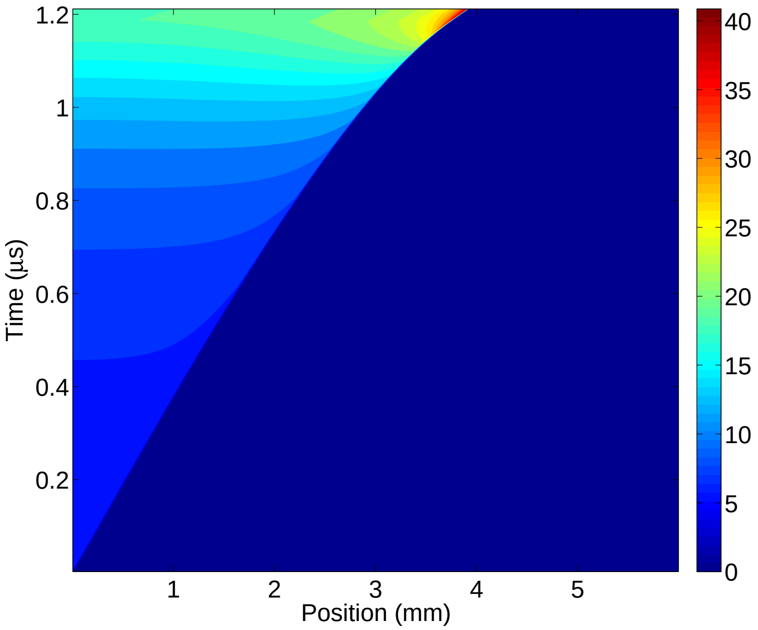

Figure 29. PBX9501_10_9 Pop-Plot (Nx=800 cells)

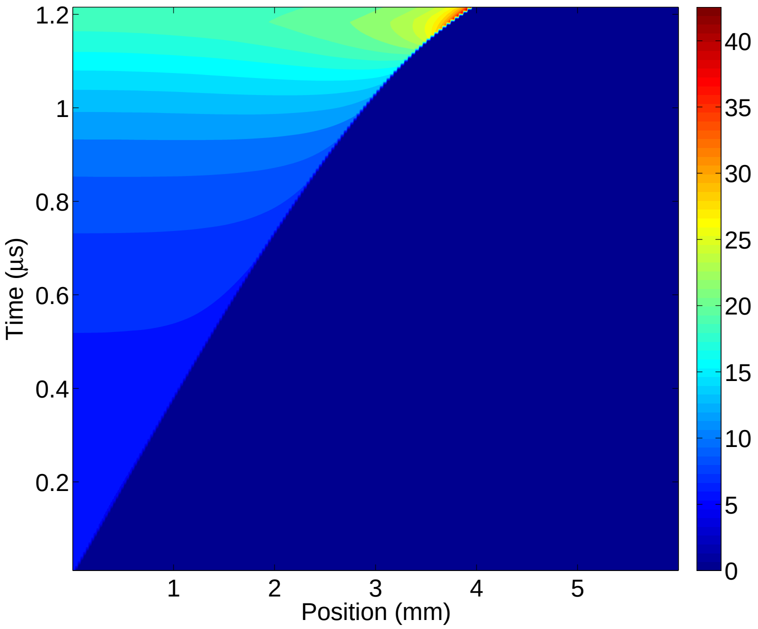

Figure 30. PBX9501_10_9 Pop-Plot (Nx=1600 cells)

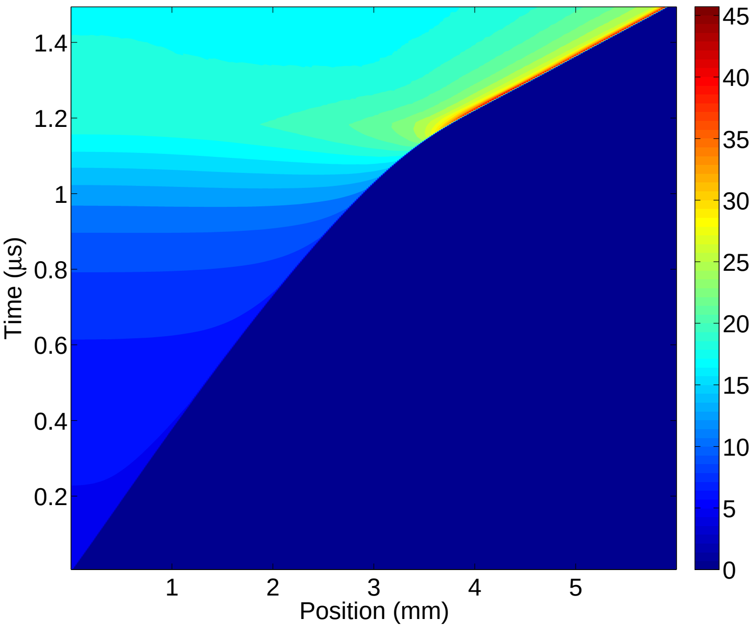

Figure 31. PBX9501_10_9 Pop-Plot (Nx=3000 cells)

The convergence test was performed to determine the stability of grid convergence and the limits of the MPEXS code. The grid convergence of the code was proved by the converging results as the number of computational cells increased. The number of computational cells is related to the resolution or the grid size of the simulation. The finer the resolution the more precise the results and should converge as seen in this study. The limits of the MPEXS were also determined during this study. The MPEXS code did not run with computational sizes such as Nx = 200 and Nx = 400. For Nx = 800 and Nx = 1000 the results were unpredictable.

4.4 All Cases of PBX9501/Al to Steady State Detonation

The third study was performed with all the cases of PBX9501/Al, which covered a wide range of aluminum particle diameter and aluminum mass fraction. The six aluminum diameters were tested for each of the three aluminum mass fractions, resulting in 18 simulation runs. For example, the aluminum mass fraction of 10 percent was tested with 9, 13, 19, 23, 29, and 34 micron diameter. The same six diameters were utilized for 15 and 20 percent aluminum mass fraction. The 18 runs were performed for two computational cell, 800 and 2000, for a total of 36 simulation runs. These two computational cell sizes of Nx = 800 and Nx = 2000 were chosen to compare the data for both a low and high grid size. A piston speed of $u_p = 1.5\ km/s$ was selected for all the PBX9501/Al cases. The main parameters considered were Run2Det distance, Run2Det time, detonation velocity, pressure, temperature, particle velocity, and volume fraction.

This study will evaluate the stability and limits of the MPEXS code. The results will be analyzed and qualitative conclusions will be made about the effects of Al on PBX9501. As discussed in earlier chapters, comparing simulation data to empirical data does not provide any benefit to this research due to the complexity of plastically bonded explosives like PBX9501.

4.4.1 Run-to-Detonation Properties and Detonation Velocity

The 18 runs were performed at 800 computational cells at $u_p = 1.5\ km/s$. The results for Run2Det distance and time, and detonation velocity are presented on Table 10. As the Al mass fraction increases from 10 to 15 to 20 percent, the Run2Det distance decreases. As the Al diameter increases from 9 to 34 μm, the Run2Det distance slightly decreases. The effects of varying the mass fraction are larger than the effects of varying the diameter of the Al for Run2Det distance. As the mass fraction is increased from 10 to 15 to 20 percent, the Run2Det time decreases significantly. As the Al diameter is increased from 9 to 34 μm for each mass fraction, the Run2Det time varies but on average it remains constant. The results for detonation velocity are unpredictable for the 15 and 20 percent cases.

The same 18 runs were performed again for 2000 computational cells at the same piston speed $u_p = 1.5\ km/s$. The results for Run2Det distance and time, and detonation velocity are presented on Table 11. The results for 2000 computational cells are similar from the 800 computational cells cases discussed in the previous paragraph but the results are more stable for detonation velocity. As the Al mass fraction increases from 10 to 15 to 20 percent, the Run2Det distance decreases. As the Al diameter increases from 9 to 34 μm, the Run2Det distance slightly decreases. The effects of varying the mass fraction are larger than the effects of varying the diameter of the Al for Run2Det distance. As the mass fraction is increased from 10 to 15 to 20 percent, the Run2Det time decreases significantly. As the Al diameter is increased from 9 to 34 μm for each mass fraction, the Run2Det time varies but on average it remains constant. As the Al mass fraction increases from 10 to 15 to 20 percent, the detonation velocity decreases. Also, as the Al particle diameter increases from 9 to 34 μm for each mass fraction, the data shows the detonation velocity decreases.

Table 10. PBX9501/Al Detonation Properties at u_p = 1.5 km/s Nx = 800cells

Run #	**Name**	**Run2Det x (mm)**	**Run2Det Time (μs)**	**Det. Vel. (km/s)**
1	PBX9501_10_9	1.016	0.258	8.024
2	PBX9501_10_13	1.021	0.259	7.997
3	PBX9501_10_19	1.026	0.260	7.978
4	PBX9501_10_23	1.026	0.261	7.967
5	PBX9501_10_29	1.021	0.260	7.954
6	PBX9501_10_34	1.011	0.258	7.953
7	PBX9501_15_9	0.939	0.233	7.749
8	PBX9501_15_13	0.941	0.234	7.745
9	PBX9501_15_19	0.939	0.234	7.621
10	PBX9501_15_23	0.939	0.235	7.778
11	PBX9501_15_29	0.929	0.234	7.807
12	PBX9501_15_34	0.921	0.233	7.770
13	PBX9501_20_9	0.866	0.210	7.378
14	PBX9501_20_13	0.864	0.211	7.455
15	PBX9501_20_19	0.869	0.211	7.490
16	PBX9501_20_23	0.861	0.212	7.478
17	PBX9501_20_29	0.851	0.211	7.460
18	PBX9501_20_34	0.854	0.211	7.561

Table 11. PBX9501/Al Detonation Properties at u_p = 1.5 km/s Nx = 2000cells

Run #	**Name**	**Run2Det x** (mm)	**Run2Det Time** (μs)	**Det. Vel.** (km/s)
1	PBX9501_10_9	1.014	0.255	8.060
2	PBX9501_10_13	1.020	0.257	8.026
3	PBX9501_10_19	1.013	0.257	8.014
4	PBX9501_10_23	1.012	0.257	8.005
5	PBX9501_10_29	1.011	0.257	7.996
6	PBX9501_10_34	1.017	0.258	7.997
7	PBX9501_15_9	0.944	0.232	7.897
8	PBX9501_15_13	0.943	0.233	7.866
9	PBX9501_15_19	0.939	0.233	7.858
10	PBX9501_15_23	0.938	0.233	7.852
11	PBX9501_15_29	0.932	0.233	7.844
12	PBX9501_15_34	0.926	0.232	7.848
13	PBX9501_20_9	0.888	0.214	7.813
14	PBX9501_20_13	0.887	0.215	7.815
15	PBX9501_20_19	0.871	0.212	7.783
16	PBX9501_20_23	0.873	0.213	7.765
17	PBX9501_20_29	0.859	0.211	7.739
18	PBX9501_20_34	0.850	0.209	7.744

Figure 32 and Figure 33 shows the pop-plots for PBX9501 at 10% aluminum mass fraction for 9 mm and 34 mm aluminum diameters. The smallest and largest of *Al* particle diameter were chosen for each *Al* mass fraction. The pop-plots for the *Al* particle diameters 13, 19, 23, 29 are very similar to each other at each *Al* mass fraction. For brevity of the report all the pop-plots were not included but the results are presented on Table 10 and Table 11. The pop-plots have a pressure gradient bar on the right side of the plot whose units are in gigapascals. The Run2Det properties for **PBX9501_10_9_up1.5_2000cells** are Run2Det time = 0.255 μs and Run2Det distance = 1.014 mm. The Run2Det properties for **PBX9501_10_34_up1.5_2000cells** are Run2Det time = 0.258 μs and Run2Det distance = 1.017 mm.

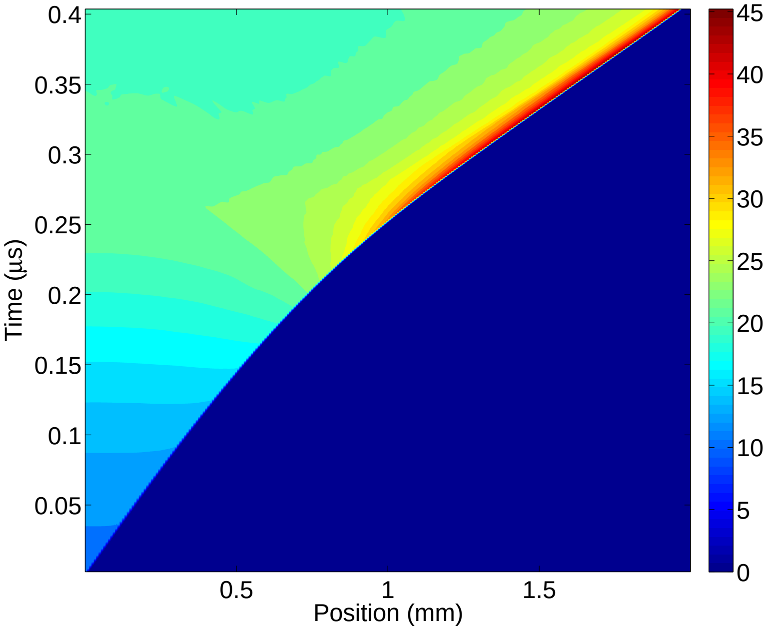

Figure 32. PBX9501_10_9 Pop-Plot (Nx=2000 cells)

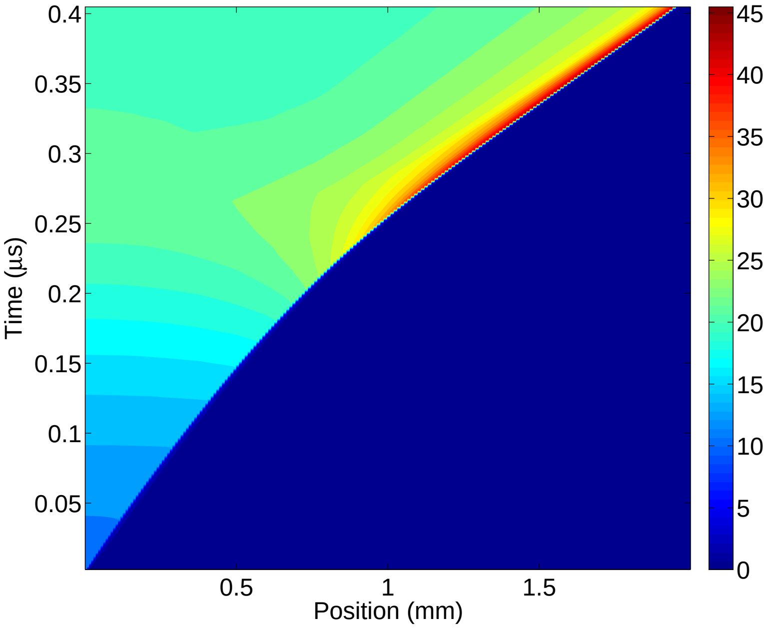

Figure 33. PBX9501_10_34 Pop-Plot (Nx=2000 cells)

Figure 34 and Figure 35 show the pop-plots for PBX9501 at 15% aluminum mass fraction for 9 mm and 34 mm aluminum diameters. The Run2Det properties for **PBX9501_15_9_up1.5_2000cells** are Run2Det time = 0.232 μs and Run2Det distance = 0.944 mm. The Run2Det properties for **PBX9501_15_34_up1.5_2000cells** are Run2Det time = 0.232 μs and Run2Det distance = 0.926 mm.

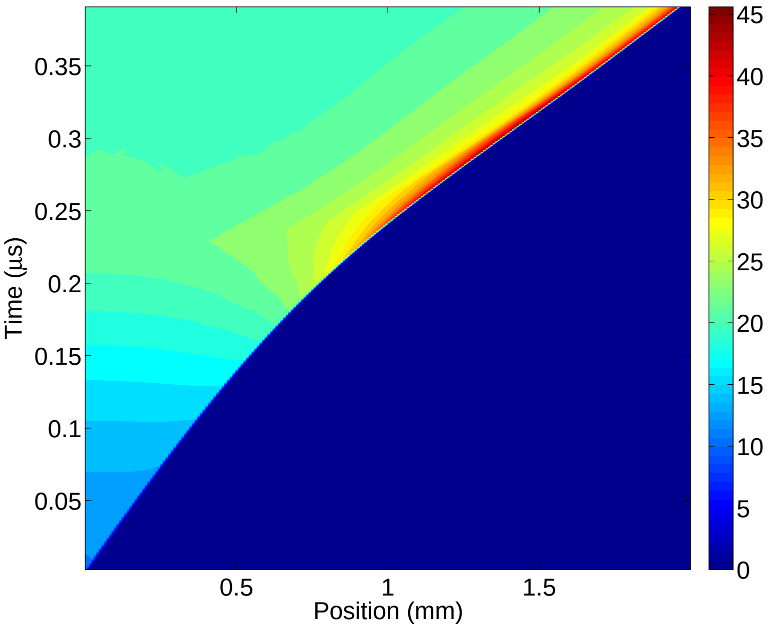

Figure 34. PBX9501_15_9 Pop-Plot (Nx=2000 cells)

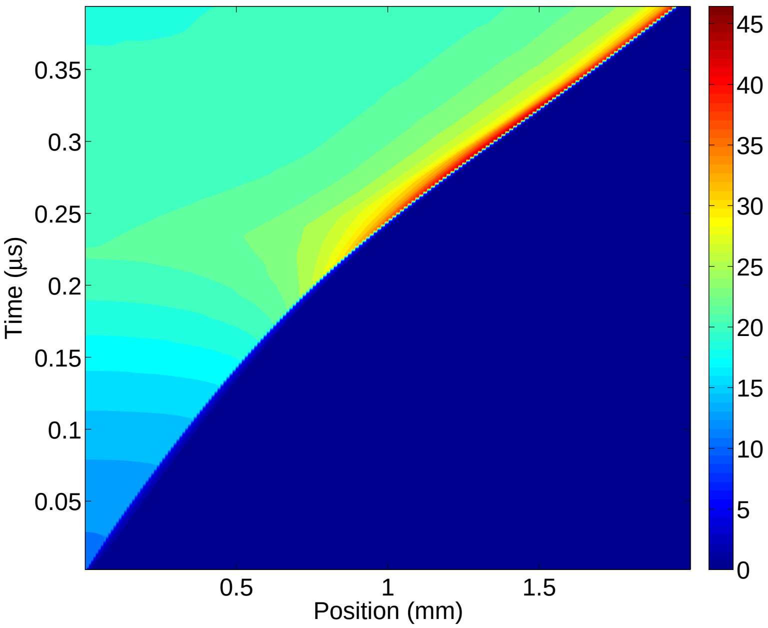

Figure 35. PBX9501_15_34 Pop-Plot (Nx=2000 cells)

Figure 36 and Figure 37 show the pop-plots for PBX9501 at 20% aluminum mass fraction for 9 μm and 34 μm aluminum diameters. Figure 36 seems to have a greater slope than the rest of the pop-plots but it only looks different due to the shorter run time for the **PBX9501_20_9** simulation run. The results for Run2Det distance and time for both cases are within 0.012 mm and 0.001 μs of each other. The Run2Det properties for **PBX9501_20_9_up1.5_2000cells** are Run2Det time = 0.214 μs and Run2Det distance = 0.888 mm. The Run2Det properties for **PBX9501_20_34_up1.5_2000cells** are Run2Det time = 0.209 μs and Run2Det distance = 0.850 mm.

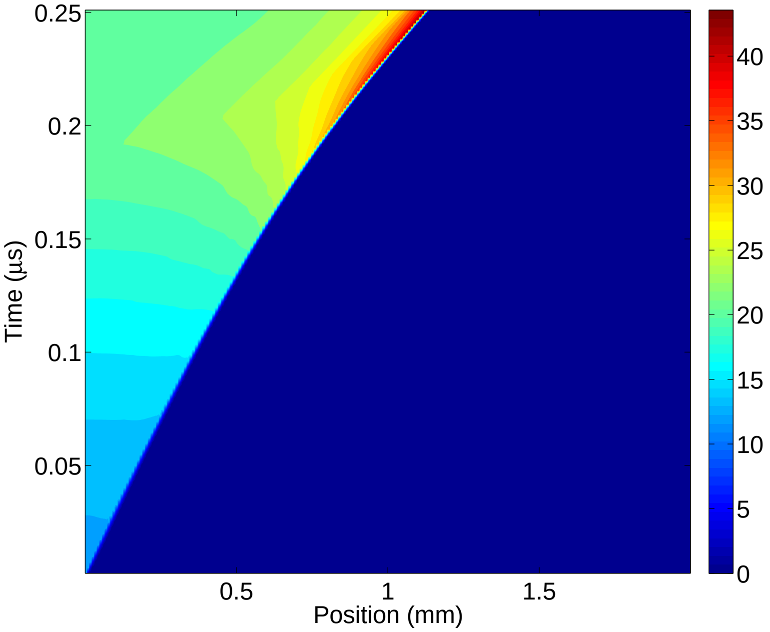

Figure 36. PBX9501_20_9 Pop-Plot (Nx=2000 cells)

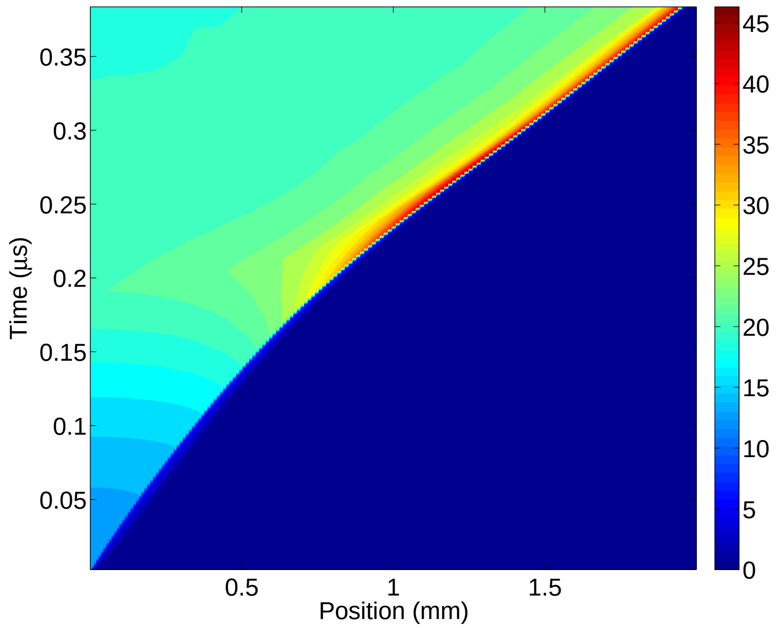

Figure 37. PBX9501_20_34 Pop-Plot (Nx=2000 cells)

Figure 38 shows the Run2Det distance for all the runs at both computational cell amounts, 800 and 2000 cells. Runs 1-6 are for PBX9501 at 10% *Al* mass fraction for the six *Al* particle diameters. The red square data points are for Nx2000 and the blue diamond data points are for Nx800. The other runs for 15 and 20 percent are also plotted and can be identified using the key on the right side of the chart in Figure 38.

The Run2Det distance for 10% PBX9501 at Nx2000, represented by the red squares, goes up and down, and has no noticeable trend. The Run2Det distance for 10% PBX9501 at Nx800, represented by the blue diamonds, has a small convex trend where the distance increases and then decreases as the *Al* particle diameter increases. The Run2Det distance for 15% PBX9501 at Nx2000 and Nx800, represented by the purple X and green triangle respectively, both have a slight decrease in distance as the *Al* particle diameter increases. The Run2Det distance for 20% PBX9501 at Nx2000 and Nx800, represented by the orange circle and teal star respectively, both have steady values then decrease slightly and then steady again. In general a conclusion can be made that as the aluminum mass fraction increases from 10 to 15 to 20 percent, the Run2Det distance decreases. As the aluminum diameter increases from 9 to 34 μm, the Run2Det distance slightly decreases. The effects of varying the mass fraction are larger than the effects of varying the diameter of the aluminum.

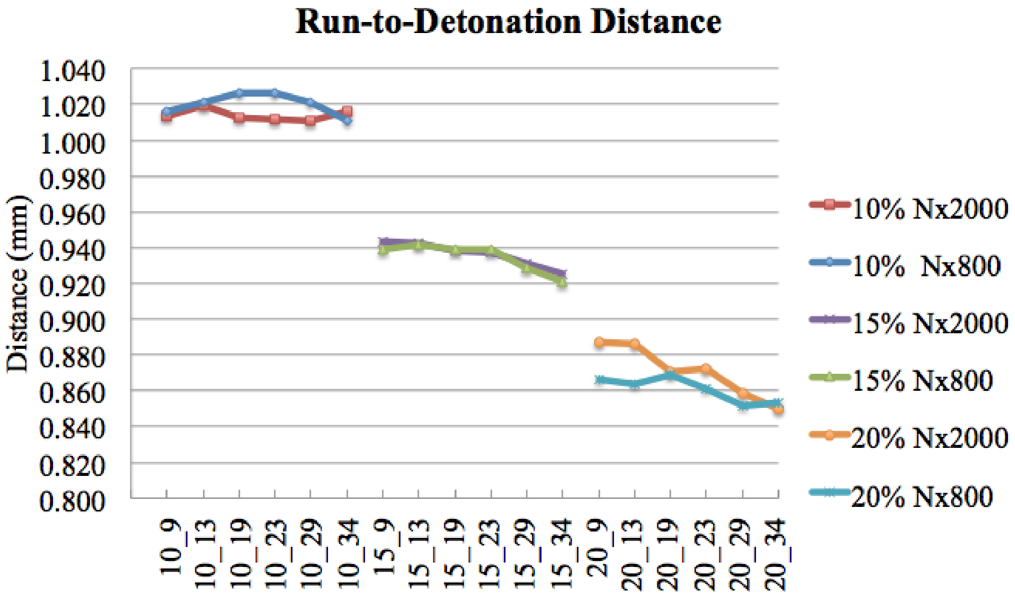

Figure 38. PBX9501 All Cases Run2Det Distance

Figure 39 shows the Run2Det time for all the runs at both computational cell amounts, 800 and 2000 cells. The Run2Det time for 10% PBX9501 at Nx2000, represented by the red squares, increases, decreases, and then increases again not showing any trend in the data. The Run2Det time for 10% PBX9501 at Nx800, represented by the blue diamonds, has a small convex trend as the aluminum size increases. The Run2Det time for 15% PBX9501 at Nx2000 and Nx800, represented by the purple X and green triangle respectively, both have a small convex trend as the *Al* particle diameter increases. The results for both case are almost identical and points are almost on top of each other. The Run2Det time for 20% PBX9501 at Nx2000, represented by the orange circle, has a slight decrease as the *Al* particle diameter increases. The Run2Det time for 20% PBX9501 at Nx800, represented by the teal star, is steady as the *Al* particle diameter increases. The effects of varying the mass fraction are larger than the effects of varying the diameter of the aluminum. When the mass fraction is increased from 10 to 15 to 20 percent, the Run2Det time decreases significantly. When the aluminum diameter is increased from 9 to 34 μm for each mass fraction, the Run2Det time varies but the variation is small.

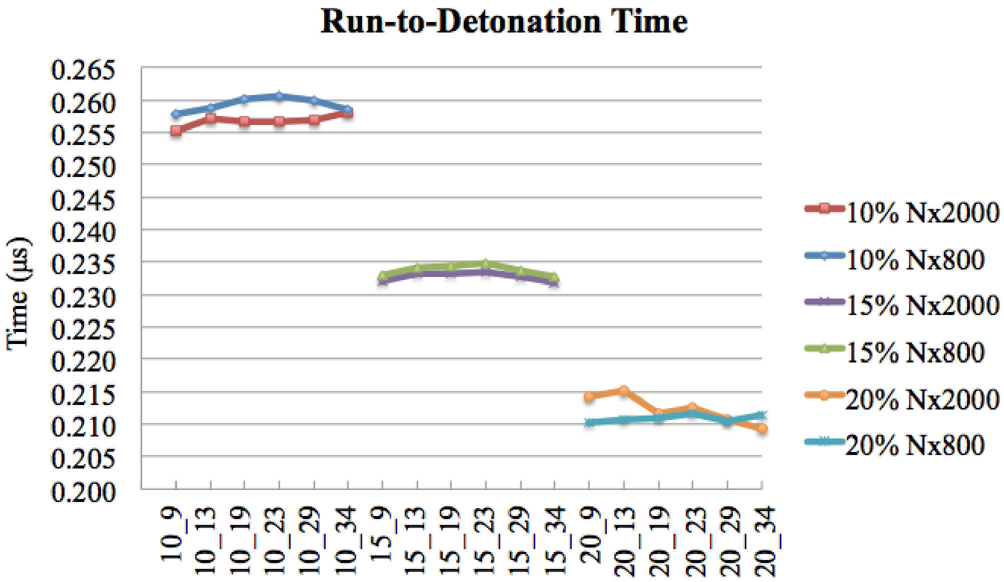

Figure 39. PBX9501 All Cases Run2Det Time

Figure 40 plots the detonation velocity versus the run numbers at the three different aluminum mass fractions. The detonation velocity for 10% PBX9501 at Nx2000 and Nx800, represented by the red squares and blue diamonds respectively, both have a steady decrease as the *Al* particle diameter increases. The detonation velocity for 15% PBX9501 at Nx2000, represented by the purple X, has a steady decrease as the *Al* particle diameter increases. The detonation velocity for 15% PBX9501 at Nx800, represented by the green triangle, has a very unstable pattern with large deviations in the detonation velocity as the *Al* size increases. The detonation velocity for 20% PBX9501 at Nx2000, represented by the orange circle, has a steady decrease as the *Al* particle diameter increases. The detonation velocity for 20% PBX9501 at Nx800, represented by the teal star, has a unstable pattern in the data. For this case, the detonation velocity increases as the particle diameter increases, which is opposite of what is expected. Considering only the more stable results using 2000 cells a few conclusions can be made for detonation velocity. As the *Al* mass fraction increases from 10 to 15 to 20 percent, the detonation velocity decreases. Also, as the *Al* particle diameter increases from 9 to 34 μm for each mass fraction, the data shows the detonation velocity decreases.

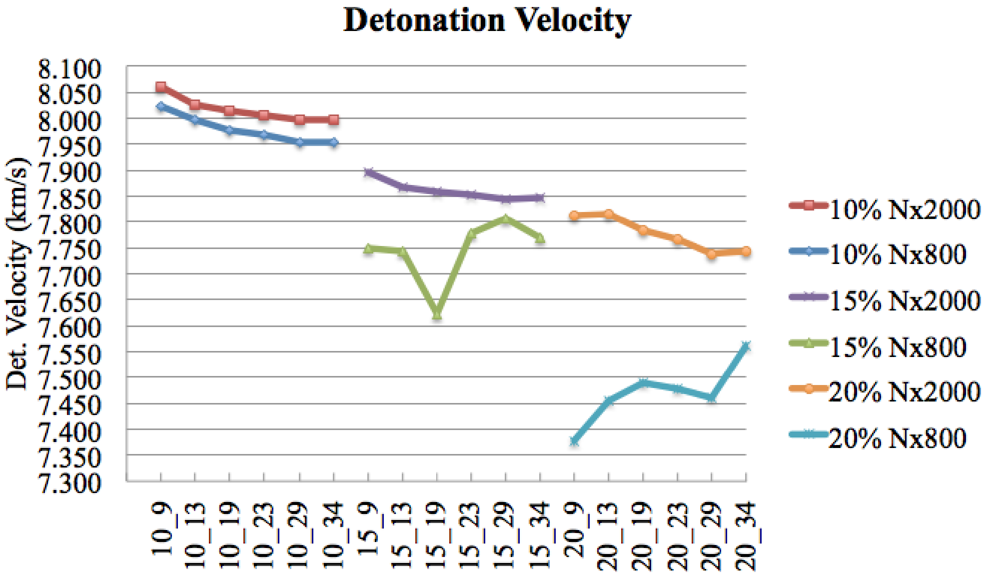

Figure 40. PBX9501AllCases Detonation Velocity

It was concluded that the simulations using 2000 computational cells provide more consistent results for both varying cases, *Al* mass fraction and *Al* particle diameter. The purpose of running simulations with both sizes of computational cells, 800 and 2000 cells, is study the effects of grid size on metalized explosive simulations. In Section 4.3, it was found that at lower resolutions the detonation property results are unstable. The same stability issues at low resolution was also seen for the metalized explosive simulations presented in this section.

4.4.2 Other Detonation Properties

Detonation properties like Run2Det distance and time, and detonation velocity are provide more useful information about explosion but other properties like pressure, particle velocity, volume fraction, and temperature must not be neglected. Pressure of the shock wave provides information about the strength of the shock wave. Particle velocity provides information on the velocity of the shock wave. Volume fraction provides information about the chemical reaction. Temperature provides information about the chemical reaction but as described earlier, the computational model does not accurately predict the actual temperatures near the shock wave due to the insufficient resolution near the reaction zone, therefore those plots will not be presented [5].

For Figure 41 to Figure 49, pressure, particle velocity, and volume fraction will be plotted against position. These figures are a snap-shoot of the shock wave at a time after the wave has reached steady-state. To compare the different cases to each other a position of 1.6 mm was chosen for all the plot. Although the time might be different for each case, the chosen position is far enough that steady-state has been reached for all the cases. Once steady-state is reached all the properties will not change for the range being considered here.

Figure 41 to Figure 43 plot pressure versus position for the smallest and largest Al particle diameter, 9 and 34 μm, at each Al mass fraction. The most important pressure for these plots is the pressure of gas reaction product. The pressure of the metal particles is not important because it is not driving the shock wave. The pressure of the explosive is the same as the gas pressure until the explosive volume fraction goes to zero. The data for the pressure of the explosive is irrelevant after the volume fraction goes to zero because all the explosive material has been consumed by the reaction.

Figure 41a shows the peak gas pressure of the shock wave at 39.20 GPa for **PBX9501_10_9_up1.5**. Figure 41b shows the peak gas pressure of the shock wave at 43.64 GPa for **PBX9501_10_34_up1.5**. It is observed that at 10% Al mass fraction the shock wave pressure increases as the Al particle diameter increases.

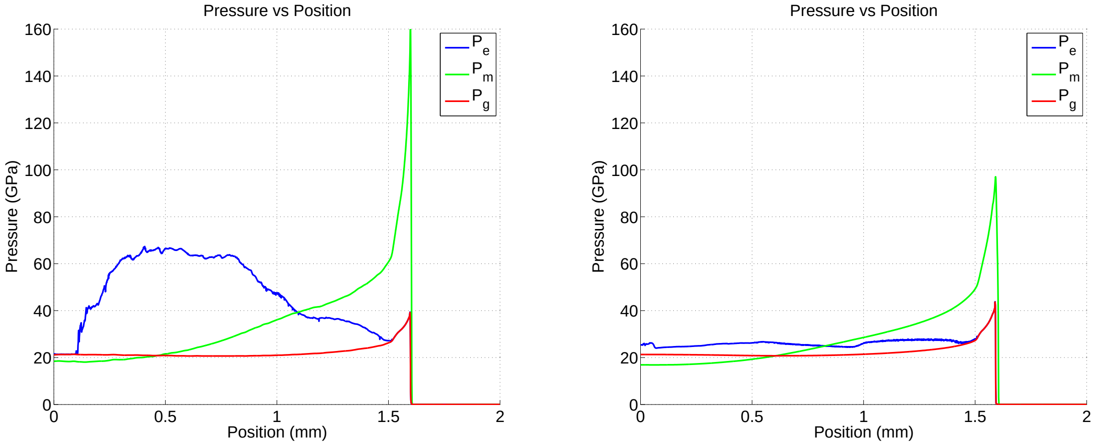

(a) PBX9501_10_9_up1.5_2000cells

(b) PBX9501_10_34_up1.5_2000cells

Figure 41. PBX9501 10% *Al* Mass Fraction Pressure Plot

Figure 42a and Figure 42b plot pressure versus position for **PBX9501_15_9_up1.5** and **PBX9501_15_34_up1.5**. Figure 42a shows the peak gas pressure of the shock wave at 36.51 GPa for **PBX9501_15_9_up1.5**. Figure 42b shows the peak gas pressure of the shock wave at 42.31 GPa for **PBX9501_15_34_up1.5**. It is observed that at 15% Al mass fraction the shock wave pressure increases as the Al particle diameter increases.

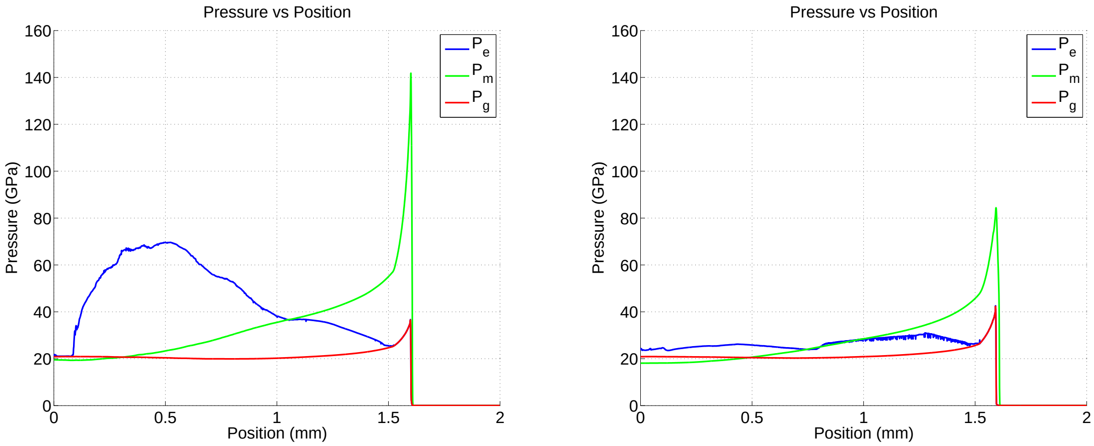

(a) PBX9501_15_9_up1.5_2000cells (b) PBX9501_15_34_up1.5_2000cells

Figure 42. PBX9501 15% *Al* Mass Fraction Pressure Plot

Figure 43a and Figure 43b plot pressure versus position for **PBX9501_20_9_up1.5** and **PBX9501_20_34_up1.5**. Figure 43a shows the location of shock wave to be at around 1.15 mm. The reason for the shock wave stopping at this location is due to the simulation quiting at t = 0.257 μs. Even though the simulation stopped early, the detonation reached steady-state prior to the quiting time and the results are still valid. Figure 43a shows the peak gas pressure of the shock wave at 31.23 GPa for **PBX9501_20_9_up1.5**. Figure 43b shows the peak gas pressure of the shock wave at 37.61 GPa for **PBX9501_20_34_up1.5**. It is observed that at 20% Al mass fraction the shock wave pressure increases as the Al particle diameter increases.

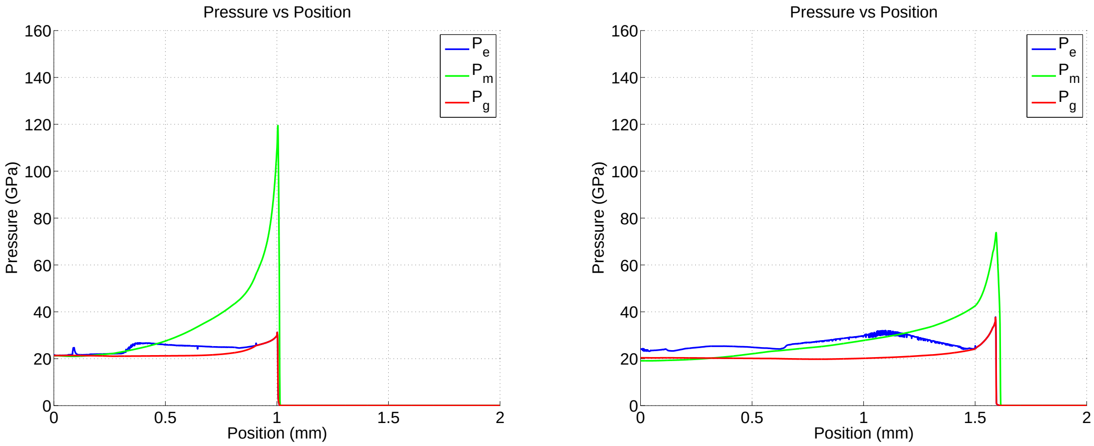

(a) PBX9501_20_9_up1.5_2000cells

(b) PBX9501_20_34_up1.5_2000cells

Figure 43. PBX9501 20% *Al* Mass Fraction Pressure Plot

Figure 44 to Figure 46 plot particle velocity versus position for the smallest and largest Al particle diameter, 9 and 34 μm, at each Al mass fraction. The most important particle velocity for these plots is the particle velocity of gas reaction product. The data for the particle velocity of the explosive is irrelevant after the volume fraction goes to zero because all the explosive material has been consumed by the reaction. Figure 44a shows the peak gas particle velocity of the shock wave at 3.609 km/s for **PBX9501_10_9_up1.5**. Figure 44b shows the peak gas particle velocity of the shock wave at 3.727 km/s for **PBX9501_10_34_up1.5**. It is observed that at 10% Al mass fraction the shock wave particle velocity increases slightly as the Al particle diameter increases.

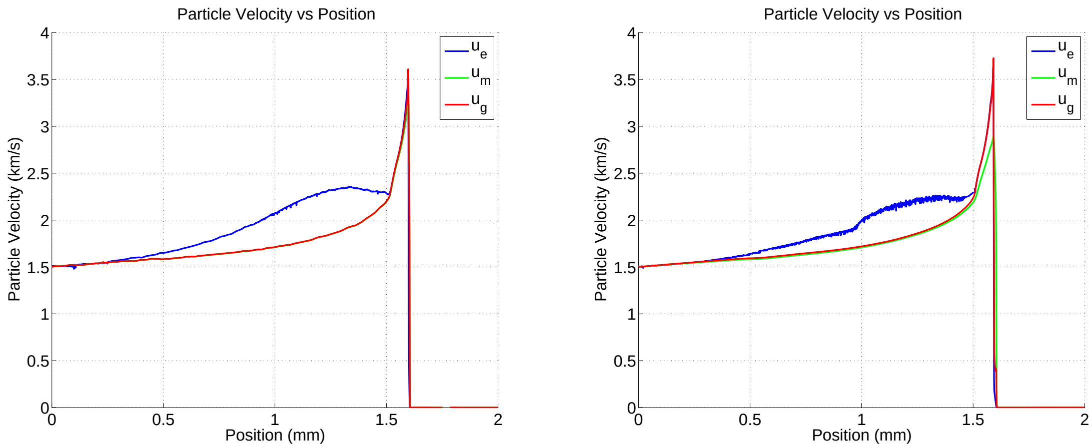

(a) PBX9501_10_9_up1.5_2000cells

(b) PBX9501_10_34_up1.5_2000cells

Figure 44. PBX9501 10% *Al* Mass Fraction Velocity Plot

Figure 45a and Figure 45b plot particle velocity versus position for **PBX9501_15_9_up1.5** and **PBX9501_15_34_up1.5**. Figure 45a shows the peak gas particle velocity of the shock wave at 3.580 km/s for **PBX9501_15_9_up1.5**. Figure 45b shows the peak gas particle velocity of the shock wave at 3.774 km/s for **PBX9501_15_34_up1.5**. It is observed that at 15% *Al* mass fraction the shock wave particle velocity increases slightly as the *Al* particle diameter increases.

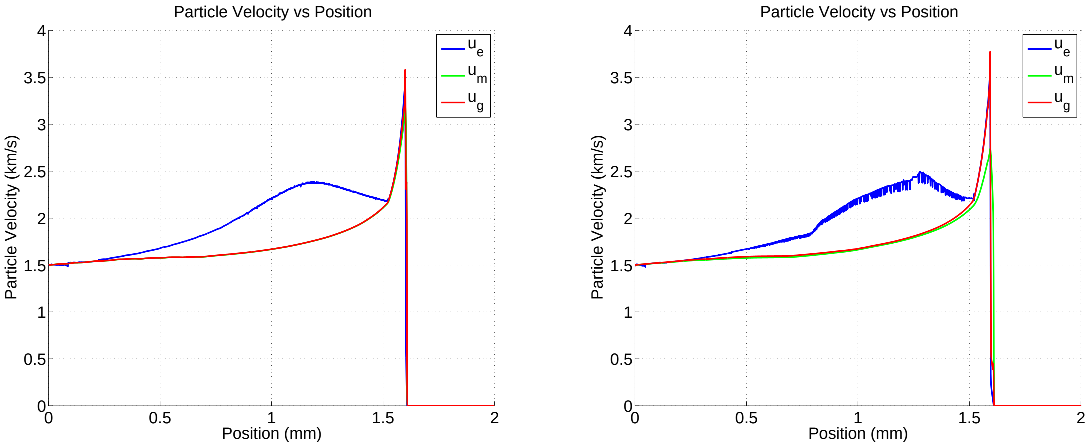

(a) PBX9501_15_9_up1.5_2000cells (b) PBX9501_15_34_up1.5_2000cells

Figure 45. PBX9501 15% *Al* Mass Fraction Velocity Plot

Figure 46a and Figure 46b plot particle velocity versus position for **PBX9501_20_9_up1.5** and **PBX9501_20_34_up1.5**. Figure 46a shows the peak gas particle velocity of the shock wave at 3.294 km/s for **PBX9501_20_9_up1.5**. Figure 46b shows the peak gas particle velocity of the shock wave at 3.591 km/s for **PBX9501_20_34_up1.5**. It is observed that at 20% *Al* mass fraction the shock wave particle velocity increases slightly as the *Al* particle diameter increases.

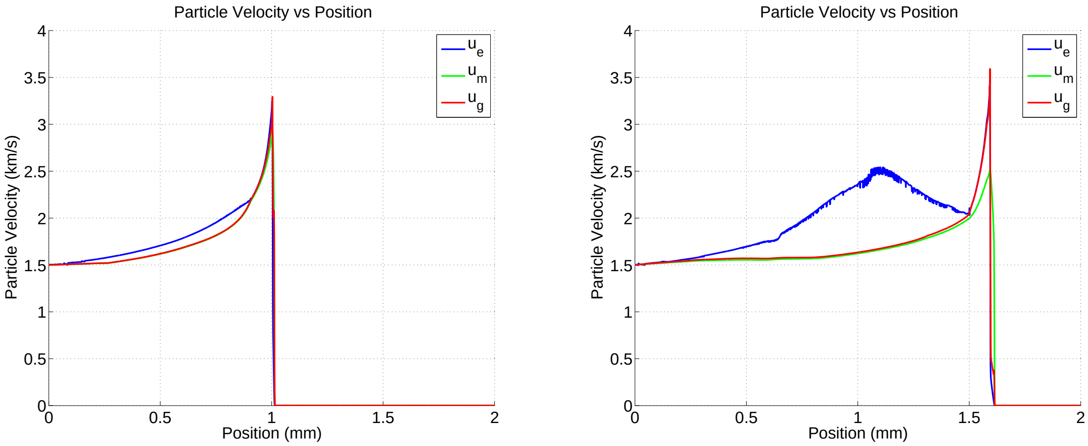

(a) PBX9501_20_9_up1.5_2000cells (b) PBX9501_20_34_up1.5_2000cells

Figure 46. PBX9501 20% Al Mass Fraction Velocity Plot

Figure 47 to Figure 49 plot volume fraction versus position for the smallest and largest Al particle diameter, 9 and 34 μm, at each Al mass fraction. All the volume fraction plots presented in the figures below look the same. The reason all the plots look the same is because all the simulations should be at steady-state at this position. The volume fraction for the explosive material, represented by the blue line, should go to zero shortly after the shock wave has passed. The volume fraction for the gas, represented by the red line, should go to total volume fraction set by the user after the shock wave has passed. The volume fraction for the metal, represented by the green line, should remain constant because the metal in non reactive in the simulation. The explosive volume fraction should exponentially decay to zero very sharply and the gas volume fraction should exponentially increase very sharply to the total solids volume fraction. All these conditions are met by all the simulation at the plotted position and time, verifying that all simulations are at steady-state.

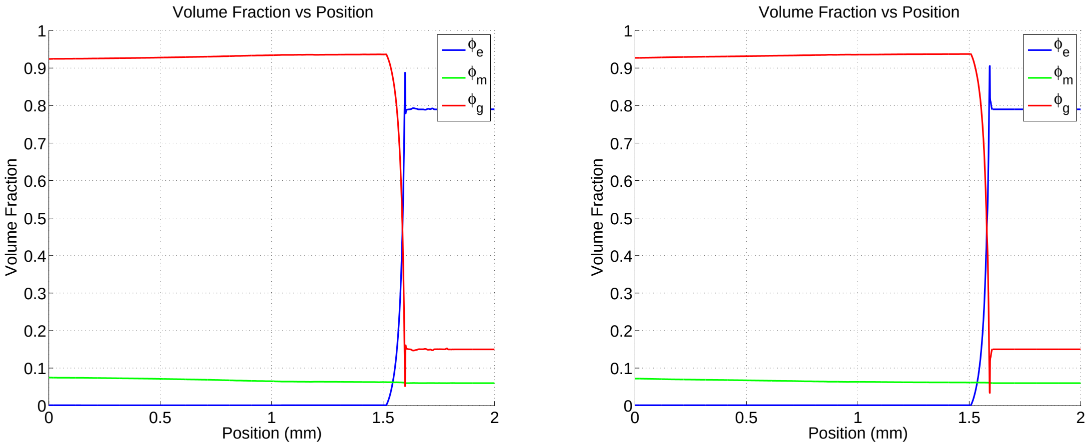

(a) PBX9501_10_9_up1.5_2000cells (b) PBX9501_10_34_up1.5_2000cells

Figure 47. PBX9501 10% *Al* Mass Fraction Volume Fraction Plot

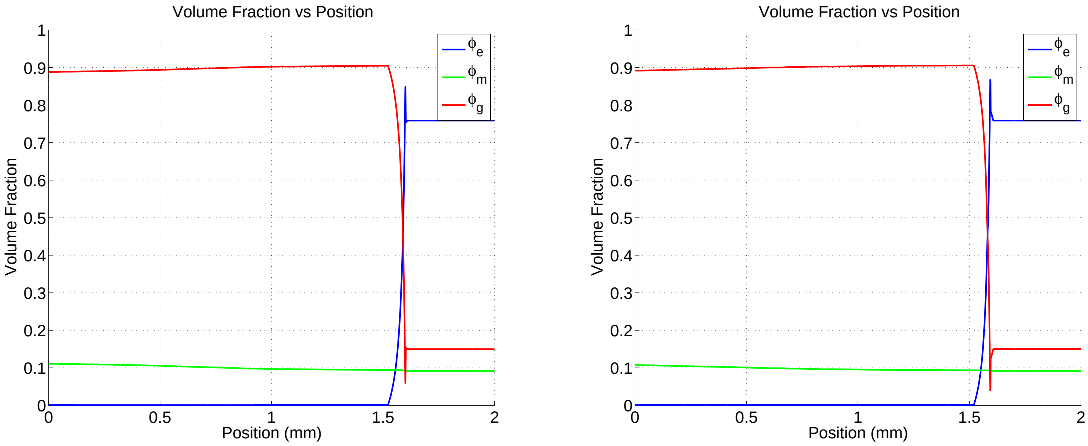

(a) PBX9501_15_9_up1.5_2000cells (b) PBX9501_15_34_up1.5_2000cells

Figure 48. PBX9501 15% *Al* Mass Fraction Volume Fraction Plot

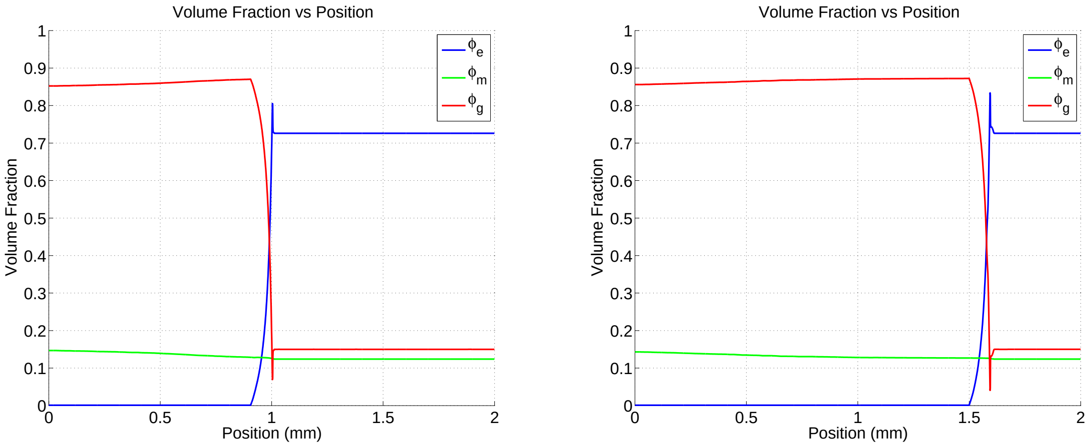

(a) PBX9501_20_9_up1.5_2000cells (b) PBX9501_20_34_up1.5_2000cells

Figure 49. PBX9501 20% *Al* Mass Fraction Volume Fraction Plot

Figure 50a shows the peak gas density of the shock wave at 2319 kg/m^3 for **PBX9501_10_9_up1.5**. Figure 50b shows the peak gas density of the shock wave at 2419 kg/m^3 for **PBX9501_10_34_up1.5**. It is observed that at 10% *Al* mass fraction the shock wave density increases as the *Al* particle diameter increases.

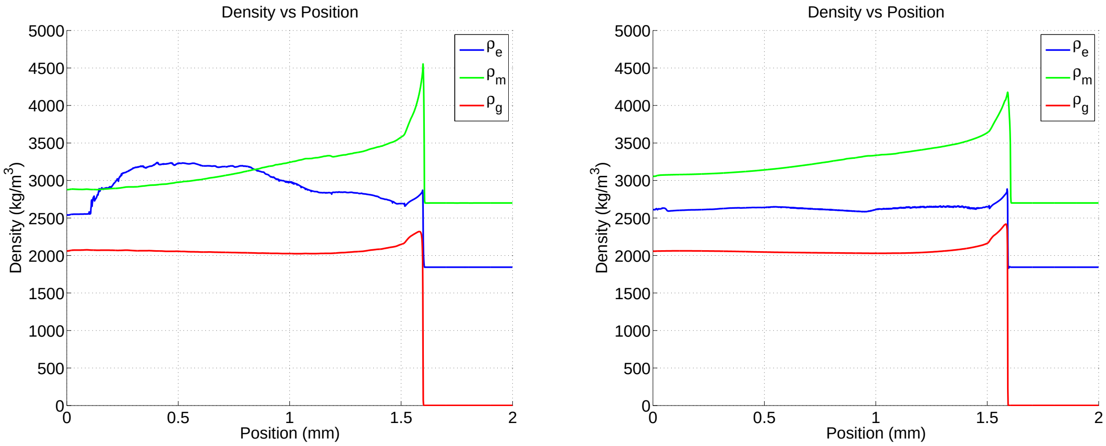

(a) PBX9501_10_9_up1.5_2000cells (b) PBX9501_10_34_up1.5_2000cells

Figure 50. PBX9501 10% *Al* Mass Fraction Density Plot

Figure 51a and Figure 51b plot density versus position for **PBX9501_15_9_up1.5** and **PBX9501_15_34_up1.5**. Figure 51a shows the peak gas density of the shock wave at 2243 kg/m^3 for **PBX9501_15_9_up1.5**. Figure 51b shows the peak gas density of the shock wave at 2361 kg/m^3 for **PBX9501_15_34_up1.5**. It is observed that at 15% Al mass fraction the shock wave density increases as the Al particle diameter increases.

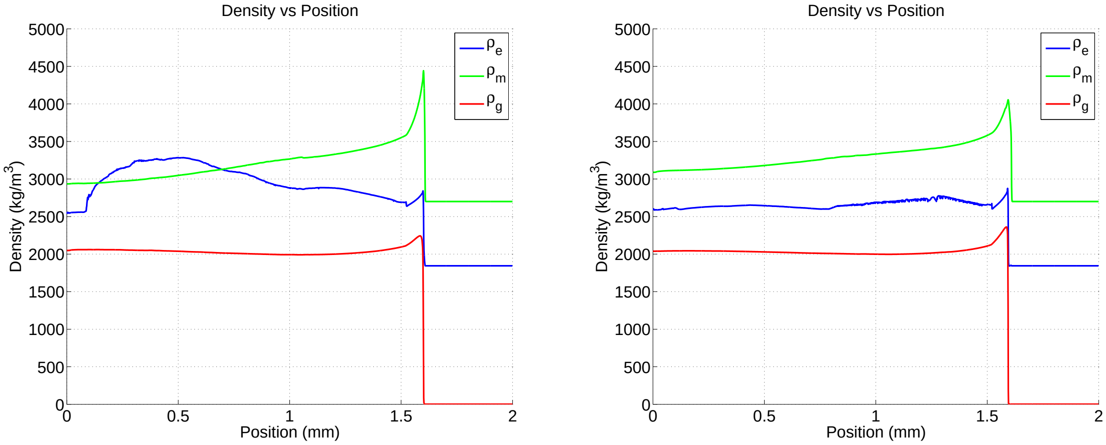

(a) PBX9501_15_9_up1.5_2000cells

(b) PBX9501_15_34_up1.5_2000cells

Figure 51. PBX9501 15% Al Mass Fraction Density Plot

Figure 52a and Figure 52b plot density versus position for **PBX9501_20_9_up1.5** and **PBX9501_20_34_up1.5**. Figure 52a shows the peak gas density of the shock wave at 2168 kg/m^3 for **PBX9501_20_9_up1.5**. Figure 52b shows the peak gas density of the shock wave at 2270 kg/m^3 for **PBX9501_20_34_up1.5**. It is observed that at 20% Al mass fraction the shock wave density increases as the Al particle diameter increases.

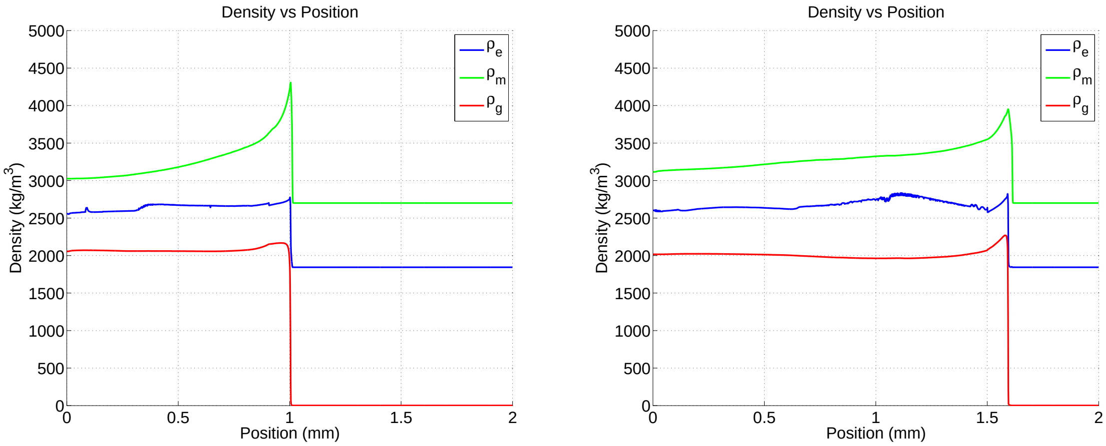

(a) PBX9501_20_9_up1.5_2000cells (b) PBX9501_20_34_up1.5_2000cells

Figure 52. PBX9501 20% *Al* Mass Fraction Density Plot

Table 12 provides the data collected for the shock wave gas pressure, gas products particle velocity, and gas density. Run # 1 through 6 are the simulations for 10% *Al* mass fraction from 9 μm to 34 μm *Al* particle diameter. Run # 7 through 12 are the simulations for 15% *Al* mass fraction from 9 μm to 34 μm *Al* particle diameter. Run # 13 through 18 are the simulations for 20% *Al* mass fraction from 9 μm to 34 μm *Al* particle diameter. The gas pressure is in gigapascals, the gas particle velocity is in kilometers per second, and the density is in kilograms per meter cubed.

Table 12. PBX9501/Al Gas Properties at $u_p = 1.5$ km/s Nx = 2000cells

Run #	**Name**	**Pressure** (GPa)	**Part. Vel.** (km/s)	**Density** (kg/m^3)
1	PBX9501_10_9	39.200	3.609	2319
2	PBX9501_10_13	40.640	3.779	2336
3	PBX9501_10_19	41.300	3.718	2363
4	PBX9501_10_23	41.960	3.719	2381
5	PBX9501_10_29	42.480	3.798	2403
6	PBX9501_10_34	43.640	3.727	2419
7	PBX9501_15_9	36.510	3.580	2243
8	PBX9501_15_13	37.700	3.601	2259
9	PBX9501_15_19	38.940	3.831	2297
10	PBX9501_15_23	40.530	3.737	2319
11	PBX9501_15_29	41.330	3.700	2346
12	PBX9501_15_34	42.310	3.774	2361
13	PBX9501_20_9	31.230	3.294	2168
14	PBX9501_20_13	33.600	3.411	2167
15	PBX9501_20_19	34.680	3.573	2197
16	PBX9501_20_23	35.850	3.464	2218
17	PBX9501_20_29	36.600	3.652	2245
18	PBX9501_20_34	37.610	3.591	2270

The results from the table above are presented in a chart to better observe the trends in the data. Figure 53 plots the pressure versus Run # for the three aluminum mass fractions. The first six data point are for the six Al particle diameters at 10% Al mass fraction and are represented by the blue diamonds. The next six data point are for the six *Al* particle diameters at 15% *Al* mass fraction and are represented by the red squares. The last six data point are for the six *Al* particle diameters at 20% *Al* mass fraction and are represented by the green triangles. It can be seen from Figure 53 the gas pressure steadily increases as the *Al* particle diameter increases at 10% *Al* mass fraction. For 15% *Al* mass fraction the first pressure is less than than all the 10% *Al* mass fraction cases. The same trend is observed for 15% *Al* mass fraction, where the gas pressure steadily increases as the *Al* particle diameter increases. Again for 20% *Al* mass fraction the first pressure is lower than all the 10% and 15% *Al* mass fraction cases. The same trend is observed for 20% *Al* mass fraction cases where the gas pressure steadily increases as the *Al* particle diameter increases.

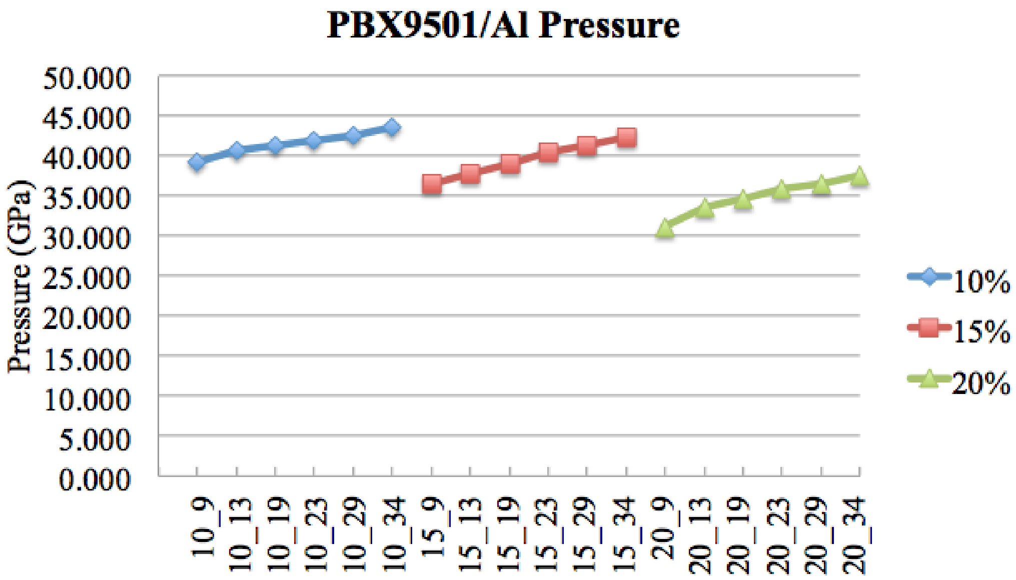

Figure 53. PBX9501 All Cases Gas Pressure

Figure 54 plots the gas particle velocity versus Run # for the three aluminum mass fractions. The same color and symbols are utilized for the different simulation runs as in Figure 53. All the 18 simulations have the same gas particle velocity pattern. As the *Al* particle diameter increases in each mass fraction case, the particle velocity goes up and down. It was concluded that on average the particle velocity remains constant with varying *Al* particle diameter. There is a very small drop on particle velocity from 10% to 15% to 20%.

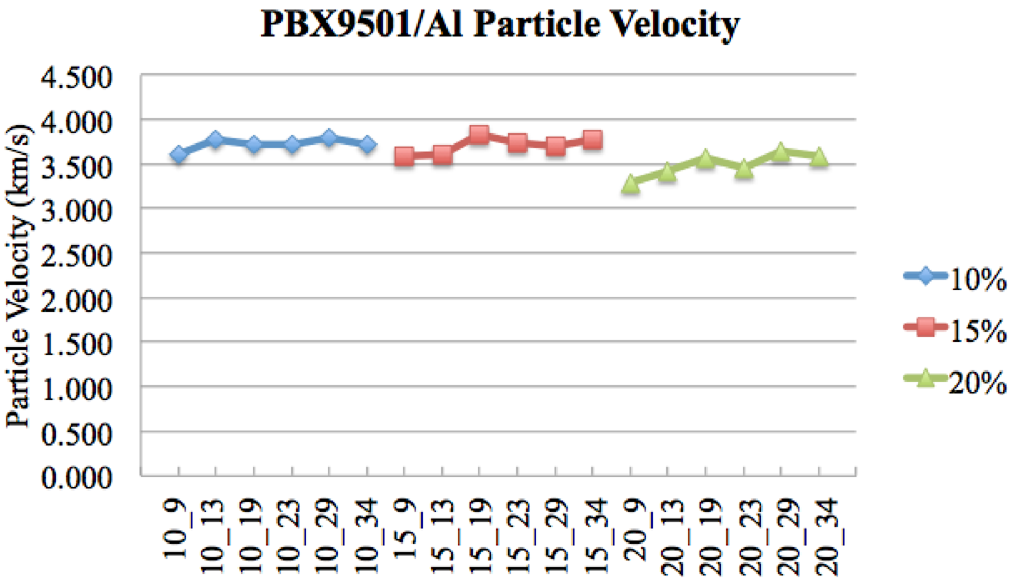

Figure 54. PBX9501 All Cases Gas Particle Velocity

Figure 55 plots the gas density versus Run # for the three aluminum mass fractions. It can be seen from Figure 55 the gas density steadily increases as the *Al* particle diameter increases at 10% *Al* mass fraction. For 15% *Al* mass fraction the first density is less than than all the 10% *Al* mass fraction cases. The same trend is observed for 15% *Al* mass fraction, where the gas density steadily increases as the *Al* particle diameter increases. Again for 20% *Al* mass fraction the first density is lower than all the 10% and 15% *Al* mass fraction cases. The same trend is observed for 20% *Al* mass fraction cases where the gas density steadily increases as the *Al* particle diameter increases.

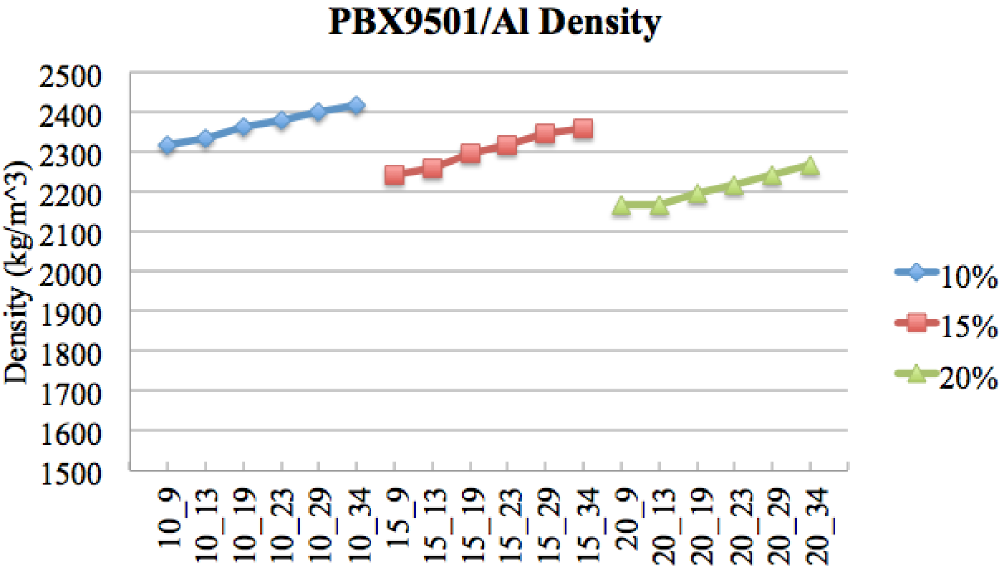

Figure 55. PBX9501 All Cases Gas Density

4.5 Conclusion

This chapter presented the results from the three main studies that were performed. The purpose of these studies was to evaluate the stability and limitations of the MPEXS code. The first study was a short study with neat PBX9501 to compare run-to-detonation properties against a single phase explosive code developed by AFRL. The second study was a convergence test of detonation properties by varying the number of computational cells for metalized PBX9501. The third study was to study the effects of aluminum on PBX9501 by performing several simulations at a range of aluminum mass fractions and aluminum particle diameters.

V. Conclusions

To find solutions to the bigger issues such as the risks of injuring or killing innocent civilians in current and future asymmetrical warfare, smaller more elementary problems need to be understood. The main focus of this research was to study and understand the effects of aluminum in high explosive such as PBX9501 using a computational simulation code. The MPEXS hydrocode was utilized in this research to perform simulations of a wide range of metalized explosive cases where the size of the Al particle and the Al mass fraction was varied. The results were separated into two sections, the performance evaluation of the MPEXS code and the study of the effects of aluminum on PBX9501.

5.1 Performance Evaluation of the MPEXS Code

The MPEXS code was evaluated by performing several studies to determine the stability and limitations of the code. The first study was a short study with neat PBX9501 to compare Run2Det properties against the SPEXS code for different piston speeds. It was important to establish a baseline by studying the behavior of the code with neat PBX9501 with no aluminum. The second study was a convergence test of detonation properties by varying the number of computational cells for metalized PBX9501. The goal of this study was to test the stability of the code by looking for a convergence in the data as the number of computational cells increased.

The first study showed that the average rate of change for Run2Det distance and time between each set of mass fraction points was larger for the SPEXS code. The difference in results in both codes does not imply the MPEXS code is bad, it only means that different equations of state and burn rates were utilized. The takeaway is the MPEXS code followed the same trend as the SPEXS code, where Run2Det distance and time decreases exponentially as the piston impact speed is increased.

The second study showed that the stability of the code was proved by the converging results as the number of computational cells increased. The number of computational cells is related to the resolution or the grid size of the simulation. It was concluded that as the resolution increased, the results became closer and closer to the same number, showing a converging pattern. The limits of the MPEXS were also tested with the small computational cell sizes of Nx = 200 and Nx = 400. When these small values were utilized the code failed to run. The code ran for Nx = 800 and Nx = 1000 but these small values provide unstable results that varied. It was not until Nx values larger than 1300 when the Run2Det result began to converge. It can be concluded that the MPEXS code, although its limitations, is stable and provides expected results.

Below is a short bulleted list to summarize this section on performance evaluation of the MPEXS code.

- Study 1: Neat Explosive
    - Different from SPEXS due to different EOS
    - MPEXS code follows same trend as SPEXS
- Study 2: Convergence Test
    - Run2Det distance and time results converged as Nx increased
    - Detonation velocity results converged as Nx increased
    - MPEXS code is stable and provides expected results

5.2 The Effects of Aluminum on PBX9501 Explosive

The main focus of this research was to use the MPEXS hydrocode to run a wide range of simulations of metalized PBX9501 and determine what effects aluminum particulates have on PBX9501. Three aluminum mass fractions were utilized; 10, 15, and 20 percent. At each of those aluminum mass fractions, six aluminum diameters were tested; 9, 13, 19, 23, 29, and 34 micron diameter.

The 18 simulation runs were performed for two computational cell, 800 and 2000. The purpose of running simulations with both sizes of computational cells, 800 and 2000 cells, was to study the effects of grid size on metalized explosive simulations. It can be concluded that the simulations using 2000 computational cells provide more consistent results for both varying parameters, Al mass fraction and Al particle diameter. In Section 4.3, it was found that at lower resolutions the detonation property results are unstable. The same stability issues at the low resolution using 800 cells was seen especially for detonation velocity at 15 and 20 percent Al mass fraction.

As mentioned before, run-to-detonation properties are very important in the evaluation of of explosive materials. Run2Det distance and Run2Det time were plotted for all the 18 simulation runs. Increasing the Al mass fraction from 10% to 15% decreased the Run2Det distance by an average of 0.012 mm, where as increasing the Al particle diameter decreased the Run2Det distance by an average of 0.001 mm. The same observation was made for Run2Det time. It was concluded that varying the aluminum mass fraction had a larger effect on Run2Det properties than varying the aluminum particle diameter for both Run2Det distance and time. In general, increasing the Al mass fraction will decrease the the time and distance for the detonation to reach steady-state. If shorter Run2Det distance and time is a desired, then increase the Al mass fraction

The other detonation properties such as detonation velocity, pressure, and density had the following results as Al mass fraction and particle diameter were varied. Detonation velocity steadily decreased as the Al particle diameter was increased. Also, as the Al mass fraction increased the detonation velocity decreased. The results showed that the gas pressure steadily increased as the Al particle diameter increased at 10% Al mass fraction. The same pressure increase with particle diameter was seen for 15% and 20% Al mass fraction. For each increase in mass fraction the first pressure was less than than all the previous Al mass fraction cases, clearly shown in Figure 53. The gas density showed the same trends as gas pressure as discussed in this paragraph. The gas density steadily increased as the Al particle diameter increased but decreased when Al mass fraction was increased. It can be concluded that on average the particle velocity remained constant with varying Al particle diameter. There is a very small decrease in particle velocity from 10% to 15% to 20%, but not significant enough to vary the Al mass fraction in the explosive.

The addition of metal particulates in explosive mixtures increases density to the shock wave, causing a higher pressure in the shock. The high pressure in the shocks are devastating and will incapacitate adversaries in physical proximity of the detonation of the munition. The addition of Al particulates in explosive mixtures and low fragmentation weapons with concentrated pressures that dissipate quickly will provide the capabilities needed to develop weapons needed to fight current and future asymmetric warfare. In conclusion, this research significantly contributes to both current explosive simulation analysis and development of future explosive formulations for better munitions that will save many lives.

Below is a short bulleted list to summarize this section on the effects of aluminum on PBX9501 explosive.

- Aluminum Particle Size - Increases
    - Pressure - Increases
    - Density - Increases
    - Particle Velocity - Remained constant

  - Run2Det Distance and Time - Small decrease
  - Detonation Velocity - Decreases
- Aluminum Mass Fraction - Increases
  - Pressure - Decreases
  - Density - Decreases
  - Particle Velocity - Remained constant
  - Run2Det Distance and Time - Decreases
  - Detonation Velocity - Decreases

5.3 Recommendations

Based on the results for metalized explosive PBX9501, the best explosive mixture is PBX9501 at 10% aluminum mass fraction and 34 μm aluminum particle diameter. **PBX9501_10_34** has the highest gas pressure and density for both particle diameter and mass fraction. The gas pressure for this case is 43.64 GPa and the gas density is 2419 kg/m^3. The detonation velocity was the lowest for 10% mass fraction but it was higher than the other mass fractions. The detonation velocity for this case is 7.997 km/s. The Run2Det time is 0.258 μs and the Run2Det distance is 1.017 μm. All these properties are for a piston speed of 1.5 km/s. If a shorter Run2Det time and distance is desired, the aluminum mass fraction can be increased to 15% with an aluminum particle diameter of 34 μm but there will be some losses in other parameters. For 15% Al mass fraction, the Run2Det time is 0.232 μs and the Run2Det distance is 0.926 μm. The pressure and density will not affected as much by the increase in aluminum. The gas pressure for this case is 42.31 GPa and the gas density is 2361 kg/m^3. The detonation velocity for this case is 7.848 km/s, a loss of 149 m/s. The aluminum mass fraction of 20% can be utilized but the benefits gained are not worth it.

Below is a short bulleted list to summarize this paragraph on explosive recommendations.

- Best mixture - PBX9501 10% 34 μm
    - Highest Pressure: P = 43.64 GPa
    - Highest Density: ρ = 2419 kg/m^3
    - Lowest Detonation Velocity for 10% but higher than 15% and 20%: D = 7.997 km/s
    - Run2Det Time: t = 0.258 μs
    - Run2Det Distance: x = 1.017 mm
- If shorter Run2Det time and distance is desired
    - Increase Al mass fraction to 15%
    - Results in losses in Pressure, Density, and Detonation Velocity
- No - Al mass fraction of 20%
    - Results in losses in Pressure, Density - deviates from munitions purpose

The MPEXS hydrocode is still in a testing phase, therefore there are many opportunities for improvement and ease of use. Throughout this research there were several updates to the code that came from testing. The most current version that was utilized to generate the results presented in this document still has limitations and issues to be worked on. In Section 4.3 it was documented that the code would stop short of the final run time for all the cases. The short running times might be due to larger numerical errors in lower resolution simulations versus errors in higher resolution simulations. The short running time issue should be corrected in future versions of the code. Another reported issue discussed in Section 3.6.2 was that the code fails and quits the simulation run for piston impact speeds of 2.0 km/s at high Al mass fraction cases. This high metal mass fraction, high impact speed problem has been reported to AFRL, so it can be resolved in future versions of the code. It would be useful if the MPEXS code provided feedback to the user when bad inputs are entered or when input parameters are outside the limits of the code. Error messages before the simulation begins should be added to future versions of the code. The MPEXS code is stable and provides good results for metalized PBX9501 explosive. The next step is to make the code more user friendly, add more EOS to handle more explosives, and improve feedback for inputs that will make the code crash.

Below is a short bulleted list to summarize this paragraph on future MPEXS code versions.

- Fix all reported issues
  - Simulations stopping short of final time
  - Issues with high Al mass fraction with high impact speeds
- Make code more user friendly
  - Better input interface
  - Error/Warning messages for inputs outside limits
- Add capability for more explosives and metals

Bibliography

1. Ao, T. "Line-imaging ORVIS measurements of interferometric windows under quasi-isentropic compression". *Proceedings of the SEM Annual Conference*, 2. Society for Experimental Mechanics Inc, June 2009.

2. Baer, M.R. "Modeling heterogeneous energetic materials at the mesoscale". *Thermochimica Acta*, 384(12):351 – 367, 2002. ISSN 0040-6031. URL `http://www.sciencedirect.com/science/article/pii/S0040603101007948`.

3. Baer, M.R. and J.W. Nunziato. "A Two-Phase Mixture Theory for the Deflagration-to-Detonation Transition (DDT) in Reactive Granular Materials". *International Journal of Multiphase Flow*, 12(6):861 – 889, 1986. ISSN 0301-9322. URL `http://www.sciencedirect.com/science/article/pii/0301932286900339`.

4. Cooper, Paul W. *Explosives Engineering*. Wiley-VCH, New Mexico, 1996. ISBN 9780471186366.

5. Crochet, Michael Wayne. *Modeling, Numberical Analysis, and Predictions for the Detonation of Multi-Component Energetic Solids*. Dissertation, Louisiana State University, Indiana, December 2013.

6. Crochet, Michael Wayne. "Multiphase Hydrocode Software Quick Start Guide", September 2014. Ver2.

7. Crochet, M.W. and K.A. Gonthier. "Numerical Investigation of a Modified Family of Centered Schemes Applied to Multiphase Equations with Nonconservative Sources". *Journal of Computational Physics*, 255(0):266 – 292, December 2013. ISSN 0021-9991. URL `http://www.sciencedirect.com/science/article/pii/S002199911300541X`.

8. Fedorov, A.V. and Yu.V. Kharlamova. "Ignition of an Aluminum Particle". *Combustion, Explosion and Shock Waves*, 39(5):544–547, 2003. ISSN 0010-5082. URL `http://dx.doi.org/10.1023/A%3A1026109801863`.

9. Fickett, W. and W.C. Davis. *Detonation: Theory and Experiment*. Dover Books on Physics Series. Dover Publications, 2000. ISBN 9780486414560.

10. GlobalSecurity.org. "Operation Desert Fox". Online Source, May 2011. URL `http://www.globalsecurity.org/military/ops/desert_fox.htm`.

11. Gogulya, M. F., A. Yu. Dolgoborodov, M. A. Brazhnikov, and G. Baudin. "Detonation Waves in HMX/Al Mixtures (Pressure and Temperature Measurements)". *Proceedings of the Eleventh International Detonation Symposium*, 979–988. Sept 1998.

12. Inc, Toyal America. "Toyal Spherical Aluminum Powders for Aerospace". Online Website, May 2015. URL `http://www.toyala.com/cgi-bin/r.cgi/powders_spherical_aero.html?OWNER=7t8fDkJt7`.

13. Kapila, A. K., R. Menikoff, J. B. Bdzil, S. F. Son, and D. S. Stewart. "Two-phase Modeling of Deflagration-to-Detonation Transition in Granular Materials: Reduced Equations". *Physics of Fluids (1994-present)*, 13(10):3002–3024, 2001. URL `http://scitation.aip.org/content/aip/journal/pof2/13/10/10.1063/1.1398042`.

14. VanderSteen, A.C., H.J. Verbeek, and J.J. Meulenbrugge. "Influence of RDX Crystal Shape on the Shock Sensitivity of PBXs". *Proceedings of the Ninth International Detonation Symposium*, 83–88. Sept 1989.

15. Yang, L., Y. Horie, A.J. Lindfors, and P.J. Miller. *An Analysis of Shock-Induced Reactions in a Fe2O3 Al Teflon Powder Mixture*. Cr n000 14094-1-0240-02, North Carolina State University and Naval Air Warefare Center, October 1996.

REPORT DOCUMENTATION PAGE

Form Approved
OMB No. 0704–0188

1. REPORT DATE *(DD–MM–YYYY)*
05–29–2015

2. REPORT TYPE
Master's Thesis

3. DATES COVERED *(From — To)*
Oct 2013 — May 2015

4. TITLE AND SUBTITLE

SIMULATION OF METAL PARTICULATES
IN HIGH ENERGETIC MATERIALS

5a. CONTRACT NUMBER

5b. GRANT NUMBER

5c. PROGRAM ELEMENT NUMBER

6. AUTHOR(S)

Eduardo Nieto, U.S. Air Force

5d. PROJECT NUMBER

5e. TASK NUMBER

5f. WORK UNIT NUMBER

7. PERFORMING ORGANIZATION NAME(S) AND ADDRESS(ES)

Air Force Institute of Technology
Graduate School of Engineering and Management (AFIT/EN)
2950 Hobson Way
WPAFB OH 45433-7765

8. PERFORMING ORGANIZATION REPORT NUMBER

AFIT-ENY-MS-15-J-043

9. SPONSORING / MONITORING AGENCY NAME(S) AND ADDRESS(ES)

Air Force Research Laboratory Munitions Directorate
2306 Perimeter Rd
Eglin AFB, FL 32542
Pemberton, Steven J Civ USAF AFRL/RWME
Email: steven.pemberton.1@us.af.mil

10. SPONSOR/MONITOR'S ACRONYM(S)

AFRL

11. SPONSOR/MONITOR'S REPORT NUMBER(S)

12. DISTRIBUTION / AVAILABILITY STATEMENT

DISTRIBUTION STATEMENT A:
APPROVED FOR PUBLIC RELEASE; DISTRIBUTION UNLIMITED.

13. SUPPLEMENTARY NOTES

14. ABSTRACT

This research focused on analyzing the effects of aluminum in high explosives such as PBX9501 using the MPEXS computational simulation code for a wide range of metalized explosive cases. The varying parameters are aluminum particle diameter and mass fraction of aluminum. The addition of metal particulates in explosive mixtures increases the density of the shock wave, causing a higher pressure in the shock. It was concluded that pressure and density steadily increases as the Al particle diameter increases, and pressure and density decreases when Al mass fraction increases. The concentrated pressures will dissipate quickly due to the high density, providing a short proximity detonation. This research significantly contributes to both current explosive simulation analysis and development of future explosive formulations for better munitions that will save many innocent lives.

15. SUBJECT TERMS

multi-phase, explosive, computational method, hydrocode, simulation, PBX9501, detonation

16. SECURITY CLASSIFICATION OF:			17. LIMITATION OF ABSTRACT	18. NUMBER OF PAGES	19a. NAME OF RESPONSIBLE PERSON
a. REPORT	b. ABSTRACT	c. THIS PAGE			Dr. Robert B. Greendyke, AFIT/ENY
					19b. TELEPHONE NUMBER *(include area code)*
U	U	U	UU	136	(937) 255-3636, x4567; robert.greendyke@afit.edu